

**Geological and Geochemical Characteristics of the Mugomo and Chifumbazi  
Gold Deposits, Tete Province, Mozambique - Constraints on the Ore Genesis**

**モザンビーク、Tete 地域、Mugomo および Chifumbazi 金鉱床の地質と地球化学  
的特徴 - 鉱床成因の制約条件**

By

Euclesia Paulina Francisco Cossa

A Doctoral Thesis

Submitted to the Department of Earth Resource Science

Akita University

In Fulfillment of the Requirements

For a Doctoral Degree

March 2023

## Abstract

The Mugomo and Chifumbazi gold deposits are located in the Chifunde District, Tete Province, northwestern Mozambique. The geology of the study area is composed of the Proterozoic Mualadzi Group comprising ultramafic metavolcanic rocks, quartzite, biotite-schist, Macanda Mafic Metavolcanics, conglomerate, and granitoid of the Furancungo Suite. The geological characteristics and metallogenesis of gold mineralization in the Tete Province are poorly understood. This study aims to describe gold mineralization and associated hydrothermal alteration in the Mugomo and Chifumbazi deposits on the bases of petrography, whole rock geochemistry, fluid inclusion, and sulfur isotopes.

The host rocks of the Mugomo deposit are metavolcanic rocks, biotite-schist, and quartzite, and they are cut by epidote and quartz veins and epidote-quartz-chlorite veins and veinlets. The host rocks of the Chifumbazi deposit are quartz-mica-schist (*i.e.*, meta-plutonic rock) overlain by gneiss, and the former is cut by quartz, quartz-carbonate (calcite, dolomite, and ankerite), and chlorite veins and veinlets. The veins and veinlets occur along the discordant fracture system within a Pan-African shear zone.

The metavolcanic rocks in the Mugomo deposit are composed mainly of plagioclase, quartz, and biotite, with secondary epidote, chlorite, and calcite, the biotite schist is composed mainly of biotite and quartz. The quartzite is composed of quartz and minor plagioclase. In the Chifumbazi deposit, the quartz-mica-schist is composed mainly of quartz, plagioclase, biotite, and muscovite, with secondary calcite, ankerite, sericite, and chlorite, while the gneiss is composed chiefly of quartz, biotite, and opaque minerals. Hydrothermal calcite, chlorite, and sericite occur either as small veins and veinlets or as alterations replacing primary minerals.

The metavolcanic rocks of the Mugomo deposit have a narrow range of  $\text{SiO}_2$  (69.5–81.7 wt.%) and can be classified as rhyolite or dacite in composition using the classification diagram of  $\text{Zr/TiO}_2$  vs.  $\text{Nb/Y}$ . The metavolcanic rock shows moderate concentrations of  $\text{FeO}_T$  (1.37–11.59 wt.%). The  $\text{Al}_2\text{O}_3$  contents vary from 9.23 to 16.14 wt%, while the concentration of CaO varies between 0.44 and 6.44 wt.%.

The quartz-mica-schist in the Chifumbazi deposit has a SiO<sub>2</sub> content (55.2- 72.4 wt.%), and it can be classified as rhyodacite or dacite which is almost equivalent to granodiorite in composition using the volcanic rock classification diagram of Zr/TiO<sub>2</sub> vs Nb/Y. The quartz-mica-schist has moderate FeO<sub>T</sub> contents (2.85-7.52 wt.%), Al<sub>2</sub>O<sub>3</sub> contents from 12.6 to 20.0 wt%, CaO contents from 0.15 to 3.73 wt.%, as well as negative anomalies of Nb, Sr, P, Eu, and Ti, and positive anomalies of Rb, Ba, K, and Pb in primitive normalized plots. On the other hand, the metavolcanic rocks of the Mugomo deposit are depleted in Rb, Nb, P, Eu, and Ti.

The ICP-MS whole rock data from the Mugomo deposit compositions indicate up to 2 ppm Au, 16 ppm Ag, 281 ppm Cu, 19 ppm Te and 87 ppm Pb which suggests that the main mineralization stage includes visible gold in pyrite disseminated in the metavolcanic rock. On the other hand, the quartz veins in Stage II of the Chifumbazi deposit include visible gold associated with pyrite and chalcopyrite. The whole rock compositions indicate up to 5 ppm Au, 30 ppm Ag, 8064 ppm Cu, 310 ppm Ni, 85 ppm Te, and 65 ppm Pb in the milky quartz veins.

Homogenization temperatures and salinity of fluid inclusions in quartz veins of the Mugomo deposit range from 200 to 430 °C and from 0.0 to 15.0 wt.% NaCl equiv., respectively, while those in Stage II of the Chifumbazi deposit range from 216 to 369 °C and from 0.7 to 15.3 wt.% NaCl eq, respectively.

The presence of shear zones is one of the important geological constraints for the formation of vein systems in the northern part of Tete province, as sulfides and gold are commonly found associated with quartz, quartz-carbonate, chlorite, and epidote veins.

Based on the geological setting, mineralogy, trace elements in quartz, fluid inclusions, and sulfur isotope signatures, the Mugomo and Chifumbazi deposits can be classified as orogenic type. Especially, the Chifumbazi deposit has distinct characteristics of orogenic gold mineralization, i.e., (i) orientation of veins structurally controlled by faults and shear zones, (ii) proximal sericite-chlorite-carbonate alterations, and (iii) presence of CO<sub>2</sub> in vapor inclusions of quartz veins.

**Keywords:** Chifumbazi and Mugomo deposits, hydrothermal alteration, gold mineralization, fluid inclusion, S-isotope, orogenic deposit.

## **ACKNOWLEDGMENTS**

First of all, I want to thank God for the blessings he has given me in my life and for the divine grace that I found before his eyes. Everything I managed to achieve was not by my strength, but it was all by divine grace.

I am very much indebted to my supervisors and co-supervisors, Prof. Andrea Agangi, Assoc. Prof. Ryohei Takahashi, Prof. Akira Imai, and Dr. Vicente Manjate for believing in me and having accepted the research project. I would also like to thank them for their guidance, straightforwardness, constructive criticisms, and discussions during the research period.

I'm greatly indebted to the Japan International Cooperation Agency (JICA) for sponsoring my studies at Akita University and to Tete high Polytechnic Institute for their unconditional support.

It's a pleasure to acknowledge the contributions of Joseph Ojwang (my second father) for his prayers and unconditional support, to all members of the Economic Geology Laboratory special for Dr. Pearlyn Manalo and Dr. Hinako Sato (for providing laboratory and fieldwork assistance), for their help, support, encouragement and constructive suggestions and recommendations during our stay at Akita University.

To my parents, Francisco Paulo Cossa and Esperança Inês Joao Cossa for having invented dreams in me and for having bet on my education at the beginning of everything even if this act of courage meant a morning without bread on the table, I will be forever thankful. To Ivo and Nicha, my little ones, my gratitude for being always there for me. Without their affection and support, I wouldn't be here. My family and friends that have been praying for me during this period.

Last but not least, I would like to take this opportunity to thank Oishi Simon Ojwang for his fellowship, for the encouragement, support, help, happiness he has given me throughout this period.

## Contents

<b>1. INTRODUCTION</b> .....	<b>15</b>
1.1 Previous studies .....	17
1.2 Objectives of the study .....	19
1.3 Location, accessibility and physiography .....	20
<b>2. GEOLOGY BACKGROUND</b> .....	<b>21</b>
2.1 Tectonic Setting .....	24
2.2 Regional Geology .....	26
2.3 Local Geology .....	28
3. Geology of the Deposits .....	29
<b>3. METHODOS</b> .....	<b>33</b>
3.1 Sampling .....	33
3.1.1 Desktop Studies .....	<b>33</b>
3.2 Fieldwork .....	34
3.3 Analytical Methods .....	34
Petrography (Microscopy observation) .....	<b>34</b>
Preparation of powder samples, pellets .....	<b>37</b>
X-ray diaffraction (XRD) .....	37
3.3.6 Scanning Electron Microscope Analysis (JEOL JSM-IT300) .....	<b>41</b>
Fluid inclusion microthermometry .....	<b>41</b>
Electron Microscope analyses – EPMA .....	<b>41</b>
Microthermometry .....	<b>42</b>
<b>4. RESULTS</b> .....	<b>44</b>
4.1 MUGOMO DEPOSIT .....	44
4.1.1 CHARACTERISTICS OF THE HOST ROCKS .....	<b>45</b>
4.1.2 Hydrothermal alteration .....	<b>47</b>
4.1.3 Geochemistry of the host rock .....	<b>48</b>
4.1.4 Rare Earth Element (REE) .....	51
4.1.5 ORE MINERALOGY .....	<b>53</b>
4.1.6 Trace elements characteristics .....	56
.....	<b>57</b>
4.1.7 Petrography of fluid inclusion .....	58

4.2 Chifumbazi deposit .....	64
4.2.1 Petrography of the host rock .....	65
4.2.2 Hydrothermal alteration .....	68
4.2.3 Geochemistry of host rock.....	69
4.2.4 Ore occurrence and petrography of Chifumbazi deposit .....	74
4.2.5 Trace element concentrations in quartz .....	81
4.2.6 Petrography of fluid inclusions.....	84
4.2.7 Sulfur isotopes.....	90
5. DISCUSSION .....	91
5.1 Hydrothermal alteration.....	91
5.2 Evolution of the mineralizing fluid .....	91
5.3 The formation of chlorite and epidote veins .....	92
5.4 Tectonic Setting .....	94
5.5 Comparison between the veins and shear zones.....	96
5.6 Type of mineralization .....	97
5.7 Ore-forming conditions.....	100
5.8 Implication to the mineral exploration.....	103
6. CONCLUSIONS .....	104
7. REFERENCES .....	106
8. APPENDICES.....	117
Appendix 1 .....	XIV
APPENDIX 1.1. Field observation and host rock characteristics of the Mugomo deposit....	XV
APPENDIX 1.2.1 Field observation and host rock characteristics of the Chifumbazi deposit .....	XXIV
Appendix 2.....	XXX
Mugomo deposit .....	XXX
Appendix 3.....	XXXVII
Chifumbazi deposit.....	XXXVII

## List of Figures

- Figure 1: Tectonic setting of all types of gold deposits. The orogenic gold is emplaced during compressional to transpressional regimes and throughout much of the upper crust, in deformed accretionary Belts adjacent to continental magmatic arcs (adapted from Groves et al., 1997). ..... 17
- Figure 2: Recommended areas for further exploration and follow-up surveys. Interpretation is based on the geochemical data compiled during the Hunting Project in Tete Province (modified from Korkiakoski, 2008)...... 19
- Figure 3: a) Distribution of Mesoproterozoic lithologies and orogenic Belts in central and southern Africa (adapted from Dirks & Ashwal, 2003); b) Geodynamic model showing the sequence of tectono-metamorphic events during the Irumide orogeny and an overview map of the Southern Irumide Belt (adapted from Karmakara & Schenk, 2016)...... 23
- Figure 4: Simplified geological map of the Tete-Chipata Belt and the Zambezi-Lufilian segment of the Damara-Lufilian-Zambezi Belt (modified from Westerhof, 2008). ID: 1- East Gondwana; 2- West Gondwana; 3- South Gondwana; MD = Mwembeshi Dislocation, SSZ = Sanangoè Shear Zone, NMS = Namama Mega ..... 25
- Figure 5: Distribution of Mesoproterozoic granitoids of the Tete Chipata Belt, grouped into several granitoid clans and a bi-modal suite emplaced during the Grenvillian orogeny (GTK Consortium, 2006; Mänttari, 2008) and Early Pan-African intrusive rocks (Matunda Suite) in Tete Province (modified after Sterk et al., 2018). Key: A = Angonia; BG = Brown granite; CG = Chacocoma Granite; CHS = Chiuta Serra; CSS = Cassacatiza Suite; FS = Furancungo Suite; MC = Monte Capirimpica; MI = Monte Inchinga; MS = Mesoproterozoic Schist; MS01 = Matunda Suite; MSS = Monte Sanja Suite; PA = Pan African Intrusion; RC = Rio Capoche; RT = Rio Tchafuro; SD = Serra Danvura; TS = Tete Suite. .... 27
- Figure 6: Local geology surrounding the Chifumbazi and Mugomo deposits (modified from GTK consortium, 2006)...... 28
- Figure 7: Photographs of the host rocks at the Mugomo deposit showing a) quartzite; b) biotite-schist; c) metavolcanic rock crosscut by quartz-epidote-chlorite veins. .... 29



- Figure 8: Photos of the host rocks and country rocks at the Chifumbazi deposit: gneiss in discordant contact with meta-granodiorite (quartz-mica-schist)..... 31
- Figure 9: Calibration curve for sulfur isotope standards. Referenced to table 2 above. 40
- Figure 10: Fluid inclusion calibration curves applied for the microthermometry data correction. 1. CO<sub>2</sub> calibration curve; 2. Calibration curve of melting ice temperature (T<sub>m</sub>) curve; 3. Calibration curve of homogenization temperature (T<sub>h</sub>). ..... 43
- Figure 11: Photomicrographs with transmitted light and crossed polars of the host rocks in the Mugomo deposit: (a,b) a quartzite with granoblastic texture composed of quartz and plagioclase; (c) a quartzite composed of plagioclase and quartz with chlorite alteration crosscut by epidote veinlet; (d) a metavolcanic rock with granoblastic texture composed of plagioclase, biotite, and muscovite; (e) a metavolcanic rock composed of plagioclase, epidote, and sericite alteration; (f) a metavolcanic rock composed of plagioclase, epidote, chlorite and calcite alterations; (g) a metavolcanic rock composed of plagioclase, and epidote; (h) a biotite-schist with lepidoblastic texture, composed of biotite and quart. Abbreviations are pl: plagioclase, qz: quartz, bt: biotite, mus: muscovite, chl: chlorite, ser: sericite..... 47
- Figure 12: Harker diagrams of major elements oxides of host rock from Mugomo deposit and Mualadzi group. *CaO*, Na<sub>2</sub>O, K<sub>2</sub>O, Rb, Ba, and Sr are not considered, since their concentrations *might* have changed significantly during the Pan-African Orogeny (*e.g* Johnson et al., 2007)..... 49
- Figure 13: Discrimination diagram of the Mugomo deposit host rock based on immobile elements Zr/Ti and Nb/Y (modified from Pearce, 1996). ..... 50
- Figure 14: Chondrite-normalized REE pattern (a) and primitive mantle-normalized trace elements and (b) of chondrite values from Sun McDonough (1989)..... 52
- Figure 15: Photomicrographs ore minerals of the Mugomo deposit. a) Subhedral pyrite crystal and chalcopyrite; b) subhedral crystals of pyrite intergrown with chalcopyrite with covellite replacement; c) native gold inclusions in pyrite crystal with chalcopyrite; d) backscattered electron image of bornite intergrown with Fe-Co-mineral; e) magnetite intergrown with chalcopyrite and covellite replacement; f) backscattered electron image showing euhedral crystals of pyrite with Bi-telluride and Ag-telluride filling micro-fractures in pyrite; Abbreviations: py – pyrite; sp –

sphalerite; ccp – chalcopyrite; mg – magnetite; gn – galena; cv – covellite; BiTe – bismuth telluride; AgTe – silver telluride, Au - gold.....	54
Figure 16: A simplified paragenetic sequence of mineralization and alteration in the Mugomo deposit.....	55
Figure 17: Gold, Ag, Cu, Co, Ni, and Pb contents of metavolcanic rock and epidote quartz veins from the Mugomo deposit, determined by the ICP-MS analytical method...	56
Figure 18: Hand specimen photos and photomicrographs of Mugomo deposit showing a) mineralized quartz and epidote vein; b) euhedral quartz cross-cutting by chlorite and clay minerals; c) quartz vein cross-cutting metavolcanic rock; d) mozaic quartz texture.....	57
Figure 19: Photomicrographs of fluid inclusions at the Mugomo deposit at room temperature (a) type I fluid inclusion (b) large individual fluids inclusions; (c) type II inclusions with long and regular shape; (d) irregular type III multi-phase inclusion composed of 3 phases inclusions L+V+S. ....	59
Figure 20: Histograms of homogenization temperatures (Th) and salinity of fluid inclusion type II in quartz veins of the Mugomo deposit.....	61
Figure 21: Homogenization temperatures versus salinity plot for the fluid inclusions of the Mugomo deposit.....	62
Figure 22: A histogram of $\delta^{34}\text{S}$ (‰) data for pyrite from the Mugomo deposit.....	63
Figure 23: Photos of the host rock and country rocks at the Chifumbazi deposit: (a) gneiss in discordant contact with quartz-mica-schist; (b) gneiss without vein; and (c) quartz-mica-schist cut by milky quartz veins. ....	66
Figure 24: Photomicrographs with transmitted light and crossed polars of the host rocks in the Chifumbazi prospect: (a) a gneiss with lepidoblastic texture composed of quartz and muscovite; (b) a quartz-mica-schist composed of plagioclase and quartz with sericite and chlorite alteration; (c) a quartz-mica-schist composed of plagioclase, quartz, muscovite with calcite and chlorite as alteration; (d) a quartz-mica-schist composed of plagioclase, rutile, quartz, actinolite and pyrite; (e) a quartz-mica-schist composed of quartz, chlorite, pyrite associated with sericite and chlorite alteration; (f) a quartz-mica-schist composed of quartz, plagioclase, muscovite, pyrite associated with sericite alteration. Abbreviations are pl: plagioclase, qz:	

quartz, bt: biotite, mus: muscovite, rt: rutile, chl: chlorite, ser: sericite, act: actinolite, op: opaque minerals, py: pyrite .....	67
Figure 25: Ternary plots of carbonates composition in the $\text{FeCO}_3\text{--CaCO}_3\text{--MgCO}_3$ apices from the quartz-mica-schist from the Chifumbazi deposit analyzed by EPMA. ....	69
Figure 26: Harker diagrams for whole-rock chemical compositions of quartz-mica-schist in the Chifumbazi deposit and meta-diorite and quartz-mica-schist in Zambia belonging to the Southern Irumide Belt. The data of meta-diorite and quartz-mica- schist in Zambia are taken from Johnson et al. (2007).....	71
Figure 27: Zr/Ti versus Nb/Y plot (after Pearce 1996) for the quartz mica schist from the Chifumbazi deposit, meta-granodiorite and meta-diorite of Zambia. ....	72
Figure 28: Diagrams of chondrite-normalized REE patterns (a), and primitive mantle- normalized trace element patterns (b) of quartz-mica-schist in the Chifumbazi deposit. Normalization values are from Sun and McDonough (1989). ....	73
Figure 29: Photos of an outcrop and hand specimen samples from the Chifumbazi deposit: (a) meta-granodiorite cut by shear zones and veins with E–W, SW–NE and NNW– SSE directions; (b) a clear quartz (CQ) veins in contact with a quartz-carbonate (QC) vein and chlorite veinlets cutting the CQ veins; (c) a QC vein occurring together with milky quartz (MQ) vein. The CQ vein was cut perpendicularly by a small fault that does not crosscut MQ vein, indicating that the MQ vein was formed after QC vein; (d) chlorite associated with ferruginous quartz (FQ) vein; and (e) altered meta- granodiorite hosting a chlorite-pyrite veinlet parallel to the foliation of rock, which cut a CQ vein.....	75
Figure 30: Photomicrographs with transmitted light and crossed polars: (a) dolomite and sericite surrounding quartz in a quartz-carbonate (QC) and milky quartz (MQ) veins; (b) coexisting quartz, calcite and ankerite with minor chlorite in a quartz-carbonate (QC) vein; (c) quartz, minor calcite, muscovite and albite enveloping quartz in a milky quartz (MQ) vein; (d) calcite filling interstices of quartz grains in a milky quartz (MQ) vein. Abbreviations are al: albite, qz: quartz, mus: muscovite, chl: chlorite, ser: sericite, ank: ankerite, cal: calcite, dol: dolomite.....	76
Figure 31: Reflected light photomicrographs and backscattered electron image of the sulfides of different mineralization stages in the Chifumbazi deposit: (a) chalcopyrite	

occurring as inclusions or filling microfractures in pyrite (Stage I); (b) a backscattered electron image of bornite and galena overgrowing pyrite (Stage I); (c) pyrrhotite, chalcopyrite and pyrite intergrown in a quartz vein (Stage II); (d) chalcopyrite intergrown with pyrite which partially replaced anhedral pyrrhotite (Stage II); (e-f) pyrite intergrown with chalcopyrite, with inclusions of native gold and chalcopyrite within pyrite (Stage II) a rectangle in (e) is enlarged in (f); (g) euhedral pyrite of Stage III with features; and (h) chalcopyrite of Stage I partially replaced by covellite of Stage IV. Abbreviations are Au: native gold; ccp: chalcopyrite, po: pyrrhotite, py: pyrite, bn: bornite, cv: covellite..... 78

Figure 32: Paragenetic sequence of mineralization in the Chifumbazi deposit.

Abbreviations are QC: quartz-carbonate vein; MQ: milky quartz vein, CQ: clear quartz vein; and FQ: ferruginous quartz vein..... 79

Figure 33: Gold, Ag, Cu, Pb, Co, Te, Ni, and Zn contents of the clear quartz (CQ) veins in Stage II from the Chifumbazi deposit, determined by ICP-MS analysis..... 80

Figure 34: Histograms of the trace element contents of quartz based on EPMA analysis for clear quartz (CQ) and ferruginous quartz (FQ) veins of Stage II in the Chifumbazi deposit. .... 82

Figure 35: (a) Al/K versus Al and (b) Al/Fe vs Al in clear quartz (CQ) and ferruginous quartz (FQ) veins of the Chifumbazi deposit. .... 83

Figure 36: Photomicrographs showing fluid inclusions in quartz veins of Stage II of the Chifumbazi deposit: (a, b) fluid inclusions of aqueous one-phase (liquid) (Types I), aqueous two-phase (vapor-liquid) inclusions (Type II), and aqueous-CO<sub>2</sub> one-phase (vapor) and/or two-phase (vapor-liquid) inclusions (Type III); (c, d) isolated Type II fluid inclusions in quartz crystals; (e) Raman spectra of a Type III fluid inclusion showing the presence of CO<sub>2</sub>. .... 86

Figure 37: Histograms of homogenization temperatures (Th) and salinity of fluid inclusion type II in quartz veins of the Chifumbazi deposit. .... 88

Figure 38: Homogenization temperatures versus salinity plot for the fluid inclusions of Stage II from the Chifumbazi deposit. .... 89

Figure 39: A histogram of sulfur isotope compositions of sulfides from the Chifumbazi deposit. .... 90

Figure 40: Diagrams of primitive mantle-normalized trace element patterns (a) of metavolcanic rocks in the Mugomo deposit compared with the arc rhyolite from the Okataina deposit (data from Deering et al., 2011); (b) of quartz-mica-schist in the Chifumbazi deposit compared to granitoids from the Furancungo Suite (data from GTK consortium, 2006) and Okataina deposit (data from Deering et al., 2011);. Normalization values are from Sun and McDonough (1989).....	95
Figure 41: Geodynamic model showing the sequence of tectonic-metamorphic events during the Irumide orogeny and an overview map of the Southern Irumide Belt (Karmakara & Schenk, 2016).....	96
Figure 42: Stereonet (lower hemisphere) of vein orientations at Mugomo and Chifumbazi deposits.....	97
Figure 43: Comparison of sulfur isotopic ratios of primary mineralization in the Mugomo and Chifumbazi deposits with other orogenic gold deposits worldwide. ....	98
Figure 44: Aluminum versus Ti contents of quartz of clear quartz (CQ) and ferruginous quartz (FQ) veins of Stage II of the Chifumbazi deposit with comparison to those of hydrothermal quartz from epithermal, orogenic, and porphyry deposits (modified after Rusk, 2012; Sun et al., 2021).....	100
Figure 45: Homogenization temperatures versus salinity plot for the fluid inclusions of type II from the Mugomo and Chifumbazi deposits. ....	103

## List of tables

Table 1: Calibrated $\delta^{34}\text{S}$ results from sulfur isotope standards .....	40
Table 2: Summary of final melting temperature ( $^{\circ}\text{C}$ ) and known final melting temperature ( $^{\circ}\text{C}$ ) of the selected chemicals for the calibration of the Linkam 10035 freezing and heating stage.....	42
Table 4: Whole rock chemical compositions of metavolcanic rock from the Mugomo deposit. Units are wt% for major oxides and ppm for other elements. ....	XXXI
Table 5: Whole rock chemical compositions of mafic metavolcanic rocks from the Mualadzi group. Units are wt% for major oxides ppm for other elements. Data from GTK consortium, 2006.....	XXXII
Table 6: Whole rock trace and rare-earth element compositions for some selected samples of metavolcanic rock from the Mugomo deposit. ....	XXXIII
Table 7: Transition metal and metalloids compositions for some selected samples of metavolcanic rock from the Mugomo deposit.....	XXXIV
Table 12: Whole rock trace element compositions of veins from the Chifumbazi deposit. ....	XL
Table 13: Transition metal and metalloids compositions for some selected samples the Chifumbazi deposit .....	XLI
Table 14: Microthermometry data of Type II inclusions of the Chifumbazi deposit	XXXI

## 1. INTRODUCTION

Gold is a precious metal that is relatively scarce on Earth and occurs in different geological environments (Kirkemo et al., 2017) such as orogenic, porphyry, volcanogenic massive sulfide, epithermal and skarn deposits.

The origin of orogenic gold mineralization is associated with regionally metamorphosed terranes of all ages (Groves et al., 1997). During the compressional to transpressional deformation processes at convergent plate margins, accretionary and collisional orogens ores minerals were formed (Figure. 1), (Groves et al., 1997).

According to Groves et al. (2003), the metamorphic belts are complex regions where the continental crust has been added to or thickened by accretion or collision (Groves et al., 2003). Mineralization can be formed at all stages of orogen evolution, so evolving metamorphic belts contain diverse gold deposit

types that may be juxtaposed or overprinted (Groves et al., 2003). There is a high-level controversy on the origin of some deposit types, particularly those formed or overprinted/remobilized during the major compressional orogeny that shaped the final geometry of the hosting metamorphic belts (Groves et al., 2003), which means that gold mineralization formed in metamorphic environment are diverse in terms of age (Middle Archean to Tertiary), geometry (single to arrays veins, stratabound replacement to disseminated deposits), structural controls (reverse to strike-slip, and, less commonly, normal faults), host rocks (mafic ultramafic rock sequences, sedimentary rocks, or granitoid plutons), metamorphic grade of host rocks (sub-greenbiotite-schist to granulite facies, although mainly greenbiotite-schist facies), temperature and pressure of formation ( $\approx 200$  to  $650^\circ\text{C}$ ; 0.5 to 5 kbars), and consequent whole-rock alteration assemblages (carbonate to diopside, muscovite to biotite or phlogopite) and metal associations (Au with variable Ag, As, B, Bi, Cu, Pb, Sb, Te, W, and Zn) (Groves et al., 2003).

Tete Province is occupied by a large area of Mesoproterozoic supracrustal rocks north of the Sânanço Shear Zone (Pekkala et al., 2008; Westerhof, 2008), belonging to the

Southern Irumide Belt also known as Tete Chipata Belt (Figure. 4) (Westerhof, 2008). The rocks are mainly metasandstones, quartz-feldspar gneisses and felsic to mafic metavolcanic rocks (Pekkala et al., 2008). All these rocks are intruded by felsic plutonic rocks during the Grenvillian orogeny cycle (1350 – 1000 Ma) and are metamorphosed from low-amphibolite to granulite facies (Pekkala et al., 2008; Westerhof, 2008).

This study aims to understand the characteristics of gold mineralization and the hydrothermal alteration in two at such gold occurrences, namely the Mugomo and Chifumbazi deposits in Chifunde district, northwestern Mozambique.

At the Chifumbazi deposit, the ores occur as quartz veins, lenses, and breccia within shear zones (Lächelt, 2004). These zones intersect hornblende augen gneisses or hornblende quartz-mica-schists (Lächelt, 2004). Gold appears as native gold or is invisible gold in pyrite and occasionally in chalcopyrite (Lächelt, 2004). Silver is also present, but rare (Lächelt, 2004). The veins consist predominantly of quartz and are partly calcitic and chloritic, associated with an extensive epidotisation, silicification and were subjected to argillaceous weathering (Lächelt, 2004)

The Mugomo deposit lies between quartzites, slates, and porphyry granite gneisses intersected by felsic intrusions (Lächelt, 2004). Gold occurs between the quartz interstices as native gold or in association with Fe mineralization (Lächelt, 2004). At deeper parts of the deposit, gold is associated

with pyrite and pyrrhotite (Lächelt, 2004). The metamorphic rocks at the Tete Chipata Belt have a large number of gold occurrences (GTK consortium, 2006; Lächelt, 2004) for which little specific information is available.



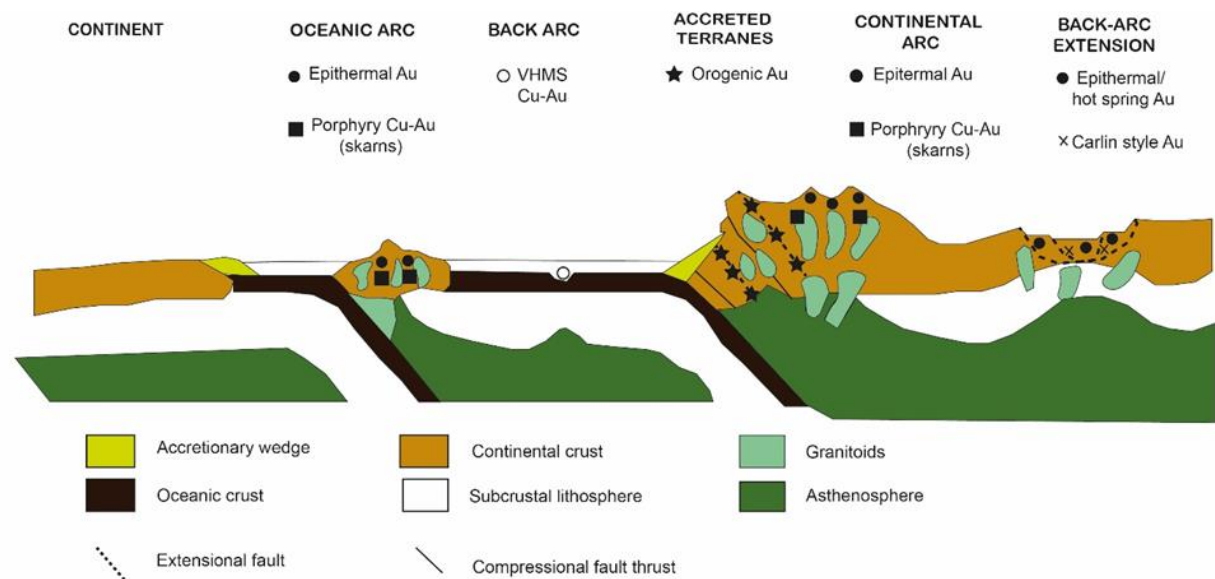


**Figure 1:** Tectonic setting of all types of gold deposits. The orogenic gold is emplaced during compressional to transpressional regimes and throughout much of the upper crust, in deformed accretionary Belts adjacent to continental magmatic arcs (adapted from Groves et al., 1997).

### 1.1 Previous studies

The northern part of Tete Province is characterized by the crystalline rocks of the basement that is mostly composed of Mesoproterozoic granitoids with Neoproterozoic to Ordovician granitoids occurring to a smaller areal extent (Mäkitie, 2008).

The gold occurrences in the northwestern part of the Tete province are characterized by Mesoproterozoic rocks (Lächelt 2004). Host rocks are formed by quartzites within shear zones and mineralized veins occur between Fe-quartzites and talc–chlorite–actinolite biotite-schists (Lächelt 2004). There is uncertainty about the gold grades because the gold deposits were not well studied and there is no available information about the gold recovered.

The geochemical surveys carried out by the Hunting Team from 1981 to 1983 were concentrated in 20 selected target areas in Tete province (Figure. 2) (Korkiakoski, 2008). Although, 1066 samples were analyzed for Au, Pd, and Te (Korkiakoski, 2008), only 19 % of samples had Au values above the detection limit of 0.5 ppb (Korkiakoski, 2008). This proportion is lower than that obtained from stream sediment sampling by the Geological Survey in Mozambique project, where 36 % of the Au values exceeded 0.5 ppb (Korkiakoski, 2008).

At the Chifumbazi deposit, the ores occur in quartz veins (Lächelt, 2004, GTK consortium, 2006). These zones intersect hornblende augen-gneisses or hornblende quartz-micaschists (GTK consortium, 2006). Gold appears as native gold or is assimilated by pyrite and occasionally by chalcopyrite (GTK consortium, 2006). Silver is also present, but rare (GTK consortium, 2006). The veins consist mostly of quartz and are partly calcitic and chloritic, associated with an extensive epidotisation, silicatisation and were subjected to argillaceous weathering (Lächelt, 2004). The area around the Chifumbazi deposit is characterized by auriferous ferruginous quartzites with layers ranging from 1 m to 30 m (Svirine, 1978, Ferreira, 1939, Freitas, 1949, Ribeiro, 1958). Different gold grades were reported by several authors (Ferreira, 1939, reported gold grade of 15 – 20 g/t; Freitas, 1949, reported gold grade of 0,35 g/m<sup>3</sup> and Ribeiro, 1958, reported gold grade of 2,7g/t and 2,29 – 5 g/t. 0,5g/t - 0,14 g/t; Svirine, 1978). The gold was observed also in quartz-carbonate veins, biotite-hornblende gneiss as native gold associated with pyrite and chalcopyrite with the gold grades varying between 4 and 14 g/t (GTK consortium, 2006).

The Mugomo deposit lies between quartzites, slates, and porphyry granite-gneisses that are intersected by felsic intrusions (GTK consortium, 2006). Gold appears between the quartz interstices as native gold or in association with Fe-mineralization (GTK consortium, 2006). At the deeper parts of the deposit, gold is associated with pyrite and pyrrhotite (GTK consortium, 2006).

The native gold is associated with Fe-mineralizations with gold grade varying 4g/t or 6-12 g/t (Lächelt, 2004). E-W trending sericitic quartzite and sericite biotite-schist with pyrite are enriched with gold along NNE striking fractures (Lächelt, 2004). In the oxidized zone gold is either native or associated with iron oxides, in the deeper parts of

the deposit, where the grade of gold 3.15 g/t, gold is associated with pyrite and pyrrhotite (Lächelt, 2004).

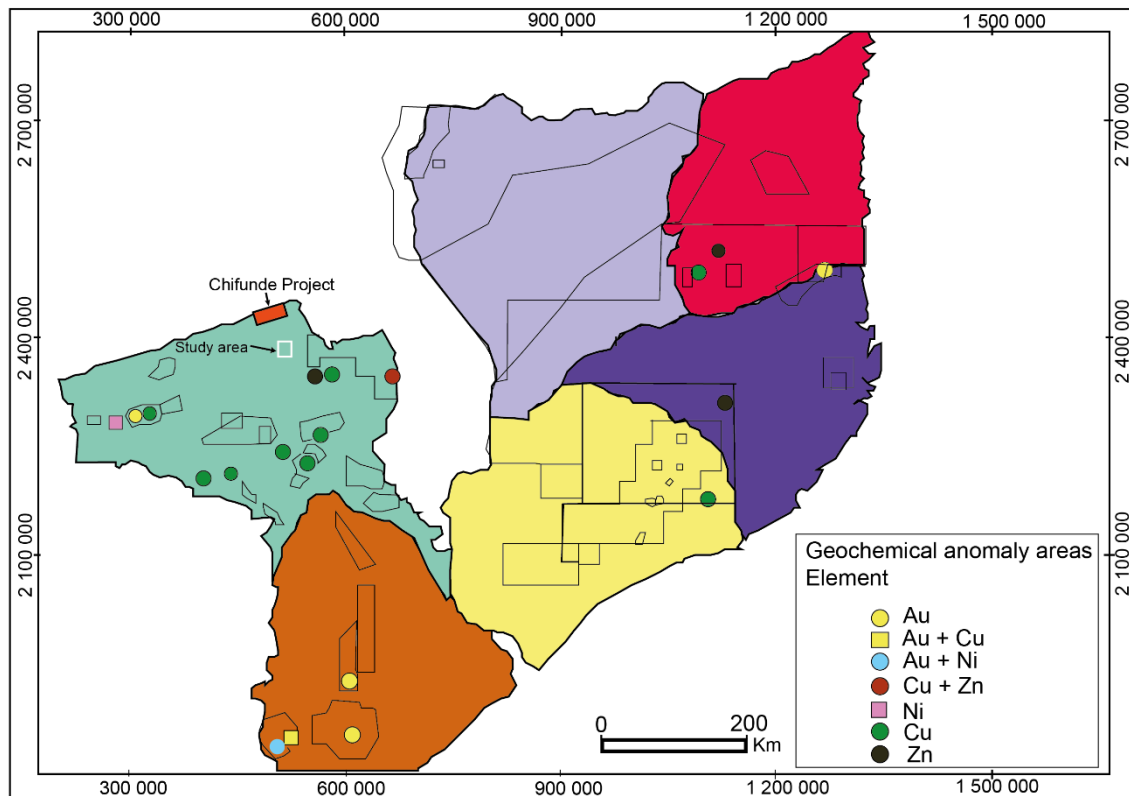


**Figure 2:** Recommended areas for further exploration and follow-up surveys. Interpretation is based on the geochemical data compiled during the Hunting Project in Tete Province (modified from Korikiakoski, 2008).

## 1.2 Objectives of the study

Mozambique has a big untapped mineral potential. Recently, gold deposits in the central and northern part of the country have attracted domestic and international investors, but so far, gold has only been exploited by informal artisanal miners in some deposits. However, these deposits are not well studied. Thus, the aims of this study are:

- To investigate the mineral and rock geochemistry of the Chifumbazi and Mugomo deposits;

- To investigate the characteristics of gold mineralization and the hydrothermal alteration in both deposits;
- Determine the ore mineral paragenetic sequence in both deposits ;
- Understand the source of the mineralizing fluids in both deposits;

### **1.3 Location, accessibility and physiography**

The Chifumbazi and Mugomo deposits are located in Tete Province, Chifunde district, western Mozambique, which borders with Zambia in the north, Malawi in the northeast, Macanga district in the east, Chiuta district in the south, and with Marávia district in the west (Ministerio de Administracao Estatal, MAE, 2005). The Chifumbazi deposit is centred at S -14.40127 and E 33.01325 coordinates, and the Mugomo deposit lies at S - 14.22962 and E 32. 59201.

The Chifunde district is characterized by rainy tropical savanna climate, annual average rainfall is above 800 mm, reaching in most cases to about 1200 or even 1400 mm. Annual average temperatures range from 24 to 26 °C (MAE, 2005). To the north, it is covered by humid temperate climate strongly influenced by altitude. The average annual precipitation is above 1200mm and the average temperature varies between 15 °C to 22.5 °C (MAE, 2005).

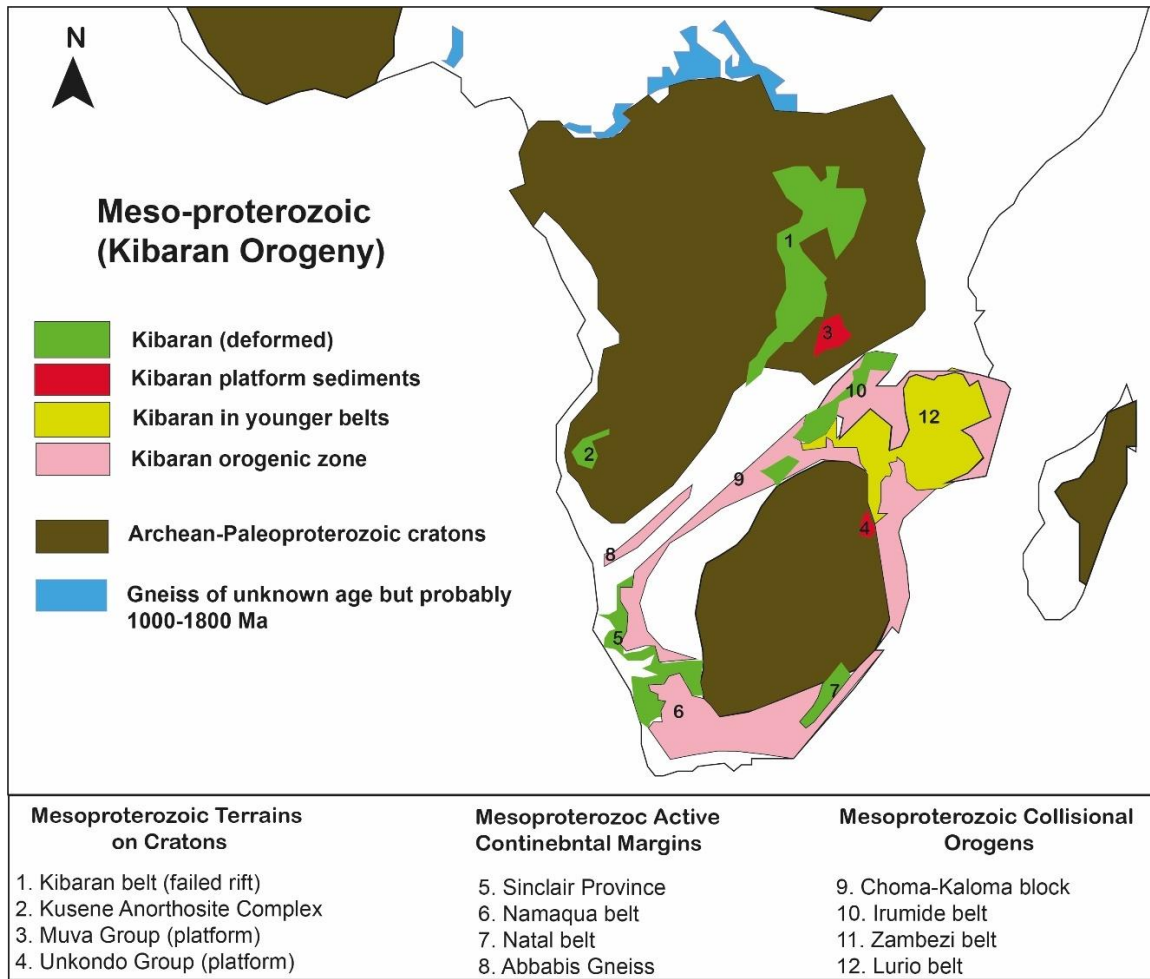
The southern zone of the district is characterized by an average altitude ranging from 100 to 200 m above sea level (MAE, 2005). However, in the northern part of the district, the topography is high and very undulating and dissected, the relief is dominated by interspersed interfluvial through narrow and very deep valleys, and inselberg rock outcrops occur in isolation (MAE, 2005).

## 2. GEOLOGY BACKGROUND

Tete Province is geologically divided into three major lithospheric plates: the Mesoproterozoic West Gondwana basement, which has undergone the Kibarian orogeny in the north with minor East Gondwana assemblages in the northeastern corner; the Archaean Zimbabwe craton with Proterozoic cover sequences occur in the south; and the Phanerozoic graben-type sediments of the Zambezi rift (parallel to Cahora Bassa Lake) are located between these basement areas (Figures. 4-5) (Rogers et al., 1995, Grantham et al., 2003, GTK Consortium 2006d, Mäkitie et al., 2008).

According to Mäkitie et al. (2008) the Tete Suite is a layered gabbro-anorthosite intrusive that overlies mylonitized crystalline basement belonging to two Pan-African lithospheric plates, and is supposedly derived from the West Gondwana plate. The West Gondwana terrane in the northern Tete Province continues to Zambia, where it is called as Southern Irumide Belt (Johnson et al., 2005, 2007; Mäkitie et al., 2008). The Mwembeshi Dislocation separates the southern Irumide Belt from the NE-SW trending Irumide Belt to the rest of Central African craton (Figure. 4) (Mäkitie et al., 2008). In the Central Africa craton, the Irumide Belt manifests Grenvillian convergent tectonism along the southeastern margin of the crystalline basement of Tete province (De Waele et al., 2006) and is characterized of Paleoproterozoic metamorphosed platform sediments of the ~1.88 Ga Muva Supergroup (De Waele & Fitzsimons, 2004, Mäkitie et al., 2008), which are most conspicuously exposed along the NW-verging Irumide, in the northwestern part of the Belt (Westerhof et al., 2008).

The Desaranhama Granite ( $1041 \pm 4$  Ma zircon U-Pb) and orthogneisses of the Furancungo Suite (GTK consortium, 2006, Mänttari, 2008, Westerhof et al., 2008) belong to the West Gondwana terrane and have a NW-SE trend (Westerhof et al., 2008). However, they show progressive deformation from W to E, towards the thrust front with the Angonia Group, the rock fabric changes from rather massive to augen gneiss to blastomylonite (GTK consortium, 2006, Mäkitie et al., 2008, Westerhof et al., 2008). Assuming a Pan-African, NW-SE striking fabric, the Furancungo Suite is the footwall of the Angonia thrust mass (Westerhof et al., 2008).



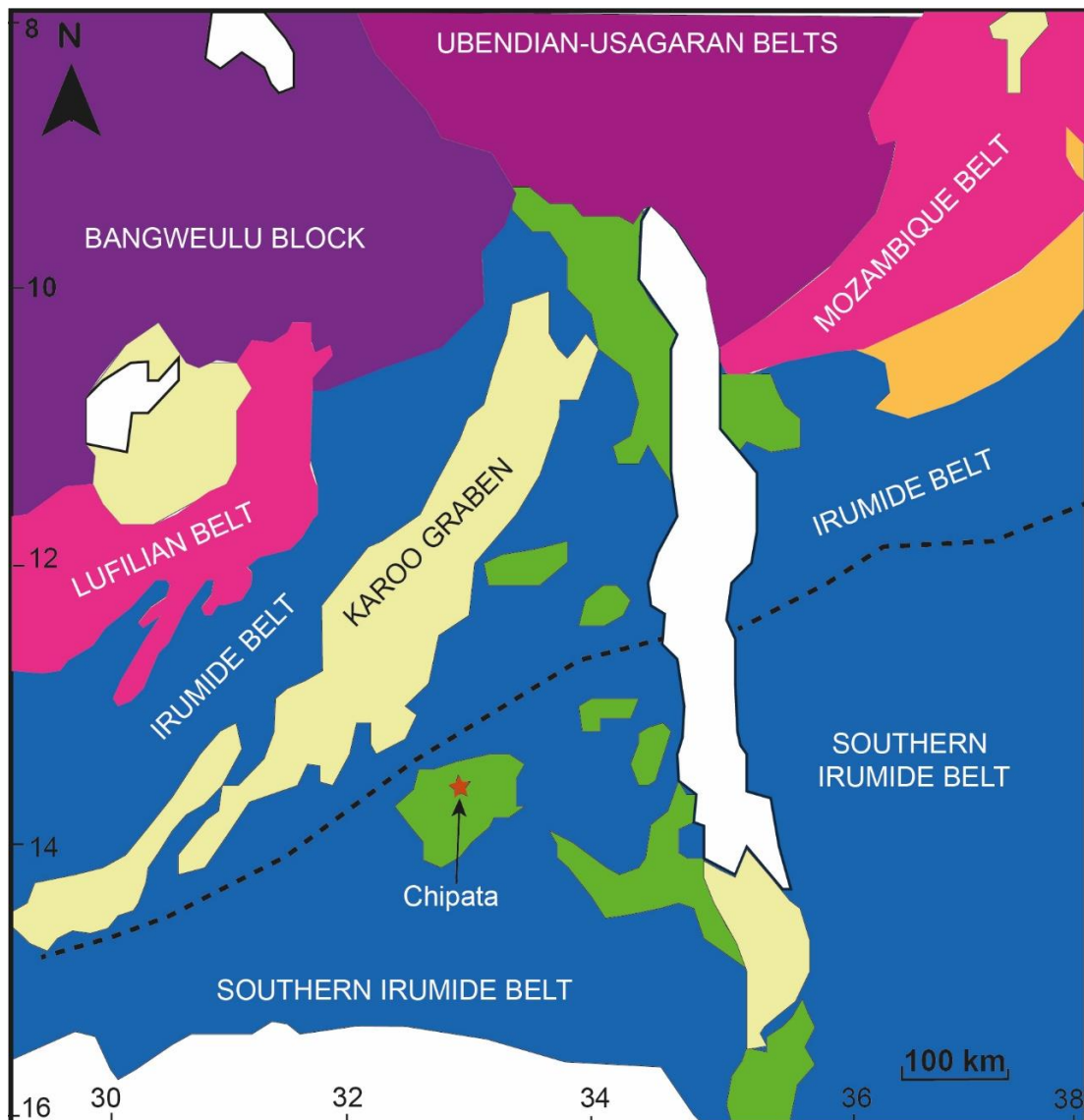


**Figure 3:** a) Distribution of Mesoproterozoic lithologies and orogenic Belts in central and southern Africa (adapted from Dirks & Ashwal, 2003); b) Geodynamic model showing the sequence of tectono-metamorphic events during the Irumide orogeny and an overview map of the Southern Irumide Belt (adapted from Karmakara & Schenk, 2016).

## **2.1 Tectonic Setting**

### **The Irumide Belt**

The Mesoproterozoic Irumide Belt is located in the southern margin of the Bangweulu Block and is a NE–SW trending Mesoproterozoic orogenic Belt, comprised of deformed Paleoproterozoic granitic basement, folded metasedimentary units and voluminous granitoid intrusions of ca. 1.05–1.00 Ga age (De Waele et al., 2006a). The peak of metamorphism is represented by upper-amphibolite facies (7–8 kbar and ~650 °C) mineral assemblages and is interpreted to have occurred at 1020 Ma (De Waele, 2004). The peak of metamorphism is coincident with large scale structural overprinting along the southern margin of the Belt and by the intrusion of primarily calc-alkaline granitoid rocks (Alessio et al., 2018). The lack of juvenile material in the Irumide Belt suggests that the Belt acted as a passive margin on the southeast margin of the Congo Craton and that the active continental margin was represented by the Southern Irumide Belt further in the south (De Waele et al., 2006b).

### **The Southern Irumide Belt**

The Mesoproterozoic rock south of the Southern Irumide Belt (SIB) has been considered as part of the Mozambique Belt, also called as the Tete Chipata Belt (Figure. 3) (Johnson et al., 2005 and Karmakara & Schenk, 2016). Lithologies of the SIB crop out in Zambia, Malawi, Mozambique, and Tanzania, (Johnson et al., 2006). In Zambia, the SIB is located in the south of the Irumide Belt, though any continuity or discontinuity between the Southern Irumide Belt and Irumide Belt is obscured by a Permo-Triassic Karoo Graben that forms the Luangwa Valley (Johnson et al., 2006). In northwest Mozambique (Tete Province), the SIB has been subdivided into a series of terranes with supracrustal sequences that display little cohesion and granitoids with ages ranging from ca. 1.2 to 1.05 Ga (Westerhof et al., 2008). However, this complex is instead interpreted to have been accreted to the Kalahari Craton prior to Congo–Kalahari collision (Macey et al., 2010). The collision's result is the current position, separated from the other Mesoproterozoic complexes by the WSW–ENE trending Lurio Belt that is suggested to represent a suture zone between the Congo and Kalahari cratons (Bingen et al., 2009). Irumide structural trends, in the Mozambique Belt, have been largely obliterated during



Pan-African tectonothermal events (De Waele et al., 2001). In the Chipata area of the Mozambique Belt, granulite facies rocks are older than 2000 Ma, and may represent a remnant of Archean crust that could have formed the eastern base ment to the Irumide Basin (De Waele et al., 2001).

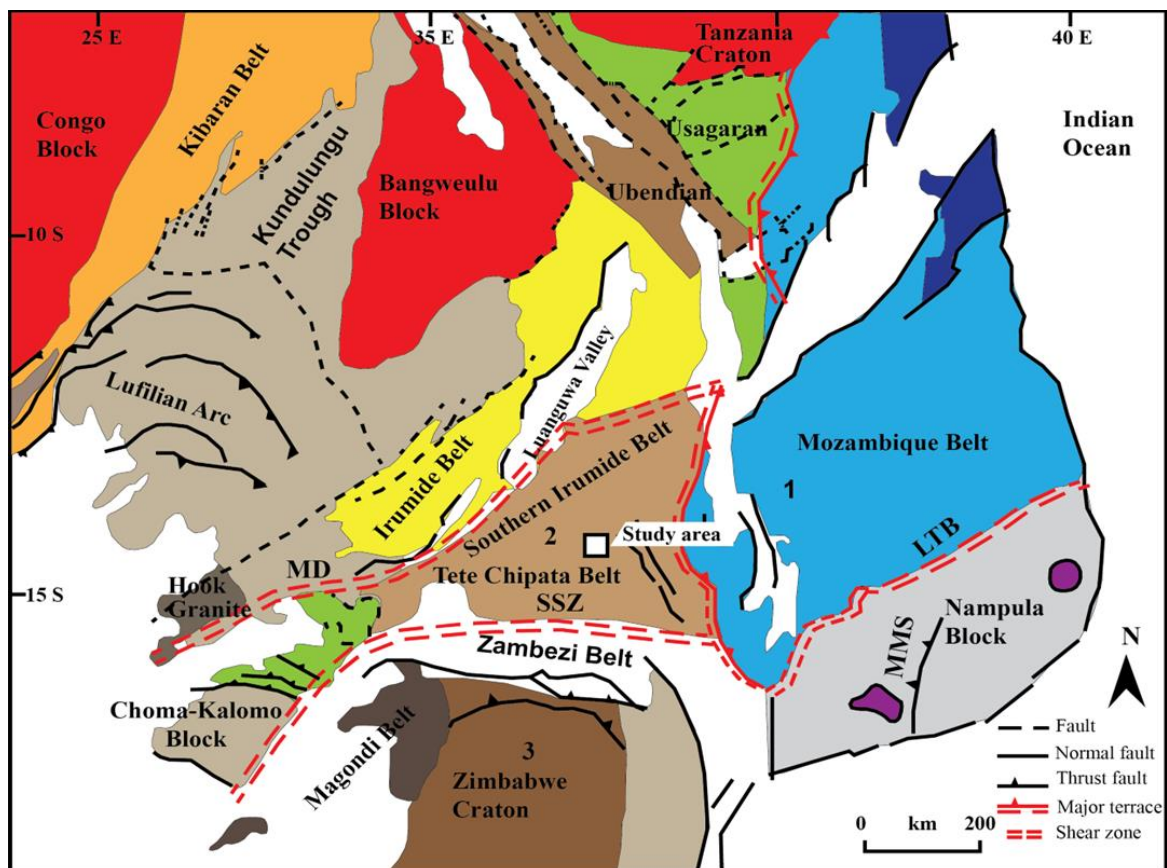


**Figure 4:** Simplified geological map of the Tete-Chipata Belt and the Zambezi-Lufilian segment of the Damara-Lufilian-Zambezi Belt (modified from Westerhof, 2008). ID: 1- East Gondwana; 2- West Gondwana; 3- South Gondwana; MD = Mwembeshi Dislocation, SSZ = Sanangoè Shear Zone, NMS = Namama Mega

shear, LTB = Lúrio Thrust Belt.

## 2.2 Regional Geology

From a geodynamic point of view, the crystalline basement of Mozambique is composed of three major lithospheric plates or terranes that have collided and amalgamated during the Pan-African Orogenic Cycle (Mäkitie et al., 2008). Before to amalgamation, each terrane was characterized by an individual and specific geodynamic development (Mäkitie et al., 2008). These terranes are called East Gondwana, West Gondwana and South Gondwana (Figure. 4) (e.g. Shackleton, 1994, Grantham et al., 2003, Rogers et al. 1995, Mäkitie et al., 2008). The crystalline basement of the northern part of Tete Province belongs to West Gondwana, mainly to a smaller structural element called the Tete Chipata Belt (Figure. 4), which formed during the Grenvillian orogenic cycle (~1.1–1.0 Ga) (Westerhof 2006, Westerhof et al., 2008a). The Irumide Belt is bounded by the W-E trending Sanângoè Shear Zone (SSZ), which approximately follows Cahora Bassa Lake in the south, by a thrust front or pseudo-suture between the East and West Gondwana terranes in the east, and by the Mwembeshi Dislocation in the northwest, in Zambia (Mäkitie et al., 2008). The basement geology of the northern Tete Province is very complex for being located close to a triple junction between the Irumide Belt, the Zambezi segment of the Zambezi-Lufilian-Damara Belt and the Mozambique Belt, (Westerhof et al., 2008a, Mäkitie et al., 2008).

The crystalline rock of the Tete-Chipata Belt of northern Tete province is composed of metamorphosed and plutonic rocks supracrustal rock sequences that have been grouped into Supergroups and Groups (Figure. 5) (Mäkitie et al., 2008).

These litho-stratigraphic units show different metamorphic grades, structural development, geodynamic setting and ages (GTK Consortium 2006d).

A small portion of the crystalline rocks of basement in northern Tete Province is composed of juvenile rocks emplaced during the Pan-African orogenic cycle (Westerhof et al., 2008).

Supracrustal rocks of the undated Mualadzi Group, are exposed in the north of the Chidzolomondo granulites, and comprise granulite-grade mafic and ultramafic metavolcanics (komatiites?), discontinuous banded ironstone horizon, minor quartzite and retrograde micabiotite-schist. In the past, the Mualadzi metavolcanics rocks have been correlated with the Fíngoè volcanics rock (Westerhof et al., 2008).

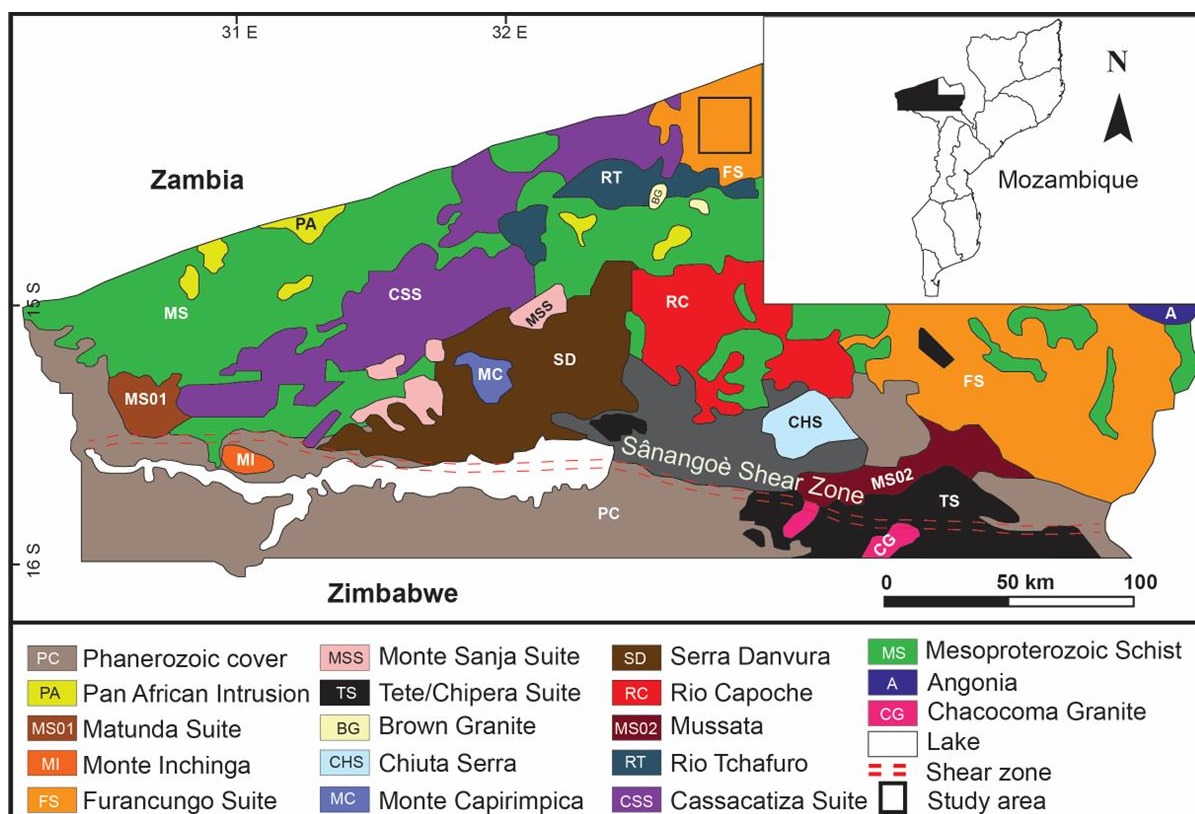


**Figure 5:** Distribution of Mesoproterozoic granitoids of the Tete Chipata Belt, grouped into several granitoid clans and a bi-modal suite emplaced during the Grenvillian orogeny (GTK Consortium, 2006; Mänttari, 2008) and Early Pan-African intrusive rocks (Matunda Suite) in Tete Province (modified after Sterk et al., 2018). Key: A = Angonia; BG = Brown granite; CG = Chacocoma Granite; CHS = Chiuta Serra; CSS = Cassacatiza Suite; FS = Furancungo Suite; MC = Monte Capirimpica; MI = Monte Inchinga; MS = Mesoproterozoic Schist; MS01 = Matunda Suite; MSS = Monte Sanja Suite; PA = Pan African Intrusion; RC = Rio Capoche; RT = Rio Tchafuro; SD = Serra Danvura; TS = Tete Suite.

### 2.3 Local Geology

The general geology of the study area is characterized by the Proterozoic Mualadzi Group (Figure. 6), composed of ultramafic metavolcanic rock, quartzite, mica-biotite-schist, the Macanda mafic metavolcanic, conglomerate rocks and the Furancungo Suite (1041±4 Ma, U-Pb zircon) (GTK consortium, 2006). The host rocks of the Mugomo deposit are metavolcanic rocks, biotite-schist and quartzites cross-cut by quartz and epidote veins and veinlets.

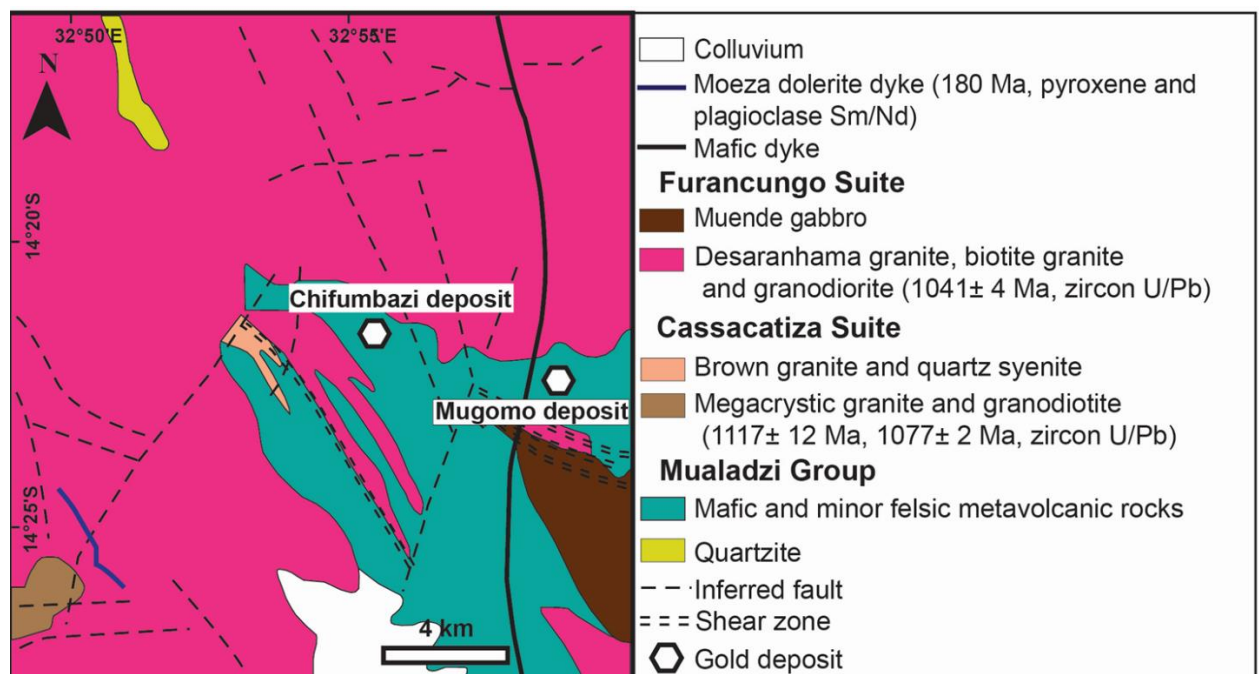


**Figure 6:** Local geology surrounding the Chifumbazi and Mugomo deposits (modified from GTK consortium, 2006).

### 3. Geology of the Deposits

#### Mugomo Deposit

Based on the mapping conducted by GTK, the study area is underlain by felsic metavolcanic rocks. These metavolcanic rocks are cut by a network of quartz veins and mylonite zones, which host most of the gold mineralization of the area (GTK consortium, 2006). However, in this particular deposit, the host rocks are metavolcanic rock, biotite-schist and quartzite. The metavolcanics, quartzites and the biotite-schist occur as a massive fine-grained rock, crosscut by epidote and quartz veins and veinlets, and epidote quartz chlorite veinlets (Figure. 7a-d).



**Figure 7:** Photographs of the host rocks at the Mugomo deposit showing a) quartzite; b) biotite-schist; c) metavolcanic rock crosscut by quartz-epidote-chlorite veins.

### **Chifumbazi deposit**

Based on mapping conducted by GTK in 2006, the rocks in the area are mainly biotite granite and quartz-mica-schist belonging to the  $1041\pm 4$  Ma Desaranhama Suite (Westerhof et al., 2008). Moreover, this deposit is located along the same N-S trending major fracture zones where two types of rocks (GTK consortium, 2006), quartz-mica-schist (meta-granodiorite) and gneiss, occur as a country rock (Figure. 8a-c) (Cossa et al, 2023). The quartz-mica-schist is intermediate to felsic with medium to coarse grains crosscut by quartz vein (Figure. 8c). The host rock is crosscut by three generations of quartz and chlorite veins (Cossa et al, 2023).



**Figure 8:** Photos of the host rocks and country rocks at the Chifumbazi deposit: gneiss in discordant contact with meta-granodiorite (quartz-mica-schist).

### **Formation of host rocks at the Mugomo and Chifumbazi deposits**

Host rocks of the Mugomo deposit are quartzite, metavolcanic rock and biotite-biotite-schist. Quartzite is composed of quartz, epidote, chlorite and amphibole. The metavolcanic rock is composed of albite, biotite and epidote, and the biotite-schist is composed of biotite and quartz. The mineral assemblages indicate that these rocks are metamorphic which resulted from the low-grade greenschist facies metamorphism of their protolith according to their mineralogical composition.

The metavolcanic rock, biotite-schist and quartzite are crosscut by epidote quartz, epidote chlorite and quartz veins that are non or less mineralized due to the dissemination of sulfides in the host rock. The low-grade metamorphism is related to green biotite-schist facies characterized by hydrous minerals such as muscovite, biotite and chlorite.

Chifumbazi deposit is 5 km away from the Mugomo deposit and is characterized by metamorphosed igneous rocks (quartz-mica-schist) and gneiss.



### **3. METHODOS**

#### **3.1 Sampling**

The field work was carried out in the Chifumbazi and Mugomo deposits, Chifunde district at northwest part of Tete province. The collected samples consist of metamorphic rocks, and veins samples. This study was conducted in four stages including the field work, laboratory analyses, data processing and interpretation. Fieldwork for this study includes sampling of representative rock types, altered rocks and gold bearing veins.

#### **Laboratory analyses**

Laboratory work includes optical petrography, X-ray diffraction (XRD) and whole-rock geochemistry by X-ray fluorescence (XRF), inductively coupled plasma mass spectrometry (ICP-MS), electron probe microanalyzer (EPMA), fluid inclusion and sulfur isotope analyses.

This chapter will cover various approaches that were taken to collect and interpret the geological and geochemistry data within the Chifumbazi and Mugomo deposits. All sample preparations and analysis were conducted at Department of Earth Resource Science Akita University and Actlabs in Canada.

The interpretation of the data includes desktop studies, plotting of data using Geographic Information System (GIS), Adobe Illustrator, IoGas\_64, and Excel. All the analytical and interpretation methods are discussed further in detail below.

##### **3.1.1 Desktop Studies**

The desktop studies include the literature reviews of the geology of Tete province and reviewing of unpublished Mozambique exploration annual reports by Direcção Nacional de Geologia (DNG) from (1978) and various reports and articles related to the Irumide Belt, various orogenic systems and gold mineralization in the igneous and metamorphic rocks.

### **3.2 Fieldwork**

Desktop studies were followed by the outcrop observation and sampling in the Chifumbazi and Mugomo deposits. The sampling and selection were focused on the type of rocks, mineralization and alteration identified during the initial desktop studies. Structural data obtained include strike and dip readings and crosscutting relationships. The GPS receiver was used to record the location of the sampling points. Some sample locations were recorded using the pace factor method. A total of 40 samples were collected from the Chifumbazi deposit and 40 samples from the Mugomo deposit. (Appendix 1)

### **3.3 Analytical Methods**

Petrography (Microscopy observation)

Microscope examination of doubly polished sections, polished sections, and thin sections was carried out using a Nikon ECLIPSE LV100N POL polarizing microscope equipped with a CCD camera CS5270B for taking photomicrographs. The scale for each objective for the CCD camera CS5270B was already calibrated using a Nikon micrometer.

Samples prepared for petrography were observed in plane-polarised light (PPL) and between crossed-polarized light (XPL), at different magnifications and selected rotation points. Under PPL and XPL, the optical properties described mineral identification, alteration textures, assemblages, birefringence and interference color, mineral size, extinction angle, twinning, zoning and dispersion. The petrographic study of opaque minerals was under reflected light.

Doubly-polished sections were observed under the polarizing microscope to characterize the fluid inclusions in the veins.

#### **Polished thin sections**

The selected samples were cut into slabs with dimensions of 3.5 cm x 2.5 cm using a diamond saw deployed at the rock sample preparation room of Akita University. For friable and soft samples, the desired side for analysis was first cemented with Petropoxy

154 epoxy resin and left for a day in the hot plate at 90°C. The rock slabs were then polished on both sides: the side selected for analysis was sequentially polished with grinding powders #150, #320, #800 and #1000, while the other side was polished with 150 grinding powder only. The slabs were cleaned using the ultrasonic bath for about 5 minutes between each grinding step. The slabs were then attached to the glass slides by bonding the side polished until # 1000 grinding powder by either petropoxy 154 or E-bound and were left to dry for about 24 hours.

For samples bound using Petropoxy, drying was done by leaving the samples on the hotplate at 90 °C, while for samples attached using E-bond, samples were dried at room temperature, with being clipped by 2 metal clips to ensure even bonding. Once dried, the samples were then cut using a secondary cutter at a thickness of about 1 mm. Separated sections were trimmed down to about 150 to 200 µm using a Prepalap machine, and were further polished using #800 powder, while periodically checking the thickness with the optical microscope through the quartz grains interference color. Once the quartz grains show 1<sup>st</sup> order yellow to 1<sup>st</sup> order white interference color, the thin section was cleaned using the ultrasonic bath for about 5 minutes.

Further polishing using #1000, #2000, #3000 polishing powders was carried out until the right thickness of 30 µm is achieved and confirmed by 1st order grey interference color of quartz grains, with an ultrasonic bath cleaning for about 10 minutes in between each polishing step. The final step of polishing was done with 3 µm and 1 µm diamond polishing at 15- 20 minutes duration each. The thin sections were cleaned by wiping with ethanol and then finally sending it to a 5-minute ultrasonic bath.

### **Polished sections**

The sample preparation and selection were based on cutting mineralized samples, selected portions of the rock samples were also cut with dimensions that can fit in the circular holder (diameters less than 2.5cm). Vaseline gel was applied in the inner portions of the circular plastic holders and base caps to remove easily the polish section after resin

consolidation. Low viscosity resin with a mixture of 1-2 mL of M curing agent for every 100 mL of low viscosity resin was prepared. Samples were placed in the holder, followed by bonding resin, sample ID (written on a piece of paper). The sample was placed inside the vacuum glass machine for about 2- 5 minutes to suck all the air mixed with epoxy and left to dry for one day. Once completely solidified, samples were polished sequentially with grinding powders, #150, #320, #800, #1000, #2000 and #3000  $\mu\text{m}$  with ultrasonic bath cleaning in between grinding steps. The final steps were done using 3 and 1  $\mu\text{m}$  diamond polishing powder at 20 minutes duration each with cleaning by ethanol, and a 5 minutes ultrasonic bath.

### **Doubly- polished section thick sections**

Selected vein samples were cut into slabs with dimensions of about 1 cm x 1 cm using a small diamond cutter. The vein slabs were polished, the side selected for analysis was sequentially ground and polished with grinding powders #150, #320, #800, #1000, #2000, #3000, 3  $\mu\text{m}$  and 1  $\mu\text{m}$  using diamond polishing during 20 minutes duration, each cleaning by ultrasonic bath and wiping with ethanol.

The sample impregnation to the glass side was made using superglue and let it sit overnight to seep in. After that the sample is cutting using secondary cutting (slow speed diamond saw). The samples were polished again with #800, #1000, #2000 and #3000 powders grinding with ultrasonic bath cleaning in between steps. Final polishing was carried out with 3  $\mu\text{m}$  and 1  $\mu\text{m}$  diamond polisher pastes using diamond polishing for during 15minutes, each cleaning by ultrasonic bath and ethanol. The double polished wafers were removed from the glass side by submerging in acetone for 4 to 6 hours and were cleaned by ethanol.

### **Carbon coating**

Selected polished thin section, polished section samples, and double-polished wafers were carbon-coated to approximately 20 to 25 nm thick, for polished thin and polished sections. Carbon coating was carried out using a JEOL JEC- 560 vacuum evaporated

carbon coating machine. At manual conditions, the voltage was set to 4.8 V at timer 10s, while at cycle conditions, the voltage was set at 1.7V initially for 30 s and 3 s at the succeeding steps. Coating operation was performed at pressures 1.4 to 1.7 Pa at vacuum conditions. Samples were kept in an improvised desiccator containing silicone gel beads for safekeeping in an environment with minimized humidity.

### **Preparation of powder samples, pellets**

About 2 to 15 g of the selected portion of the rock slabs, veins and ore minerals (pyrite and chalcopyrite) samples were crushed and powdered for X-ray diffraction (XRD), X-ray fluorescence (XRF), inductively coupled plasma-mass spectrometry (ICP-MS) and sulfur isotope analyses.

The samples were lightly crushed by using an iron mortar and pestle to obtain the coarse-grained sand-sized fragments.

Powdering to clay-sized particles was done by using an agate ball mill. The agate ball mill was cleaned before, in between samples and after each sample by quartz sand to minimize the risk of cross-sample contamination. The milled samples were packed in a large-sized paraffin paper enclosed in a plastic bag and was stored in the desiccator.

### **X-ray diffraction (XRD)**

The samples are lightly crushed using an iron mortar and pestle to coarse-grained sand-sized fragments, therefore, before, between and after crush each sample is necessary to clean the iron mortar and agate ball mill to minimize the contamination. The powdering to clay-sized particles was done using an agate ball mill crusher, and the sample was packed in a large-sized paraffin paper enclosed in a plastic bag.

XRD measurement requires in advance putting the sample powder in the holder and making the surface flat using glass. For friable samples, and samples that have possible occurrence of clay minerals, hydraulic elutriation was applied to orient the samples for better peak analyses in XRD. The samples were lightly crushed to pebble to coarse-sand sized fragments and were placed a 500 mL beaker. They were then submerged in distilled water, and rigorously mixed. The clay minerals would be separated from the non-clay

minerals as they would take a longer time to settle (approximately 3 to 4 hours dependent on the amount of sample powder) with respect to the latter. Using a pipette, a layer of clay minerals suspended in distilled water was extracted, and transferred to a test tube. Using a centrifuge machine for about 10 minutes at 350 rpm, the clay minerals were separated from the liquid. The clay minerals settled at the base of the test tube were collected by decantation and placed into a glass holder for XRD analysis.

### **Inductively couple plasma mass spectrometry (ICP-MS)**

In this method, the initial weight of the sample was measured, and then poured in a plane at a constant rate and subdivided into four equal parts. The selected part was taken and measured using an electric balance. For an 8 g sample, one quarter is about 2 g, the process was repeated until a 0.50g of powder was achieved. Collected 100 mg of powder from selected samples were analysed by aqua regia and nitric acid.

Major and trace elements were analyzed on fusion ICP-OES and ICP-MS at Actlabs in Canada.

### **Sulfur isotope analysis**

The process of barium sulfatr preparation needs 20 mg of pyrite and chalcopyrite samples as pure as possible by the mineral separation under the binocular microscope, to collect the specific mineral of interest.

Pyrite and chalcopyrite were selected for sulfur isotope analysis because of its abundance and coarse sand size crystals. The ore minerals were extracted from representative samples by:

1. crushing the samples to fine sand size powder using the iron agate mortar
2. panned the ore minerals using the panning dish.
3. separation of pyrite and chalcopyrite from silicates using a Nikon SMZ 1500 binocular.

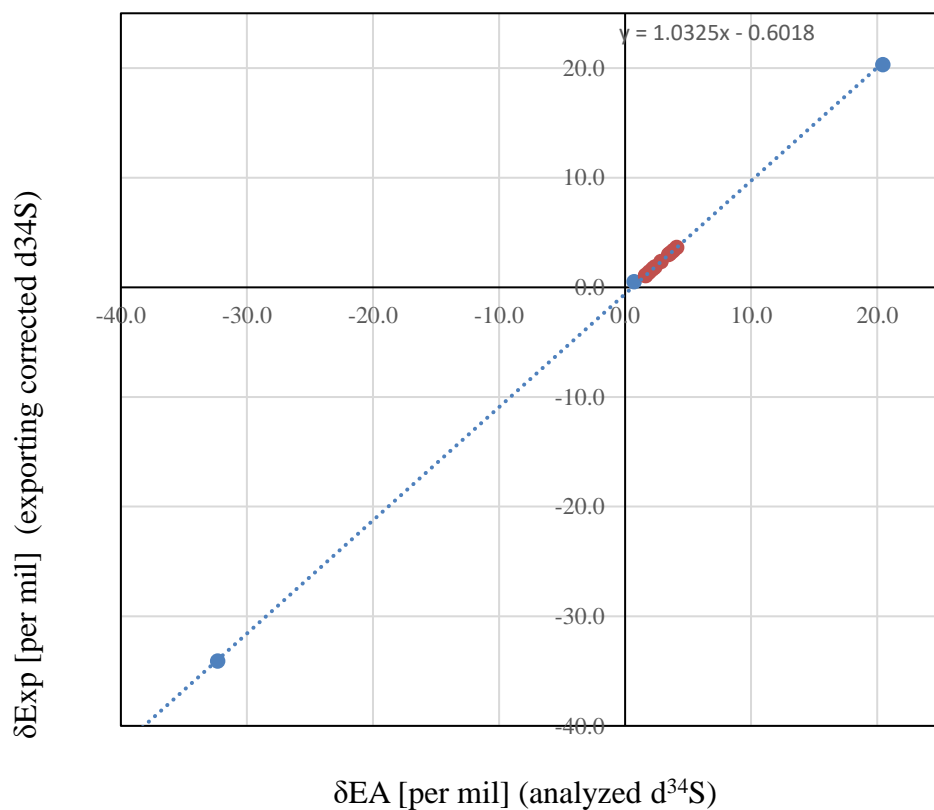
The amounts of pyrite and chalcopyrite was between 20 mg and 40 mg. The 20 mg of sulfide is decomposed in the 100 ml beaker glass with adding 40 ml nitric acid ( $\text{HNO}_3$ ) and about 4 ml bromine ( $\text{Br}_2$ ), putting the watch glass on the top to avoid the evaporation of bromine under 95 °C to 99 °C (not in boiling condition). Usually, the sulfide is digested

in 1 hour, if the sulfide sample is not dissolved yet, more bromine about (1 to 4 ml) was added for more reaction during the 15 to 30 minutes or until all samples were dissolved. After one day of evaporation, the sample should be dissolved with 10 ml 6N HCl using pipe and add 90 ml of distilled water, to make a total of 100 ml sample solution. The solution was checked for any residue. The solution was filtrated whenever a residue was found. The residue is commonly silicate minerals or another non-separable mineral. The solution was filtered using filter paper, and the captured filtered solution was then used for cation ion exchange. After the preparation of the cation ion exchange resin column, the solution was poured into the column slowly and captured with a 300 ml glass beaker. After the ion exchange process, 10 ml of 10% BaCl was added to the captured solution to form the BaSO<sub>4</sub> precipitate and heated to 99 °C for one day while having the watch glass on. The column was later cleaned with HCl six normal (6N) solution to remove all captured cations, and rinsed with distilled water until a neutral pH was reached. The next sample was processed followed by the cleaning process as described earlier. Final filtration procedure involved pouring sample solutions into 50 ml syringes containing 0.25 micro meter membrane filter paper, and carefully filtered to obtain the BaSO<sub>4</sub> crystals were then weight, and between 0.2 to 0.4 mg of samples were placed in small tin capsules, followed by vanadium pentoxide (V<sub>2</sub>O<sub>5</sub>) of 5 to 6 times the samples weight. The tin capsules folded carefully into small cube sizes and safely stored away for analysis. Preparation of standards included tin capsules, SO<sub>5</sub>, 3x SO<sub>6</sub>, and 2 x NBS-127 samples, whereby all were prepared similarly to the BaSO<sub>4</sub> sample preparation using tin foil and V<sub>2</sub>O<sub>5</sub>.

Sulfur isotope samples and standards were analysed using the Thermo Delta-V Advantage, Isotope Ratio Mass Spectrometry machine. Calibrated results from standard samples are provided in table 1 and Figure 9. A total of 22 samples were analysed.

**Table 1:** Calibrated  $\delta^{34}\text{S}$  results from sulfur isotope standards

Measurement sequence	$\text{d}^{34}\text{S}$ to gas (per mil)		
	SO-6	SO-5	NBS-127
1st	-32.332	0.793	20.421
2nd	-32.354	0.731	20.456
3rd	-32.255	0.644	20.499
Average	-32.314	0.723	20.459
True value	-34.10	0.50	20.30
SD	0.20	0.20	0.40

**Figure 9:** Calibration curve for sulfur isotope standards. Referenced to table 2 above.



### **3.3.6 Scanning Electron Microscope Analysis (JEOL JSM-IT300)**

Point identification analyses were carried out on carbon coated polished sections using the SEM-EDS to confirm and identify unknown minerals and determine their elemental composition. Coated samples were carefully mounted on holder and analysed with an EDS detector. All analyses were done in high vacuum condition, at working distance of 10 mm, at acceleration voltage of 15kV, beam current of 2.2 nA, and spotsize of about 60 nm.

### **Fluid inclusion microthermometry**

Quartz samples selected for fluid inclusion analysis were prepared as doubly polished wafers with a thickness of 150  $\mu\text{m}$ , and microthermometry experiments were carried out using a Linkam 10035 freezing and heating stage attached to a Nikon ECLIPSE LV100N POL microscope.

### **Electron Microscope analyses – EPMA**

The chemical composition of ore mineral (pyrite) and mapping were conducted using JEOL JXA-8230 and 8800R electron probe microanalyzers (EPMA) at Akita University. The analyses were conducted to measure contents of Au, Ag, Fe, S, Cd, Zn, Co, Cu, Pb, Te, As, Bi, and Ni in the pyrite. The results are reported in (Appendix 4).

The analyses were performed using an accelerating voltage of 20 kV, a current of 20 nA and a probe diameter of 10  $\mu\text{m}$ . Peak and background counting times were 20 /10 s for Fe and S, 50/ 25 s for Cd, Zn, Co, Cu, Pb, Te, As, Bi, and Ni, 300/ 150 s for Au and 100/50 s for Ag. respectively.

### **Laser Raman spectroscopy**

The identification of  $\text{CO}_2$  and  $\text{H}_2\text{O}$  for the vapor phase of fluid inclusion samples was carried out via a Renishaw Laser Raman Spectrometer at Akita University. The calibration processes, a silica standard was conducted at the beginning of the measurement. The laser power was 10 % on the measurement, while on the vapor-rich inclusions the laser output was set to 50% to get optimum results and to avoid the decrepitation of the fluid inclusions.

### Microthermometry

Microthermometry was conducted on both the polyphase brine and vapor rich inclusions using a Linkam 10035 heating stage.

The Linkam 10035 heating stage was calibrated using standard chemicals to their known final melting temperature at a heating rate of 0.3°C per minute. Heating rates of 1°C/min were employed for measurements below 30° C and 5° C/ min up to 500 °C. Consequently, the accuracy of the measurements was approximately  $\pm 0.2^\circ\text{C}$  during the freezing cycle and  $\pm 0.2^\circ\text{C}$  during the heating measurements (Table 2, Figure. 10).

**Table 2:** Summary of final melting temperature ( $^\circ\text{C}$ ) and known final melting temperature ( $^\circ\text{C}$ ) of the selected chemicals for the calibration of the Linkam 10035 freezing and heating stage.

Chemicals	Composition	info	True temp (deg C)	Start melting (deg C)	Final melting temp (deg C)
CO <sub>2</sub> liquid	CO <sub>2</sub>		-56.6	-60.0	-59.6
n-Dodecane			-9.6	-11.5	-10.6
n-Tridecane			-5.5	-12.8	-6.7
pure water			0	-2.8	-0.1
n-Tetradecane			5.5	3.5	4.8
Benzanilide	C <sub>13</sub> H <sub>11</sub> NO		163	160.8	165.2
Sodium Nitrate	NaNO <sub>3</sub>		308	304.5	323.3
Potassium dichromate	K <sub>2</sub> Cr <sub>2</sub> O <sub>7</sub>	toxic	398	343.3	413.3
Cupric chloride	CuCl <sub>2</sub>	toxic	498	-	-

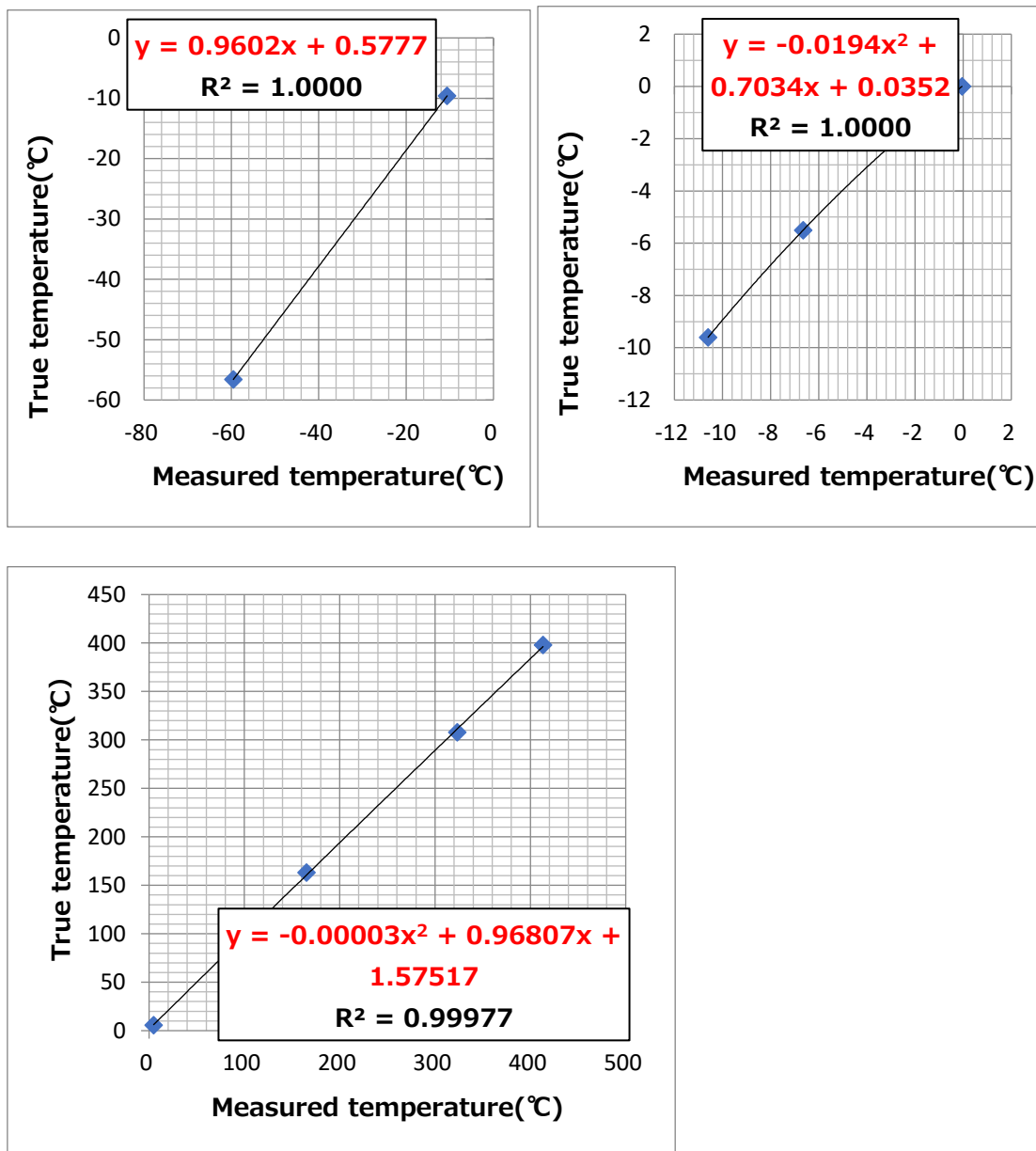


**Figure 10:** Fluid inclusion calibration curves applied for the microthermometry data correction. 1. CO<sub>2</sub> calibration curve; 2. Calibration curve of melting ice temperature (T<sub>m</sub>) curve; 3. Calibration curve of homogenization temperature (T<sub>h</sub>).

## **4.RESULTS**

### **4.1 MUGOMO DEPOSIT**

## **4.1.1 CHARACTERISTICS OF THE HOST ROCKS**

### **4.1.1.1 Petrography**

The host rocks in the Mugomo deposit are mainly metavolcanic rock, quartzite and biotite-schist.

The metavolcanic rock is fine to coarse-grained. The quartzite shows massive texture and biotite-schist is foliated.

Under the microscope the rocks show the following characteristics.

- 1.** Quartzite shows granoblastic texture composed of quartz and plagioclase, (Figure.11 a-b), crosscut by chlorite and epidote veinlet (Figure.11 c).
- 2.** Metavolcanic rock shows a granoblastic texture composed of plagioclase, quartz, biotite, muscovite, and epidote, sericite and calcite as alterations minerals. (Figure. 11d-g). sericite is replacing plagioclase (Figure. 11b) and filling fractures within plagioclase and epidote (Figure.11e).
- 3.** Biotite-schist shows lepidoblastic texture composed of biotite and minor quartz. Biotite occurs as elongated crystals and quartz is present in small amount (Figure. 11h).

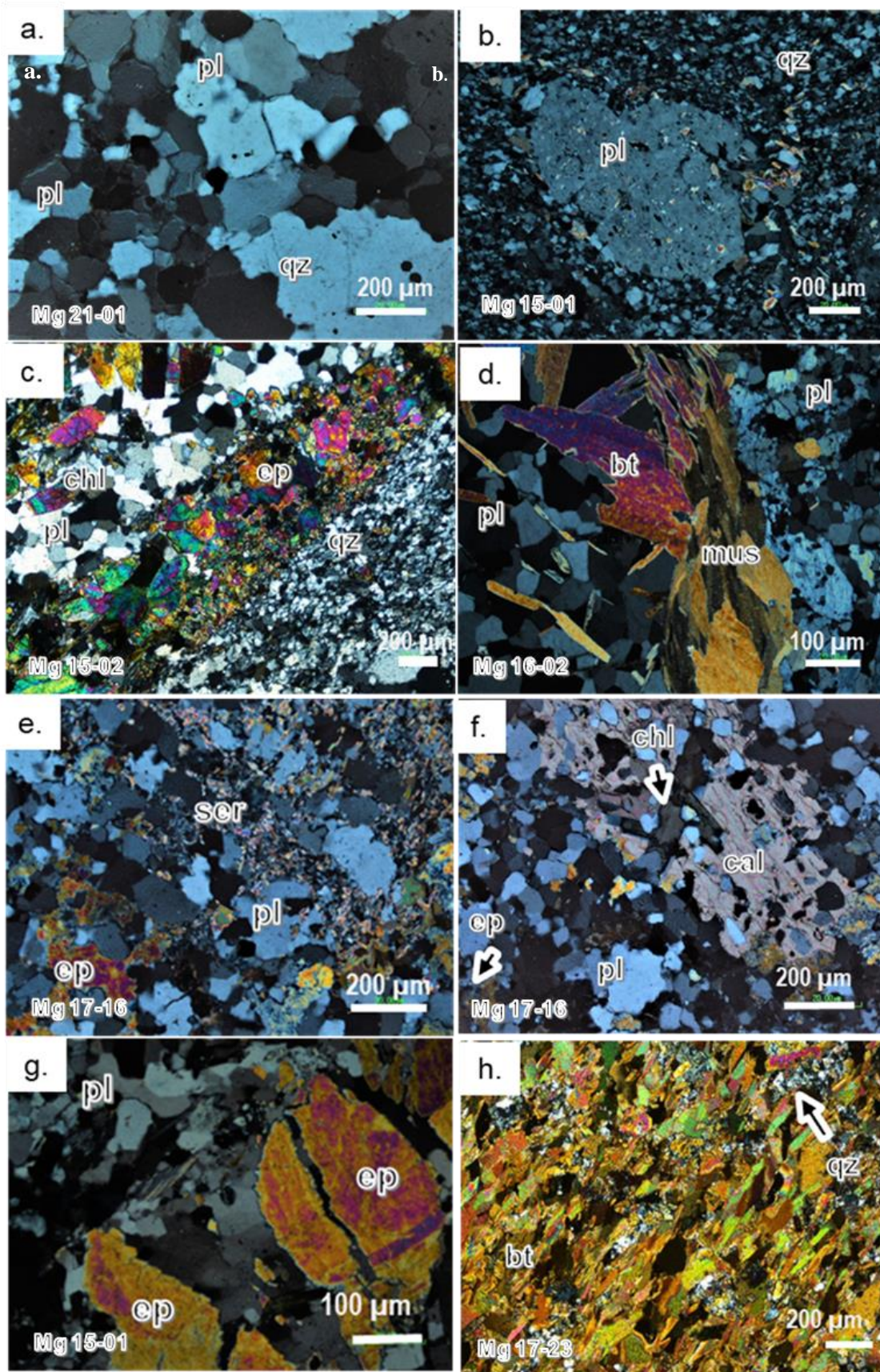


**Figure 11:** Photomicrographs with transmitted light and crossed polars of the host rocks in the Mugomo deposit: (a,b) a quartzite with granoblastic texture composed of quartz and plagioclase; (c) a quartzite composed of plagioclase and quartz with chlorite alteration crosscut by epidote veinlet; (d) a metavolcanic rock with granoblastic texture composed of plagioclase, biotite, and muscovite; (e) a metavolcanic rock composed of plagioclase, epidote, and sericite alteration; (f) a metavolcanic rock composed of plagioclase, epidote, chlorite and calcite alterations; (g) a metavolcanic rock composed of plagioclase, and epidote; (h) a biotite-schist with lepidoblastic texture, composed of biotite and quartz. Abbreviations are pl: plagioclase, qz: quartz, bt: biotite, mus: muscovite, chl: chlorite, ser: sericite.

#### 4.1.2 Hydrothermal alteration

Hydrothermal alteration is weakly developed in the Mugomo deposit and is characterized mainly by epidotization, silicification, chloritization, sericitization and carbonatization of metavolcanic rock and quartzite (Figure. 11c, e,f, g).

The alteration mineralogy of the host rocks has been determined based on the alteration of minerals and the textural relationship between mineralization and lithology of the host rock. Epidotization, silicification and chloritization are the main alteration types (Figure. 11c, e, f, g). Sericite and calcite are in minor amount found in the metavolcanic rocks (Figure. 11e) in the Mugomo deposit.

Sericite-carbonate, and chlorite alteration types (Figure. 11e-f) are found in the metavolcanic rock in the Mugomo deposit. The textural relationship between the two alterations is not clear, therefore the alterations may represent different hydrothermal events.

### 4.1.3 Geochemistry of the host rock

Selected chemical analyses of representative samples studied for major, minor, and trace elements are listed in Tables 4, 5 and 6, and appendix 2. Due to the fact that the rocks in this study have been metamorphosed, fluid-mobile elements such as CaO, Na<sub>2</sub>O, and K<sub>2</sub>O, as well as trace elements such as Rb, Sr, Ba, cannot be used to discuss tectonic environments or fractionation assimilation pathways (Humphris & Thompson, 1978; Brekke et al., 1988; Brouxel & Lapierre, 1988 and Johnson et al., 2007).

Whole-rock data of the Mugomo deposit (Table 4) and the Mualadzi Group (from GTK consortium, 2006) (Table 5) are shown in a series of Harker diagrams and normalized trace-element as well (Figure. 12)

Whole-rock chemical composition of 16 samples from Mugomo deposit was analyzed, and the major elements show a variation in SiO<sub>2</sub> from 56.1 wt.% to 81.7 wt.%, Al<sub>2</sub>O<sub>3</sub> contents range from 9.23 wt.% to 16.3 wt.%. whereas the MgO content is between 0.11 and 7.61 wt.% (Table 4, appendix 2).

The Harker diagrams show continuous trends between the felsic metavolcanic from the Mugomo deposit and mafic metavolcanic rocks from the Mualadzi Group (Table 5 appendix 2). In the Harker diagrams plots both Mugomo deposit and Mualadzi group major and trace elements of the metavolcanic rocks show depletion of Nb.

The immobile element ratios Nb/Y and Zr/Ti suggest that the protolith of metavolcanic rocks is rhyolite or dacite (Figure.13).



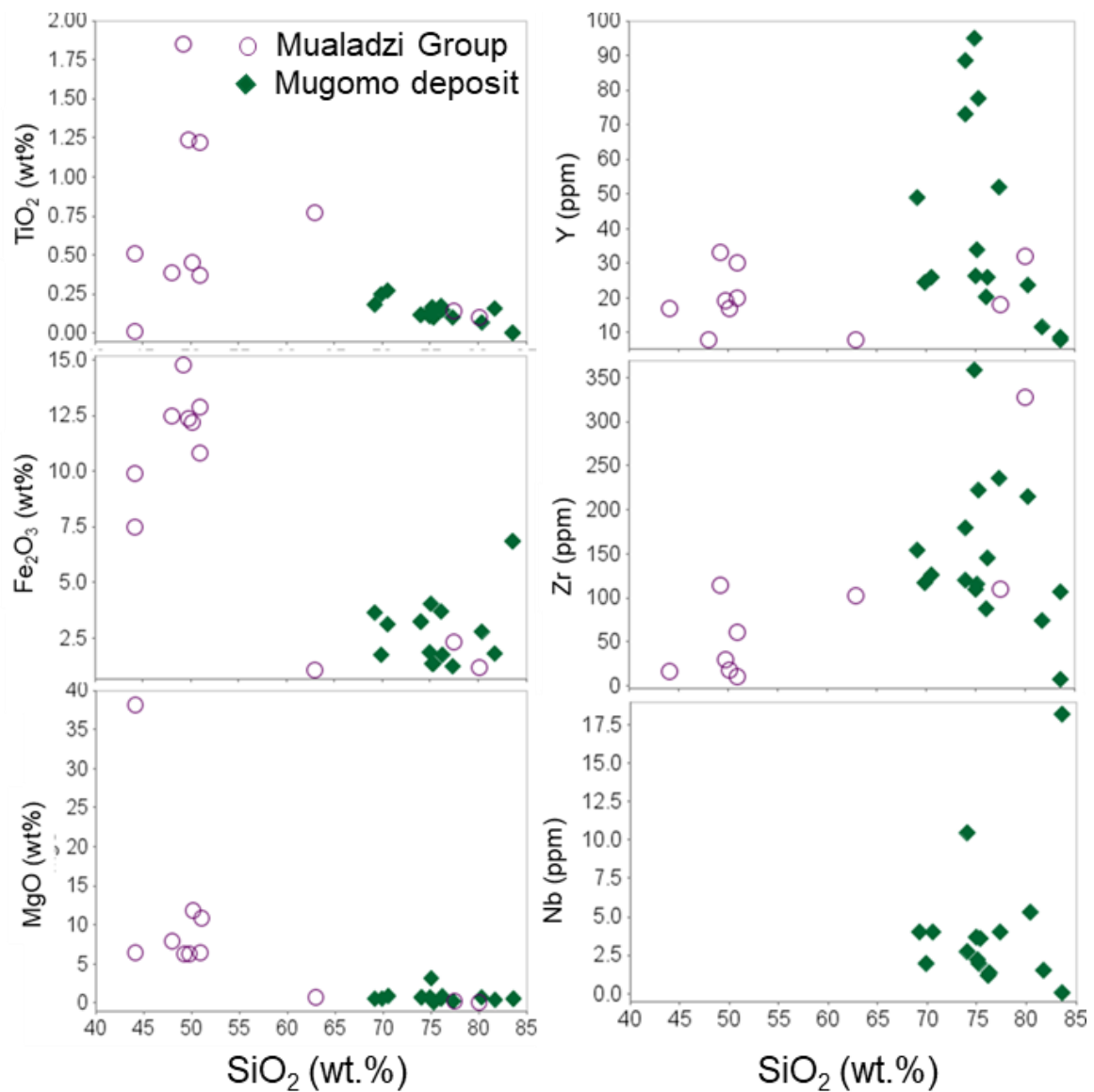


**Figure 12:** Harker diagrams of major elements oxides of host rock from Mugomo deposit and Mualadzi group. *CaO*, *Na<sub>2</sub>O*, *K<sub>2</sub>O*, *Rb*, *Ba*, and *Sr* are not considered, since their concentrations *might* have changed significantly during the Pan-African Orogeny (*e.g* Johnson et al., 2007).

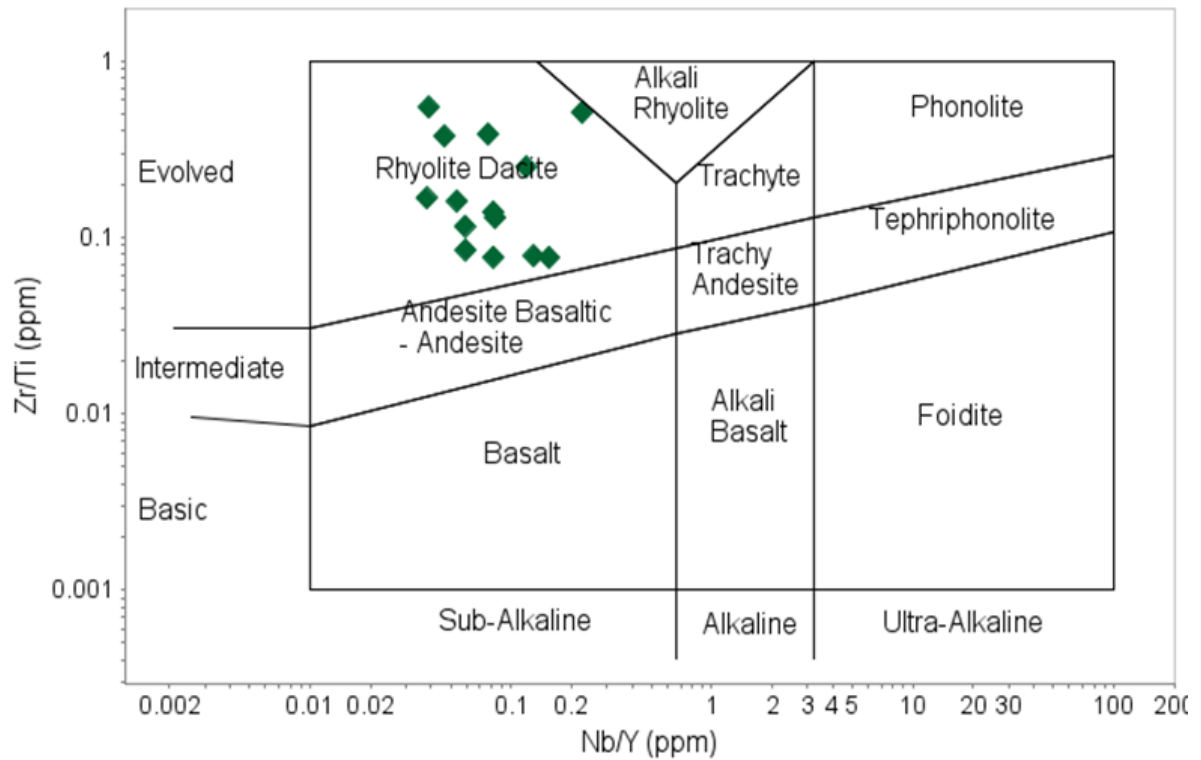


**Figure 13:** Discrimination diagram of the Mugomo deposit host rock based on immobile elements Zr/Ti and Nb/Y (modified from Pearce, 1996).

#### 4.1.4 Rare Earth Element (REE)

Rare earth elements were measured using the ICP-MS in samples of rhyolite dacite from Mugomo deposit (Figure. 14). REE elements were classified into two groups the: LREE (light rare earth elements) and HREE (heavy rare earth elements).

The values were normalized to the chondrite values of Sun and McDonough (1989), showed in Table 6 appendix 2.

The spider diagram of meta-rhyolite-dacite from Mugomo deposit shows a slight enrichment of LREE over HREE ( $La/Yb_N = 0.9 - 1.8$ ) and a negative Eu anomaly (Figure. 14b). The spider diagram of meta-rhyolite-dacite shows moderate enrichment of large-ion lithophile elements Cs, Ba and Th over REE and marked negative anomalies at Nb (compared to La), and Ti compared to mid-REE. Light REE are mildly enriched compared to mid-REE ( $La/Sm_N = 0.9 - 2.4$ ), whereas the mid to heavy REE trends a nearly flat ( $Sm/Yb_N = 0.6 - 2.3$ )

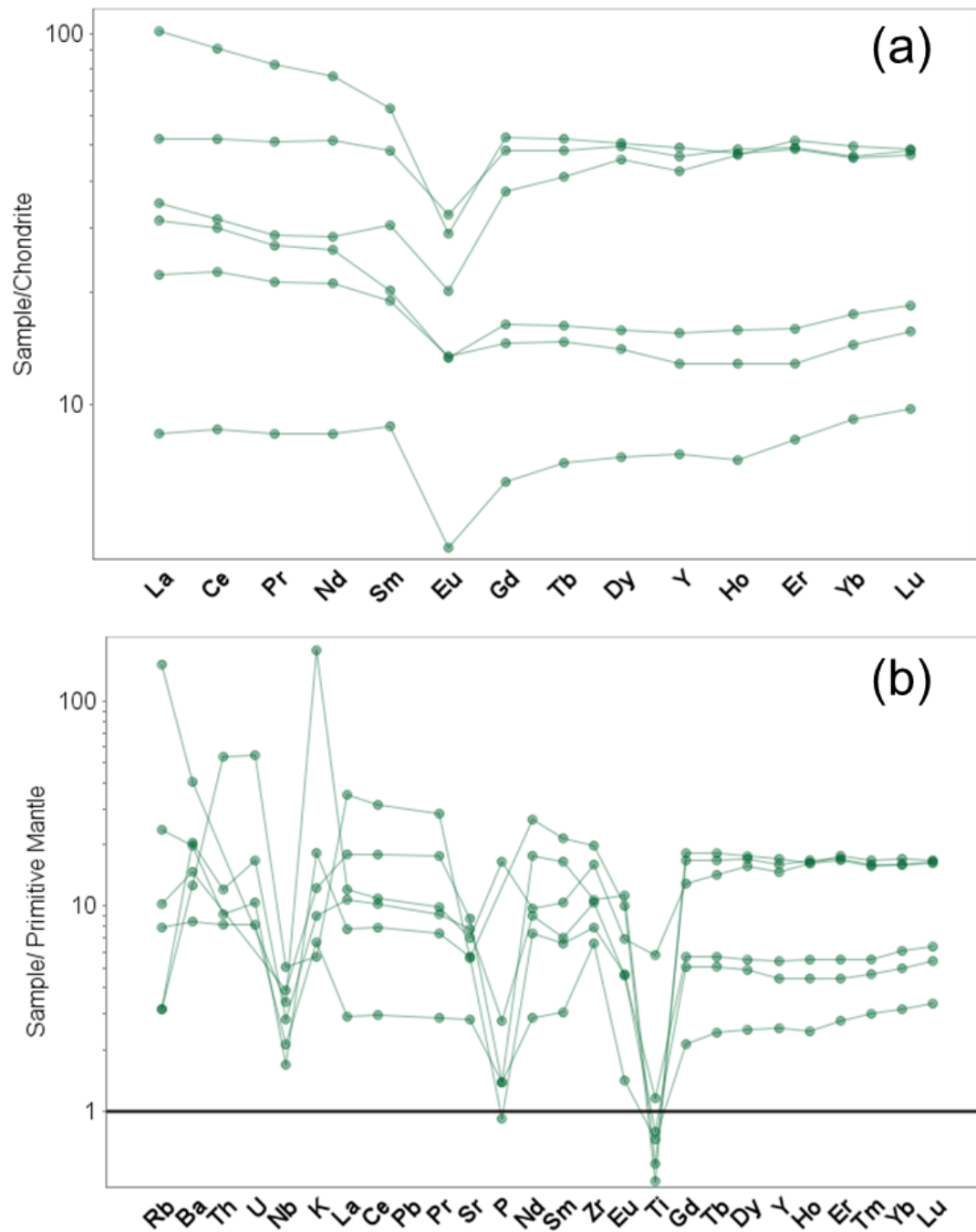


**Figure 14:** Chondrite-normalized REE pattern (a) and primitive mantle-normalized trace elements and (b) of chondrite values from Sun McDonough (1989).

## **4.1.5 ORE MINERALOGY**

### **4.1.5.1 Mode of occurrence of ore minerals**

In the Mugomo deposit, the ore minerals are mostly disseminated in the host rock and to a lesser extent in the quartz veins (Mg 21-02 appendix 1.2)

#### **Mineralized quartz veins**

The quartz veins in this deposit are wide and contain a small amount of ore minerals. The mineralized quartz veins appear crosscut the epidote veins.

#### **Mineralized host rock**

The ore mineral assemblage in the metavolcanic rock, quartzite and biotite-schist host rock at Mugomo deposit includes pyrite, chalcopyrite, and sphalerite, with minor bornite and trace Ag-telluride, Bi-telluride and native gold. Pyrite occurs as euhedral crystal, with grain size varying from 150 to 500  $\mu\text{m}$  (Figure. 15a, b,c,f). Anhedra pyrite also occurs associated with chalcopyrite and covellite (Figure.15b), sometimes with native gold inclusions (Figure 15c). Bornite occurs as subhedral crystal grains associated with an unidentified Fe-Co-S (Figure. 15d). Magnetite occurs as anhedra crystals (Figure. 15e) associated with chalcopyrite and covellite. Ag-telluride and Bi-telluride crystals occur along the boundaries of pyrite (Figure. 15f).

The mineralisation stage of the Mugomo deposit consists mostly of pyrite-sphalerite-chalcopyrite, minor bornite, and trace Ag-telluride and Bi-telluride (Figure. 16), with epidote and chlorite as alteration minerals.

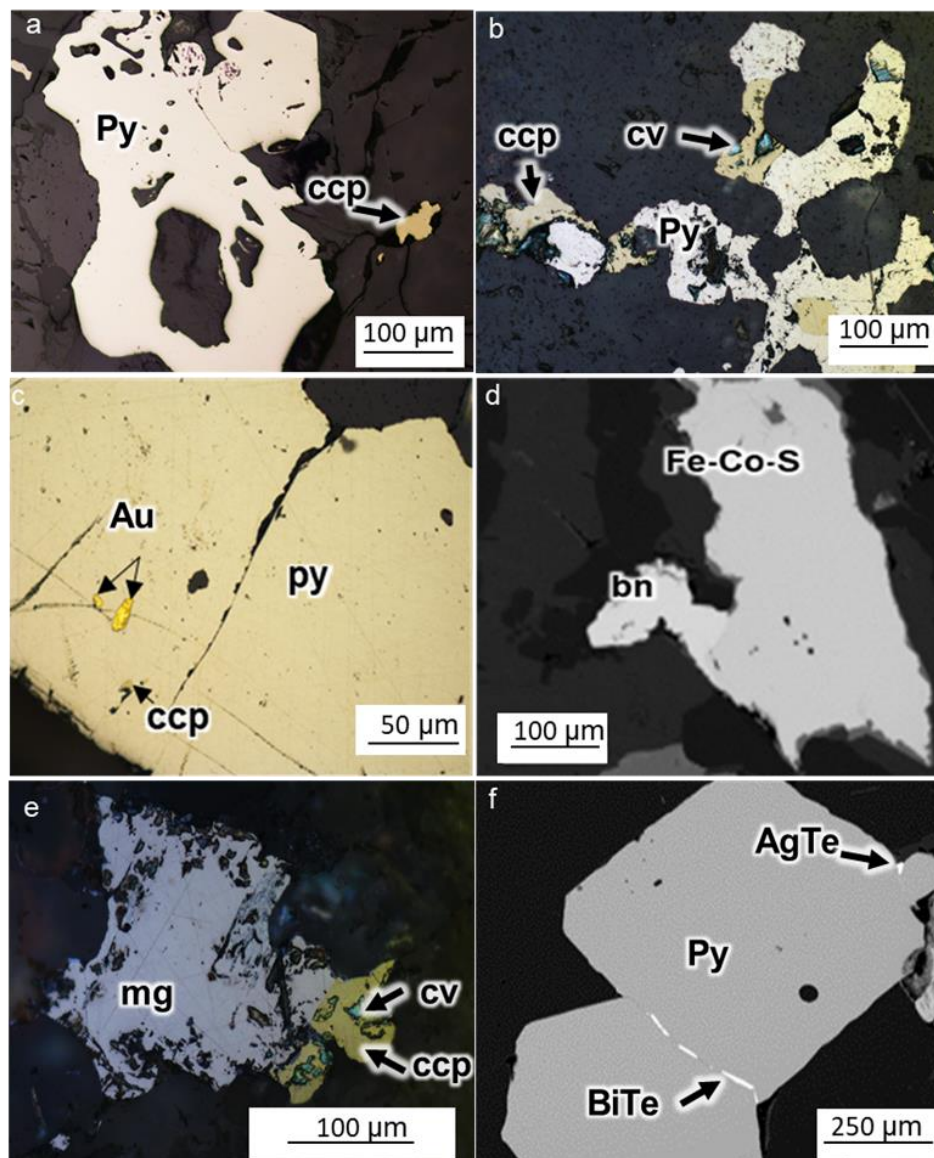


**Figure 15:** Photomicrographs ore minerals of the Mugomo deposit. a) Subhedral pyrite crystal and chalcopyrite; b) subhedral crystals of pyrite intergrown with chalcopyrite with covellite replacement; c) native gold inclusions in pyrite crystal with chalcopyrite; d) backscattered electron image of bornite intergrown with Fe-Co-mineral; e) magnetite intergrown with chalcopyrite and covellite replacement; f) backscattered electron image showing euhedral crystals of pyrite with Bi-telluride and Ag-telluride filling microfractures in pyrite; Abbreviations: py – pyrite; sp – sphalerite; ccp – chalcopyrite; mg –

magnetite; gn – galena; cv – covellite; BiTe – bismuth telluride; AgTe – silver telluride, Au - gold.

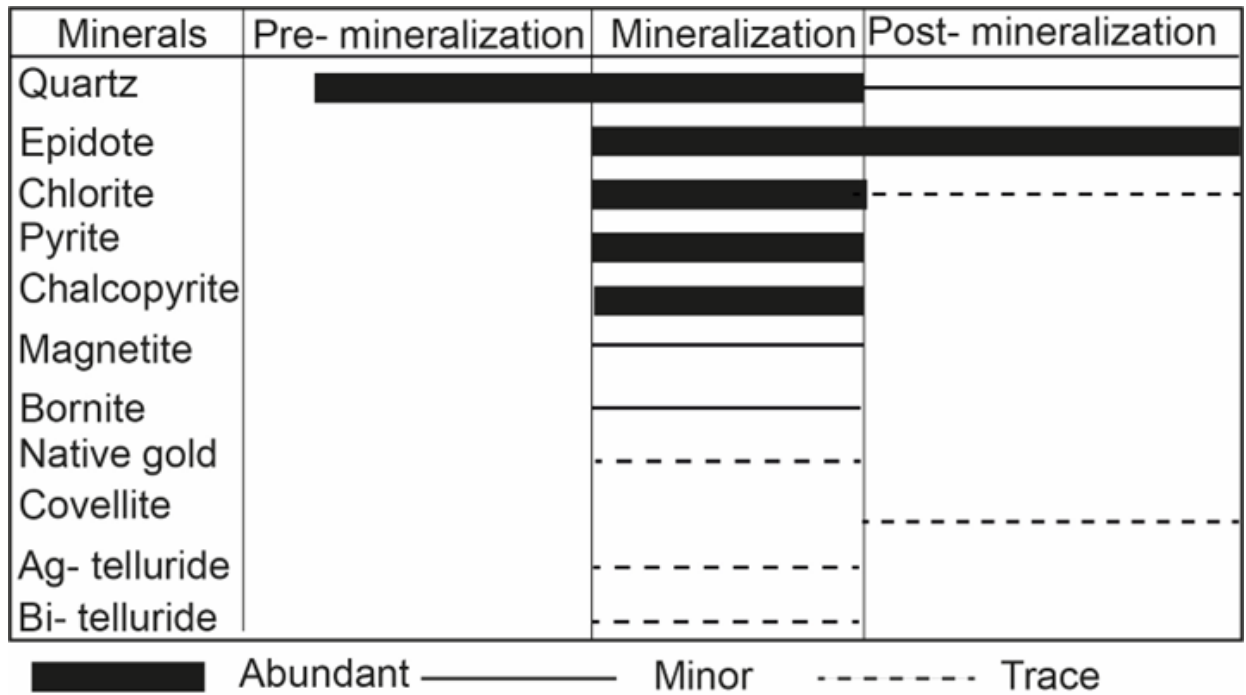


**Figure 16:** A simplified paragenetic sequence of mineralization and alteration in the Mugomo deposit

#### 4.1.6 Trace elements characteristics

For trace element analyses conducted in the Mugomo deposit, epidote quartz veins, and meta-rhyolite-dacite were selected. The rhyolite-dacite has maximum content of Au (~2 ppm), Ag (15 ppm), Cu (313 ppm), Ni (41 ppm), Zn (3002 ppm), Mn (1295 ppm) and Pb (87 ppm). The epidote-quartz veins yielded concentrations of Cu (1023 ppm), Mn (1032 ppm), and Co (255,9 ppm) (Figure. 17, Table 7, appendix 2).

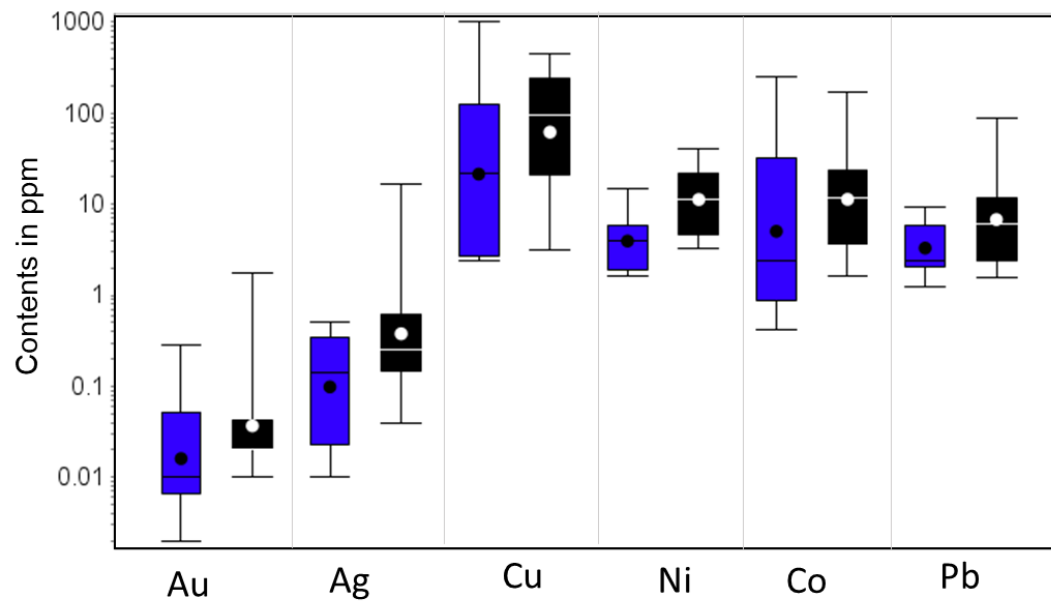


**Figure 17:** Gold, Ag, Cu, Co, Ni, and Pb contents of metavolcanic rock and epidote quartz veins from the Mugomo deposit, determined by the ICP-MS analytical method.



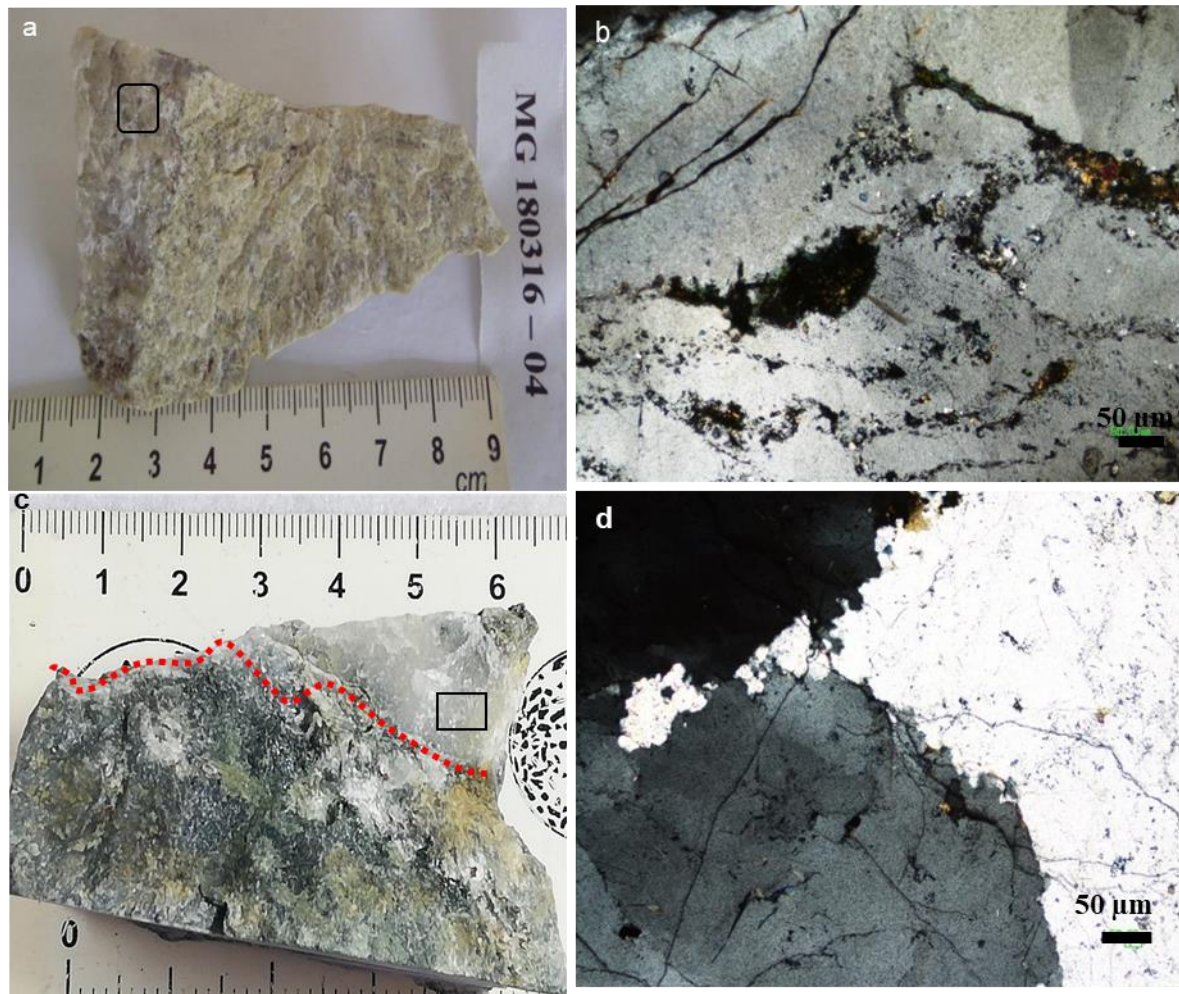


**Figure 18:** Hand specimen photos and photomicrographs of Mugomo deposit showing a) mineralized quartz and epidote vein; b) euhedral quartz cross-cutting by chlorite and clay minerals; c) quartz vein cross-cutting metavolcanic rock; d) mozaic quartz texture.

#### 4.1.7 Petrography of fluid inclusion

Fluid inclusion study was conducted on barren quartz. Seven doubly polished thin sections were prepared, however, the size of inclusions in four samples are very small with a size  $< 4 \mu\text{m}$ . Primary, secondary, and pseudosecondary inclusions are present in the quartz crystals. The primary inclusions are randomly distributed within a crystal of quartz, with sizes ranging from 2 to 18  $\mu\text{m}$  (Figure. 19 a-d), while the secondary inclusions occur within healed fractures that crosscut multiple quartz crystals. Pseudosecondary inclusions show planar distribution, however, they do not continue until the end of a single crystal of quartz (Figure. 19a). In this study, primary inclusions were selected for the Raman spectroscopy and microthermometry analyses.

Based on the number of phases at a room temperature, 25 °C, as well as the results of laser Raman analysis, the primary inclusions were categorized into three types, which coexist with each other (Figure. 19b). Type I fluid inclusions are aqueous one-phase (liquid) inclusions (Figure. 19a). Type II fluid inclusions are aqueous two-phase (vapor + liquid) inclusions with size ranging from 3 to 18  $\mu\text{m}$  and vapor volume between 10 and 30 % (Figure. 19b-d). More than 50 % of fluid inclusions observed are the Type II inclusions. Type III fluid inclusions are three phase fluid inclusions composed  $\text{H}_2\text{O}-\text{CH}_4-\text{NaCl}$  with sizes ranging from 4 to 18  $\mu\text{m}$  (Figure. 19d).

##### 4.1.7.1 Laser Raman spectroscopy

Representative Type II fluid inclusions of quartz crystals were measured using laser Raman spectroscopy to determine gas compositions. The Type I and II inclusions veins are dominated by  $\text{H}_2\text{O}$  and  $\text{CH}_4$  (Figure. 36a, c, d), while Type III inclusions mainly contain  $\text{H}_2\text{O}-\text{CH}_4-\text{NaCl}$  (Figure. 19d). The vapor phase and liquid phase of type II inclusions are dominated by  $\text{CH}_4$  (Figure. 19e).

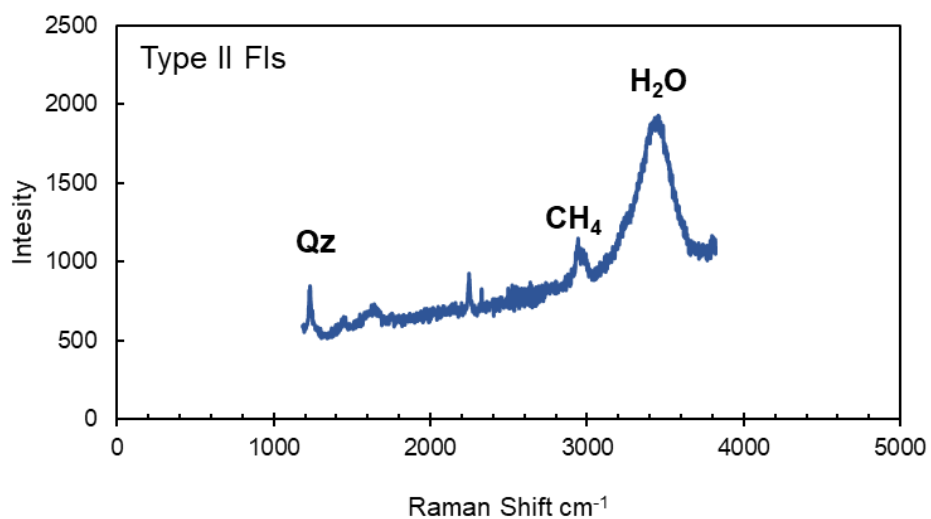
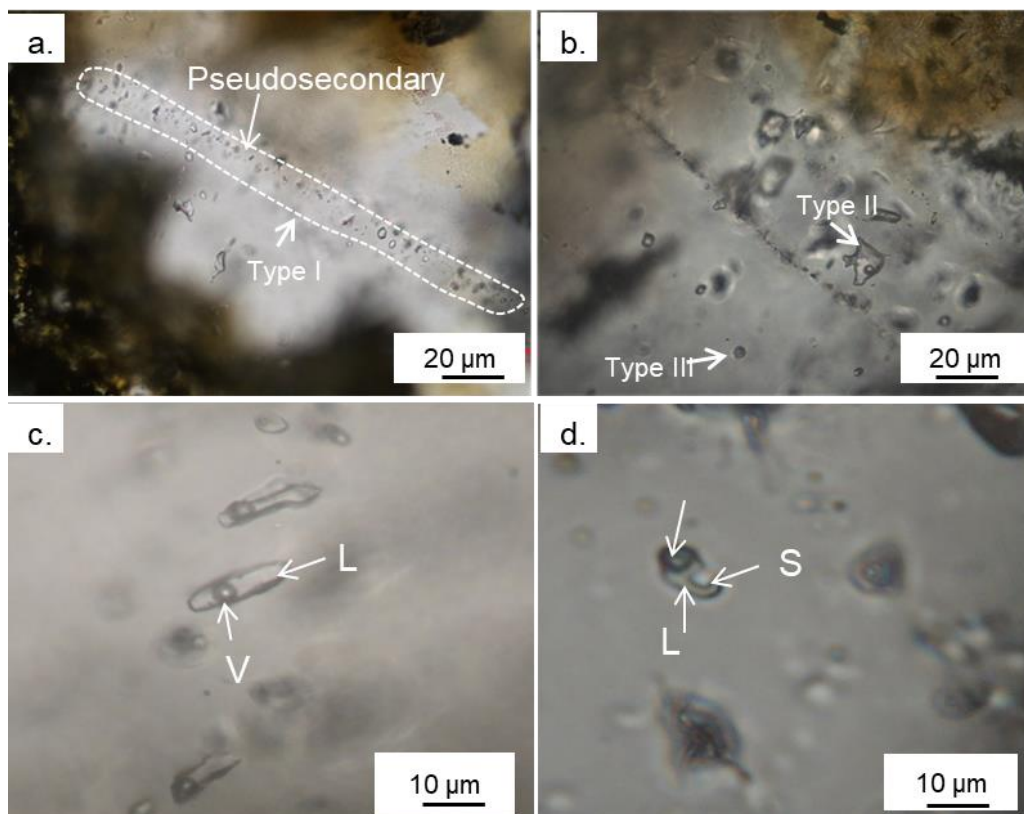


**Figure 19:** Photomicrographs of fluid inclusions at the Mugomo deposit at room temperature (a) type I fluid inclusion (b) large individual fluids inclusions; (c) type II inclusions with long and regular shape; (d) irregular type III multi-phase inclusion composed of 3 phases inclusions L+V+S.

#### 4.1.7.2 Microthermometry

At room temperature ( $\sim 25^{\circ}\text{C}$ ), the type I fluid inclusions are composed by one-liquid phase, type II fluids are composed by two phases (L/V) and the type III is composed by three phases (L/V/S) (Figure. 19).

The early-stage hydrothermal stage of quartz crystals contains dominantly primary fluid inclusion (type II) secondary fluids inclusion (type I), however, the secondary fluid inclusions were not measured. Some fluid inclusions homogenized to liquid, while others homogenized to vapor. The homogenization temperatures ( $T_h$ ) of type II range from 200 to  $439^{\circ}\text{C}$ , with salinity varying between 1 to 15 NaCl wt.% equiv. (Figure. 20). The homogenization temperature for type III fluids range between 300 to  $450^{\circ}\text{C}$  with salinity 25- 28 NaCl equiv.

The homogenization temperature and salinity data are plotted in the binary diagram shown in Figure.21, no positive or negative correlation was observed in all analyzed samples.

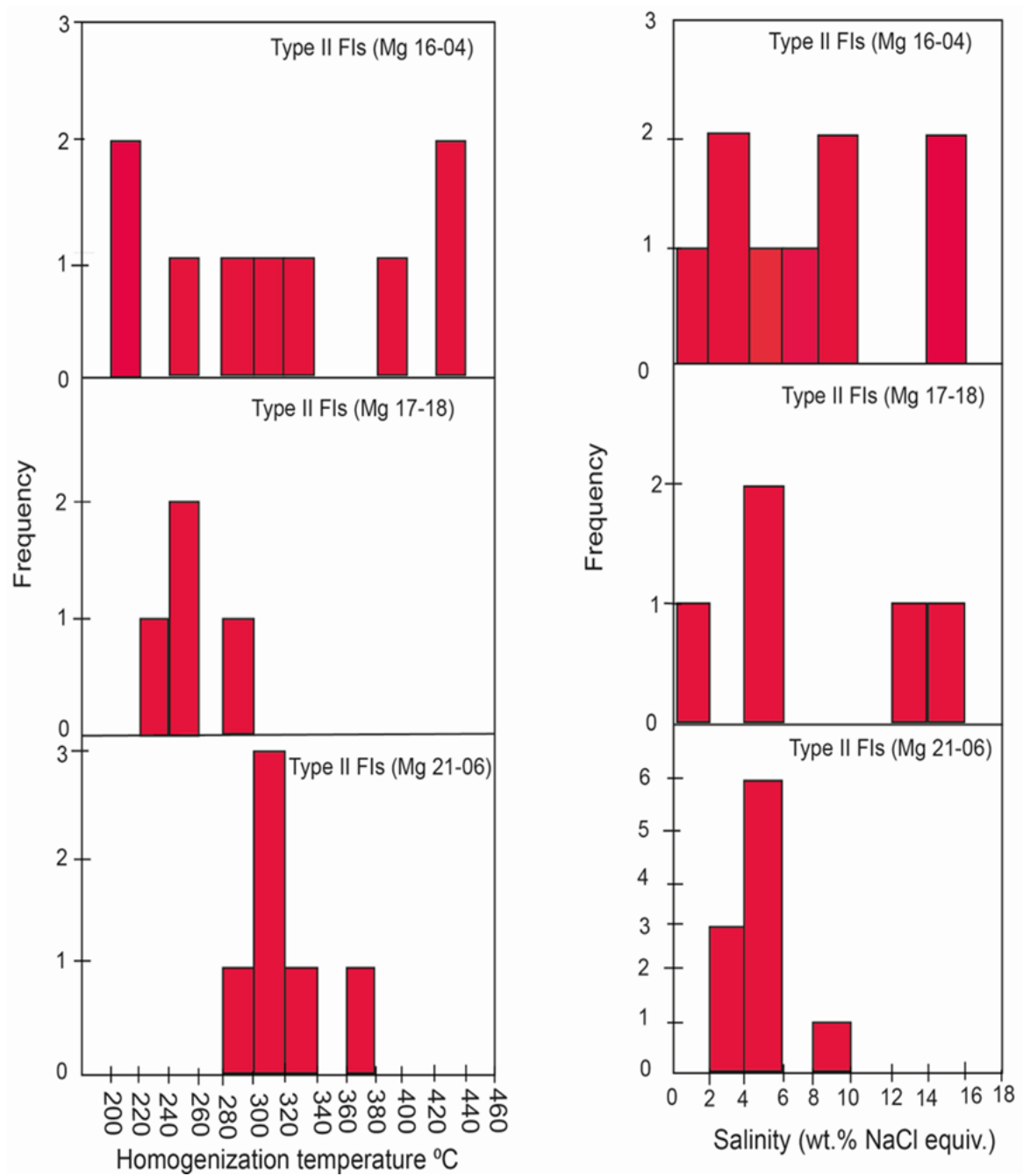


**Figure 20:** Histograms of homogenization temperatures (Th) and salinity of fluid inclusion type II in quartz veins of the Mugomo deposit.

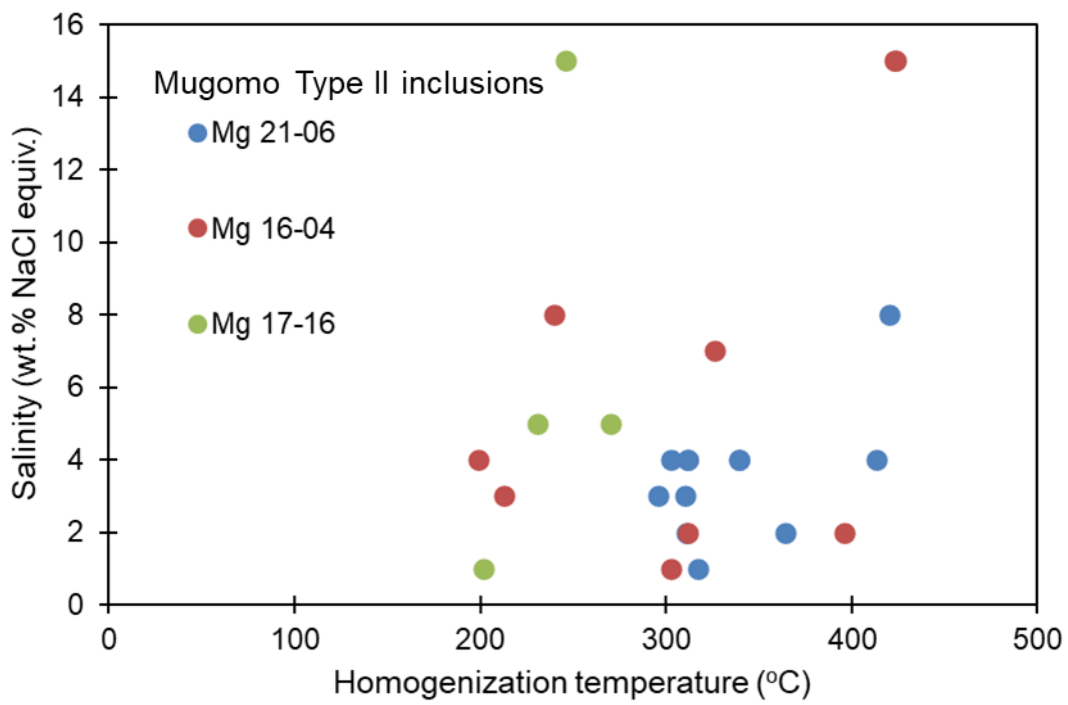


**Figure 21:** Homogenization temperatures versus salinity plot for the fluid inclusions of the Mugomo deposit.

### Sulfur Isotope

Sulfur isotope ratios were determined for 8 sulfide samples including pyrite disseminated in quartzite and metavolcanic rocks. The  $\delta^{34}\text{S}$  values obtained are shown in Table 9 and Figure 22. The  $\delta^{34}\text{S}$  values of pyrite range from +2.5 to +3.8 ‰ with an average of +3.5 ‰.

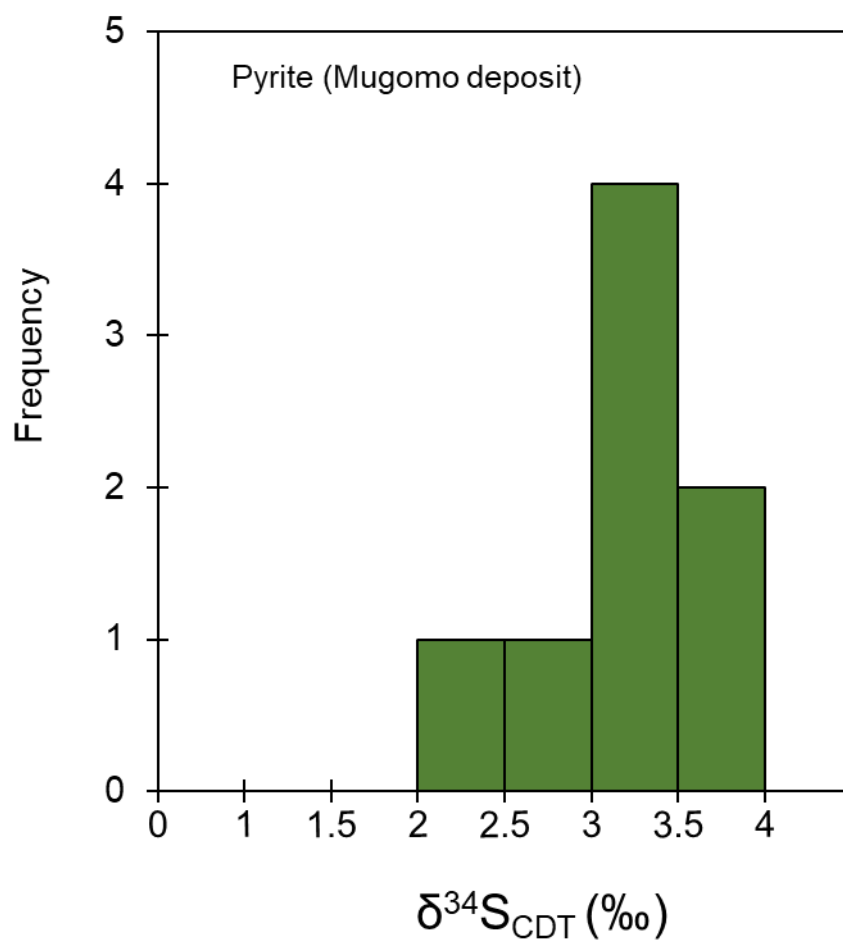


**Figure 22:** A histogram of  $\delta^{34}\text{S}$  (‰) data for pyrite from the Mugomo deposit.

## **4.2 Chifumbazi deposit**



#### 4.2.1 Petrography of the host rock

Gneiss and quartz-mica-schist occur in outcrops of the Chifumbazi deposit (Figure. 23a). Although the gneiss is in contact with quartz-mica-schist, quartz and chlorite veins are hosted only by the quartz-mica-schist (Figure. 23b-c).

The gneiss is composed of medium-coarse-grained quartz, biotite, and muscovite (Figure 24a) and is highly foliated (Cossa et al., 2023). These minerals align in the same orientation.

As part of the Furancungo Suite, quartz-mica-schist (meta-granodiorite) contains metamorphosed biotite granite and granodiorite (GTK Consortium, 2006; Westerhof et al., 2008, Cossa et al., 2023). The quartz-mica-schist is foliated and contains dominant plagioclase, quartz, with minor biotite, actinolite, muscovite and accessory rutile opaque minerals and disseminated pyrite. Sericite associated with chlorite is produced by the alteration of plagioclase (Figure. 24b and e), and opaque minerals. Biotite associated with actinolite (Figure. 24c) usually occurs as small aggregates and gives a spotted appearance to the rock. Rutile is surrounded by plagioclase associated with quartz (Figure. 24d) (Cossa et al., 2023). Pyrite is associated with sericite and chlorite (Figure. 24e), sometimes with sericite alone (Figure. 24f) (Cossa et al., 2023).



**Figure 23:** Photos of the host rock and country rocks at the Chifumbazi deposit: (a) gneiss in discordant contact with quartz-mica-schist; (b) gneiss without vein; and (c) quartz-mica-schist cut by milky quartz veins.

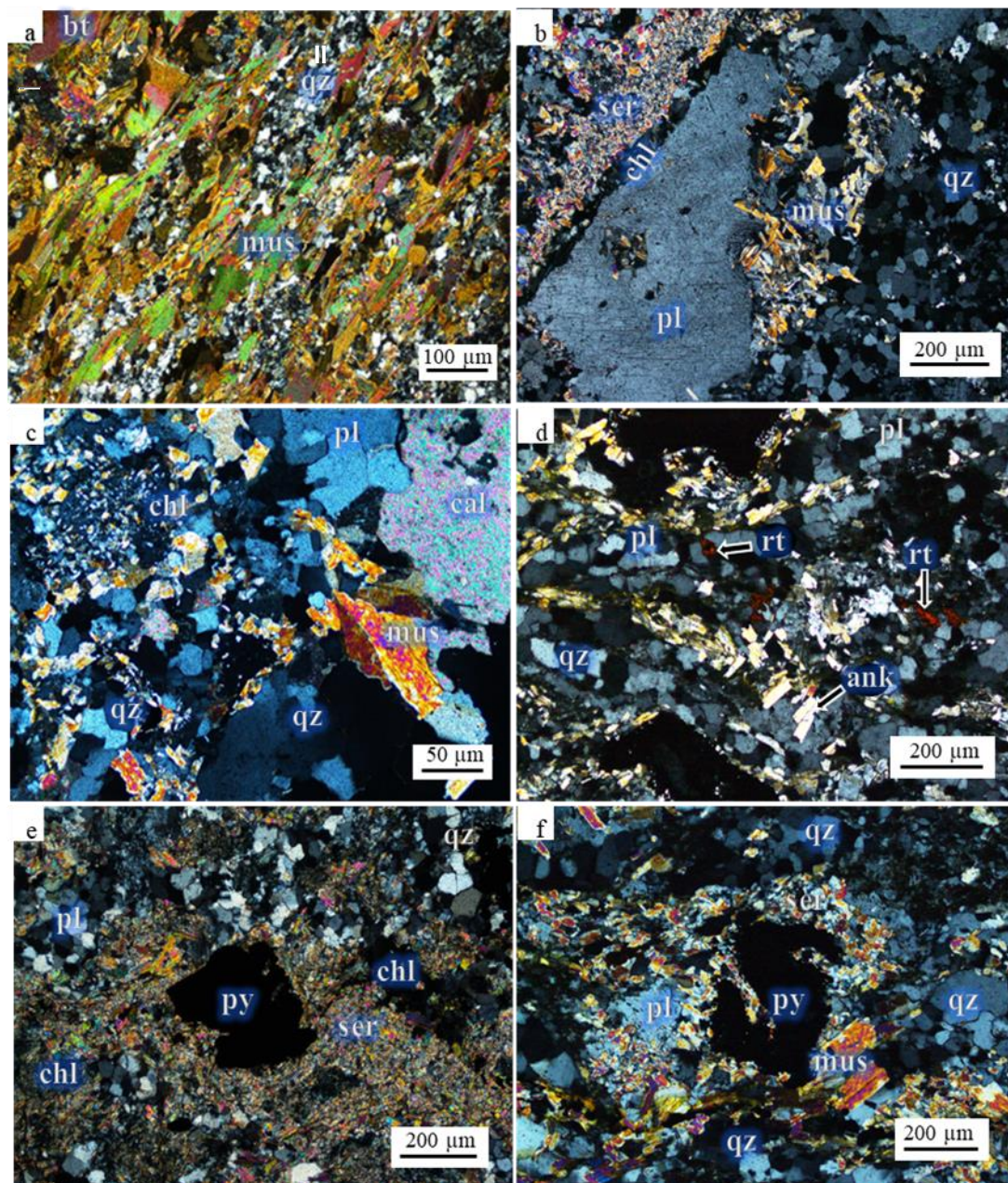


**Figure 24:** Photomicrographs with transmitted light and crossed polars of the host rocks in the Chifumbazi prospect: (a) a gneiss with lepidoblastic texture composed of quartz and muscovite; (b) a quartz-mica-schist composed of plagioclase and quartz with sericite and chlorite alteration; (c) a quartz-mica-schist composed of plagioclase, quartz, muscovite with calcite and chlorite as alteration; (d) a quartz-mica-schist composed of plagioclase, rutilite, quartz, actinolite and pyrite; (e) a quartz-mica-schist composed of quartz, chlorite, pyrite associated with sericite and chlorite alteration; (f) a quartz-mica-

schist composed of quartz, plagioclase, muscovite, pyrite associated with sericite alteration. Abbreviations are pl: plagioclase, qz: quartz, bt: biotite, mus: muscovite, rt: rutile, chl: chlorite, ser: sericite, act: actinolite, op: opaque minerals, py: pyrite

#### 4.2.2 Hydrothermal alteration

Hydrothermal alteration is weakly developed at Chifumbazi deposit, and is characterized mainly by chloritization, sericitization, and carbonatization of quartz-mica-schist.

Alteration minerals include sericite, chlorite, and carbonate. Chloritic alteration is found in the whole quartz-mica-schist and overprints the plagioclase and sericite alteration (Figure. 23b, e).

Actinolite is associated with biotite (Figure 24c,d). Rutile is associated with plagioclase, quartz, actinolite and opaque minerals (Figure. 24d). Pyrite occurs as disseminated subhedral crystals associated with sericite and chlorite (Figure. 24e-f).

Sericite, calcite, and chlorite are the main alteration minerals in quartz-mica-schist (Figure. 23b-f). Sericite, calcite, dolomite, and ankerite tend to occur around veins and shear zones, indicating their hydrothermal origin. Chlorite pervasively occurs in the quartz-mica-schist, overprinting plagioclase and sericite, and it is abundant in the mineralized zones (Figure 24b, e,f).

Calcite and ankerite are the most abundant carbonate alteration minerals in the host-rock (Figure 25) and they are also predominant in quartz carbonate veins.

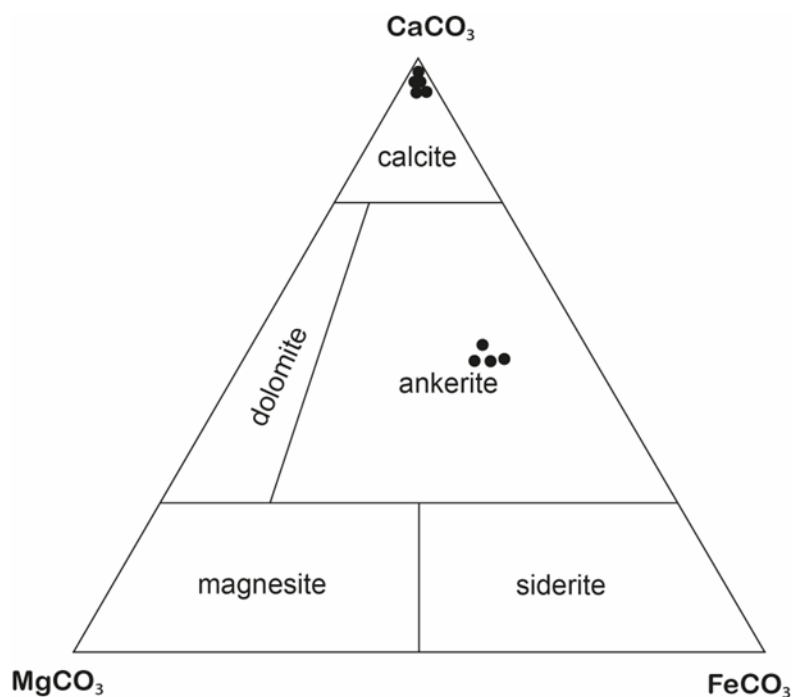


**Figure 25:** Ternary plots of carbonates composition in the  $\text{FeCO}_3$ – $\text{CaCO}_3$ – $\text{MgCO}_3$  apices from the quartz-mica-schist from the Chifumbazi deposit analyzed by EPMA.

#### 4.2.3 Geochemistry of host rock

Bulk chemical compositions of representative samples of quartz-mica-schist in the Chifumbazi deposit are shown in Table 10 and Figure 26. The composition of similar rocks occurring in the Southern Irumide Belt in Zambia (Johnson et al., 2007) has also been compared. The chemical compositions of quartz-mica-schist are  $\text{SiO}_2$  content of 57.9 – 72.4 wt.%,  $\text{FeOT}$  content of 2.9 – 7.5 wt.%,  $\text{Al}_2\text{O}_3$  content of 12.6 – 20.0 wt%, and  $\text{CaO}$  content of 0.2 – 3.7 wt.%. The chemical compositions of quartz-mica-schist of Zambia are  $\text{SiO}_2$  content of 67.2– 76.5 wt.%,  $\text{FeOT}$  content of 2.9 – 9.1wt.%,  $\text{Al}_2\text{O}_3$  content of 10.3 – 14.1 wt%, and  $\text{CaO}$  content of 0.8 – 9.1 wt.%. The  $\text{SiO}_2$ ,  $\text{FeOT}$ , and  $\text{CaO}$  contents of all quartz-mica-schist from the Chifumbazi deposit are comparable to those from Zambia (Johnson et al., 2007); however, they are rich in  $\text{Al}_2\text{O}_3$ . Since the country rocks in the study area are metamorphosed, fluid-mobile elements such as  $\text{CaO}$ ,  $\text{Na}_2\text{O}$ , and  $\text{K}_2\text{O}$ , as well as trace elements such as  $\text{Rb}$ ,  $\text{Sr}$ , and  $\text{Ba}$ , cannot be used to

discuss original rock compositions, fractionation and assimilation pathways, or tectonic setting (Humphris and Thompson, 1978; Brekke et al., 1984; Brouxel and Lapierre, 1988; Johnson et al., 2007). The whole-rock composition data of the quartz-mica-schist (Table 10, appendix 3) in the Chifumbazi deposit (this study) and the meta-diorite and meta-granodiorite in Zambia, Southern Irumide Belt (Johnson et al., 2007; Table 11) are plotted in Harker diagrams shown in Figure 26. Negative correlation was observed between  $\text{TiO}_2$ ,  $\text{Fe}_2\text{O}_3$ ,  $\text{MgO}$ , and  $\text{SiO}_2$  (Figure. 26a-c), while trace elements such as Y and Nb are positively correlated with  $\text{SiO}_2$  (Figure. 26d-e). The concentration of Zr is not correlated with that of  $\text{SiO}_2$  either the quartz-mica-schist or meta-diorite (Figure. 26f). The immobile elements ratios of Nb/Y and Zr/ $\text{TiO}_2$  suggest that the protolith of quartz-mica-schist are rhyolite dacite or dacite (Figure 27).

The rare earth element (REE) and trace element compositions of quartz-mica-schist were plotted in diagrams normalized to chondrite and primitive mantle, respectively (Table 2, Figure. 28a-b). The chondrite-normalized REE patterns of quartz-mica-schist in the Chifumbazi deposit indicate enrichment of light REE (LREE) over mid REE [(La/Sm) N = 3.83 – 7.79] and mid-REE over heavy REE (HREE) [(Gd/Yb)N=1.25 – 1.99], and negative Eu anomalies ( $\text{Eu}/\text{Eu}^*=0.47 - 0.63$ , Figure. 28a). The primitive mantle-normalized trace element patterns of quartz-mica-schist in the Chifumbazi deposit indicate enrichment of large ion lithophile elements (LILE) and depletion of Nb, Sr, P, Eu, Ta, and Ti (Figure. 28b). Apart from the high-mobility elements K, Rb, and Sr, they have rich Ba, Th, and U concentrations and are depleted in Nb, Ta, and Ti, which are associated with subduction (Pearce, 1982).

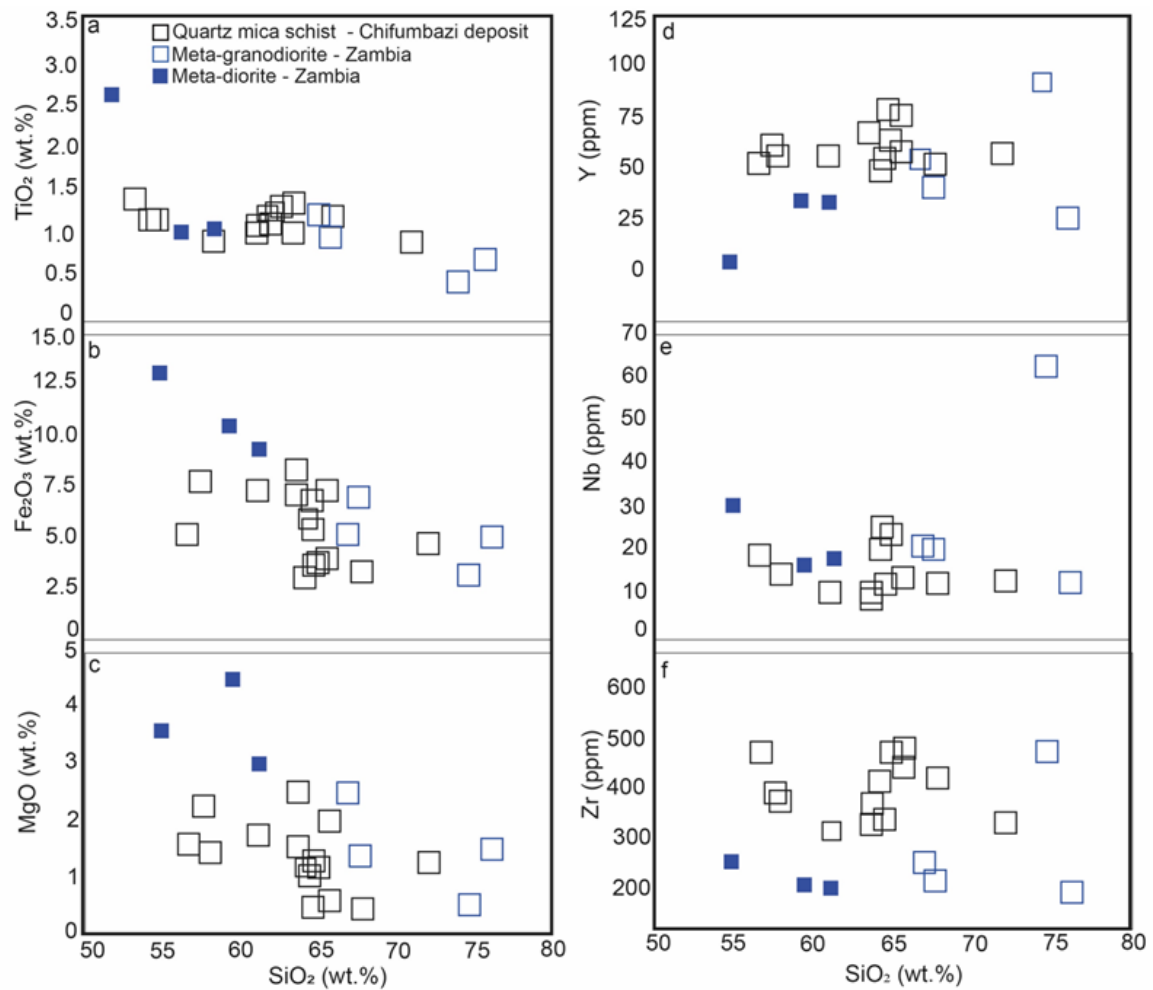


**Figure 26:** Harker diagrams for whole-rock chemical compositions of quartz-mica-schist in the Chifumbazi deposit and meta-diorite and quartz-mica-schist in Zambia belonging to the Southern Irumide Belt. The data of meta-diorite and quartz-mica-schist in Zambia are taken from Johnson et al. (2007).

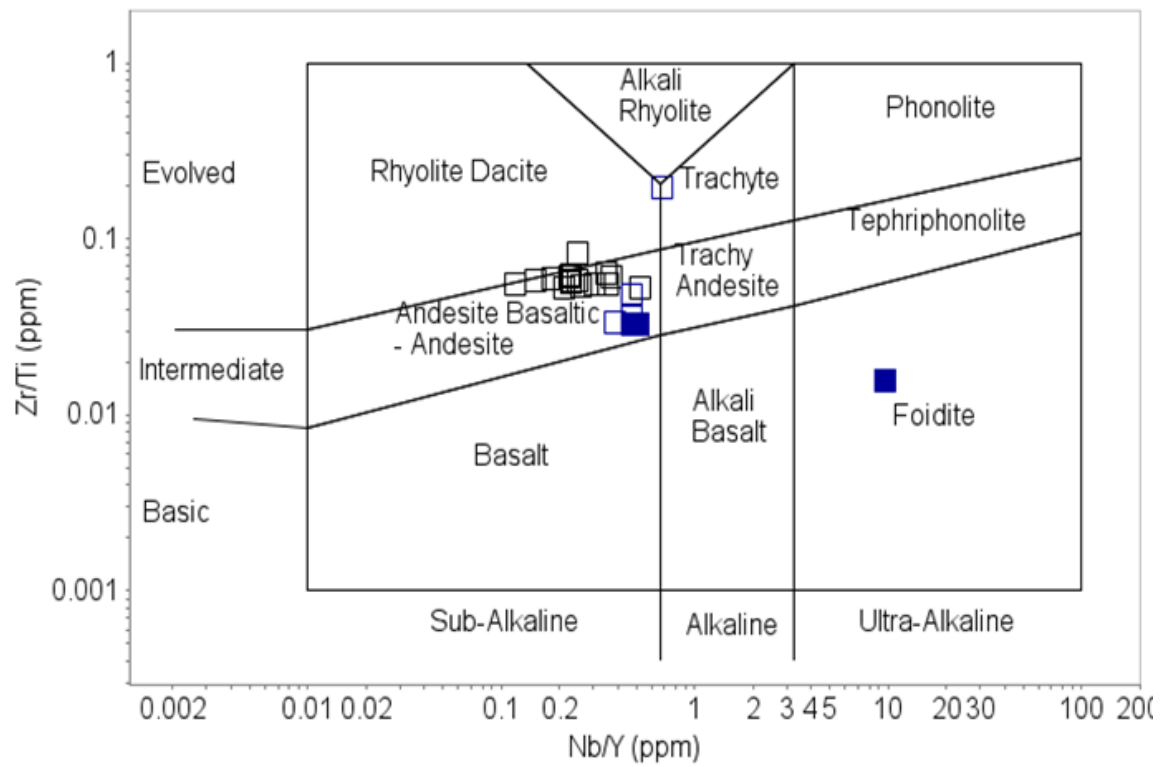


**Figure 27:** Zr/Ti versus Nb/Y plot (after Pearce 1996) for the quartz mica schist from the Chifumbazi deposit, meta-granodiorite and meta-diorite of Zambia.



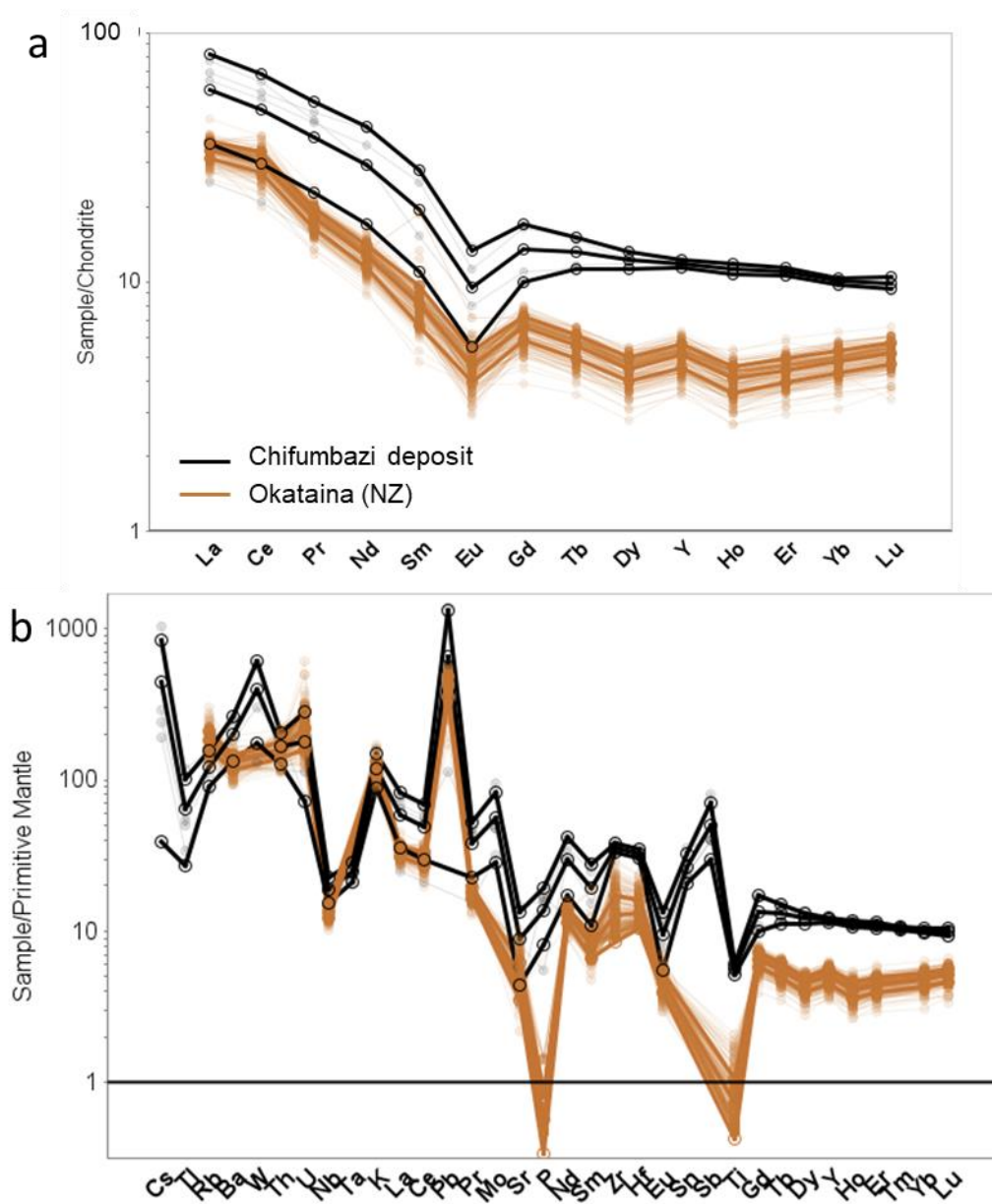


**Figure 28:** Diagrams of chondrite-normalized REE patterns (a), and primitive mantle-normalized trace element patterns (b) of quartz-mica-schist in the Chifumbazi deposit. Normalization values are from Sun and McDonough (1989).

#### **4.2.4 Ore occurrence and petrography of Chifumbazi deposit**

##### **4.2.4.1 Mode of occurrence of veins**

Four successive quartz-carbonate (calcite, dolomite, and ankerite), and chlorite generations of veins were identified in the quartz-mica-schist of the Chifumbazi deposit. These veins occur with different orientations (Figure. 29a). Quartz is the main constituent in all the veins that contain sulfides, except for the chlorite-pyrite veins and veinlets. Quartz-carbonate (QC) veins are cut by 1 – 10 cm wide chlorite veins and veinlets (Figure. 29b), as well as the milky quartz (MQ) vein (Figure. 29c). The MQ veins are 5 – 95 cm wide (Figure. 23c). Clear quartz (CQ) veins which co-precipitated within MQ and QC veins, primarily as veinlets and are also crosscut by chlorite-pyrite veinlets (Figure. 29b). Ferruginous quartz (FQ) veins are 1 – 6 cm wide, and exhibit a red color and occur with the CQ veins (Figure. 29d). The chlorite-pyrite veins and veinlets in the Chifumbazi deposit crosscut the QC, MQ, and CQ veins (Figure. 29e). Under the microscope, the QC veins are characterized by the occurrence of mosaic Quartz in association with dolomite, calcite, and ankerite, with minor sericite (Figure. 30a-b). On the other hand, the MQ veins consist mainly of Quartz, with minor calcite, muscovite, biotite, and albite (Figure. 30c-d).

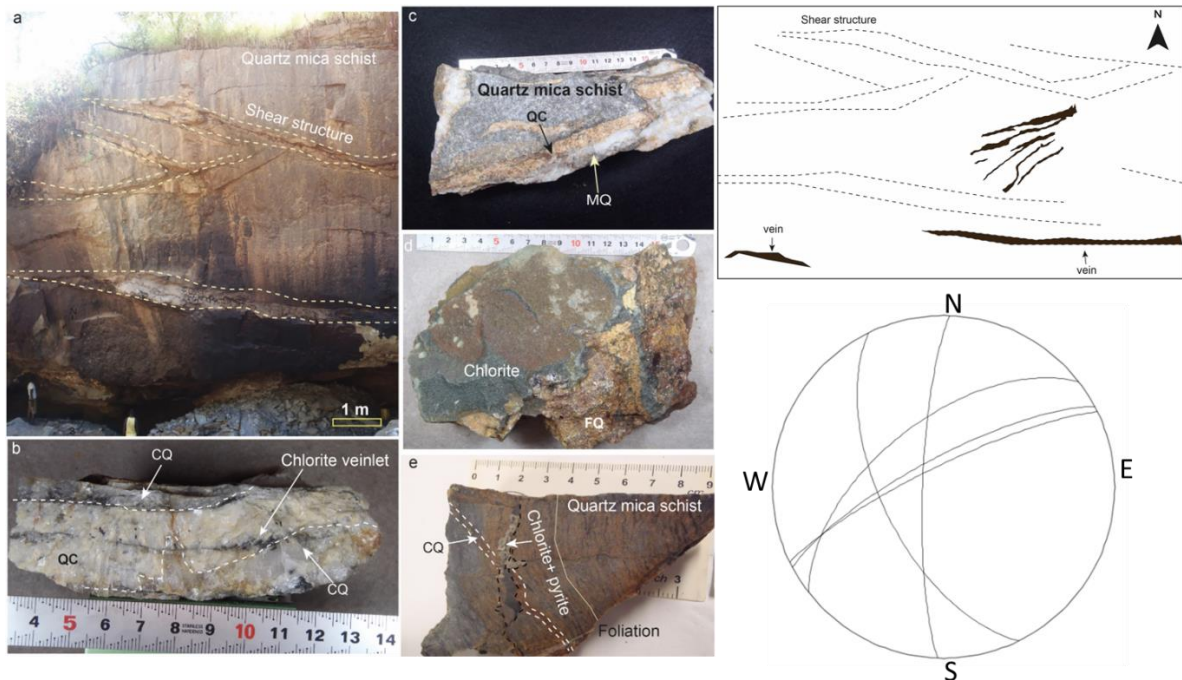


**Figure 29:** Photos of an outcrop and hand specimen samples from the Chifumbazi deposit: (a) meta-granodiorite cut by shear zones and veins with E–W, SW–NE and NNW–SSE directions; (b) a clear quartz (CQ) veins in contact with a quartz-carbonate (QC) vein and chlorite veinlets cutting the CQ veins; (c) a QC vein occurring together with milky quartz (MQ) vein. The CQ vein was cut perpendicularly by a small fault that does not crosscut MQ vein, indicating that the MQ vein was formed after QC vein; (d)

chlorite associated with ferruginous quartz (FQ) vein; and (e) altered meta-granodiorite hosting a chlorite-pyrite veinlet parallel to the foliation of rock, which cut a CQ vein.

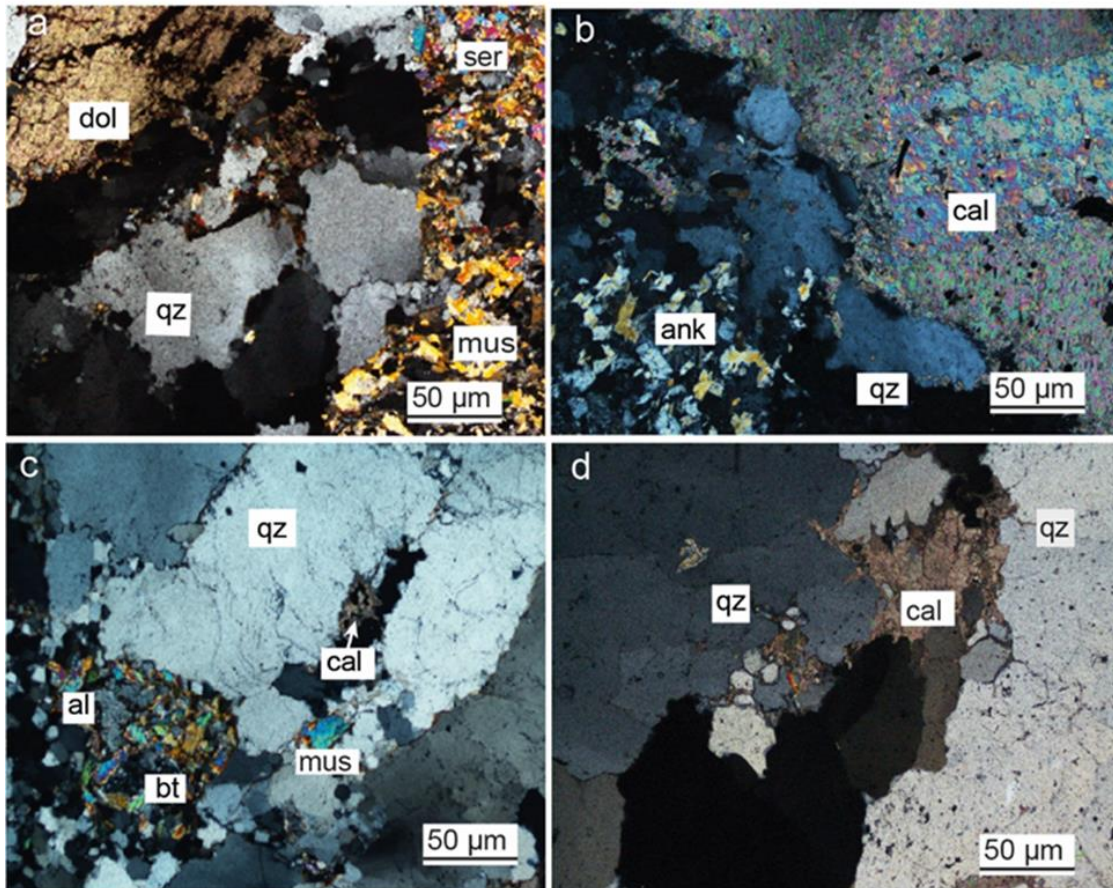


**Figure 30:** Photomicrographs with transmitted light and crossed polars: (a) dolomite and sericite surrounding quartz in a quartz-carbonate (QC) and milky quartz (MQ) veins; (b) coexisting quartz, calcite and ankerite with minor chlorite in a quartz-carbonate (QC) vein; (c) quartz, minor calcite, muscovite and albite enveloping quartz in a milky quartz (MQ) vein; (d) calcite filling interstices of quartz grains in a milky quartz (MQ) vein. Abbreviations are al: albite, qz: quartz, mus: muscovite, chl: chlorite, ser: sericite, ank: ankerite, cal: calcite, dol: dolomite

#### 4.2.4.2 Mineralized host rock

##### Mineralization sequence and mineral assemblages

The mineralization in the Chifumbazi deposit can be divided into four stages based on crosscutting relationships of the veins and veinlets and mineral assemblages (Cossa et al., 2023). Stages I to III are primary mineralization, and Stage IV is supergene oxidation (Cossa et al., 2023). Stage I, represented by the QC veins, consists of quartz, carbonates dolomite, calcite, ankerite, pyrite, chalcopryrite, pyrrhotite, and galena (Figure. 31a-b) (Cossa et al., 2023). Stage II, represented by the MQ (milky quartz), CQ (clear quartz), and FQ (ferruginous quartz) veins, is mainly composed of quartz, pyrrhotite, pyrite, chalcopryrite, and native gold and is the main mineralization stage (Figure. 31c-f) (Cossa et al., 2023). Stage III is mainly composed of chlorite and pyrite in the chlorite-pyrite veins (Figure. 31g) (Cossa et al., 2023). Stage IV consists of secondary minerals of goethite, bornite, and covellite (Figure. 31h) (Cossa et al., 2023). The paragenetic sequence of the Chifumbazi deposit is shown in Figure 32. Based on ICP-MS analyses, gold occurs in Stage II, where bulk compositions of the veins revealed the highest metal contents, five ppm Au, 30 ppm Ag, 8064 ppm Cu, 310 ppm Ni, 85 ppm Te, and 66 ppm Pb (Table 12; Figure. 33) (Cossa et al., 2023).

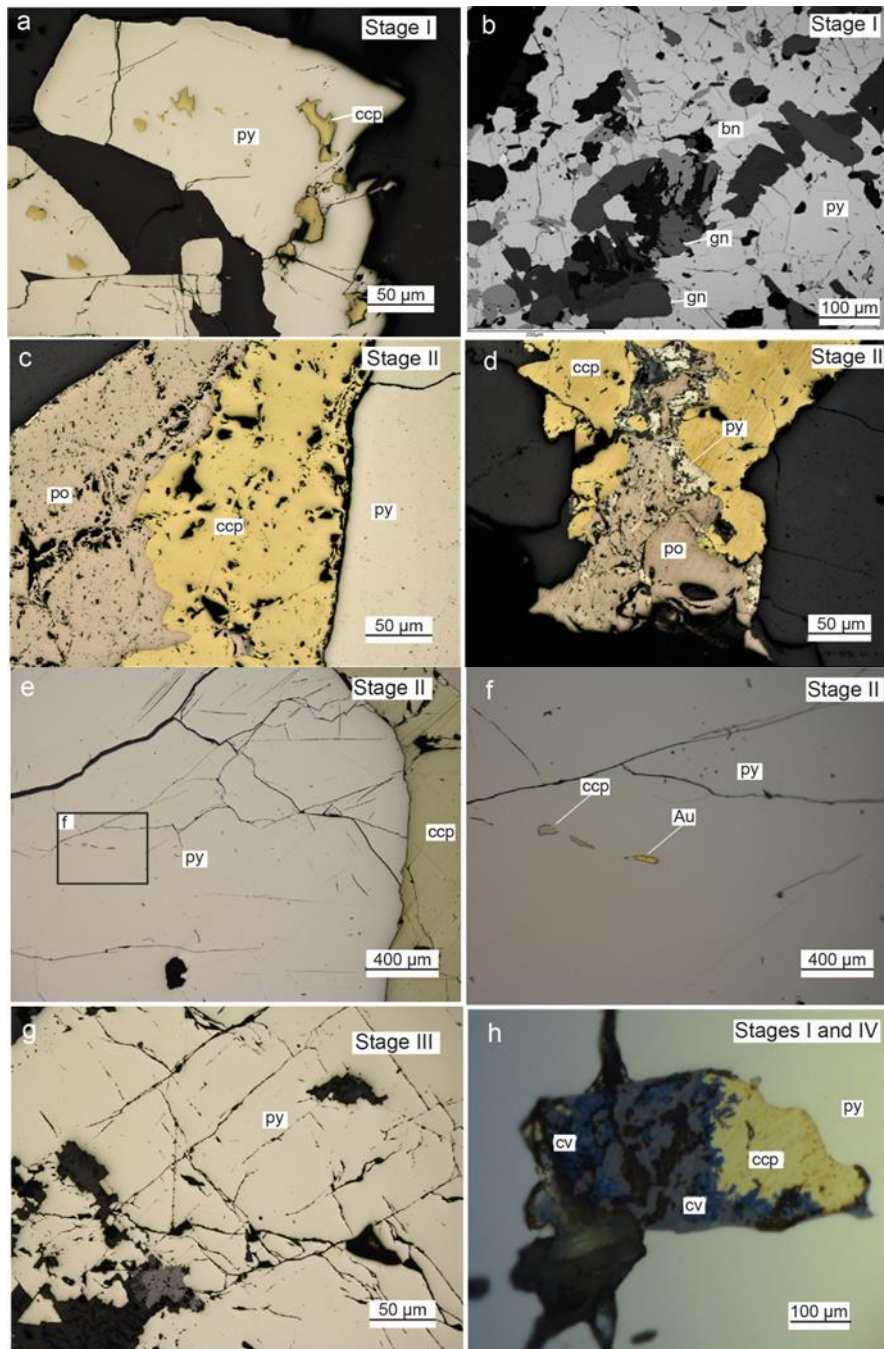


**Figure 31:** Reflected light photomicrographs and backscattered electron image of the sulfides of different mineralization stages in the Chifumbazi deposit: (a) chalcopyrite occurring as inclusions or filling microfractures in pyrite (Stage I); (b) a backscattered electron image of bornite and galena overgrowing pyrite (Stage I); (c) pyrrhotite, chalcopyrite and pyrite intergrown in a quartz vein (Stage II); (d) chalcopyrite intergrown with pyrite which partially replaced anhedral pyrrhotite (Stage II); (e-f) pyrite intergrown

with chalcopyrite, with inclusions of native gold and chalcopyrite within pyrite (Stage II) a rectangle in (e) is enlarged in (f); (g) euhedral pyrite of Stage III with features; and (h) chalcopyrite of Stage I partially replaced by covellite of Stage IV. Abbreviations are Au: native gold; ccp: chalcopyrite, po: pyrrhotite, py: pyrite, bn: bornite, cv: covellite.

Stage and vein type		I	II	III	IV
Minerals		QC	MQ, CQ and FQ		
Ore minerals	Pyrite	Abundant	Abundant	Abundant	Abundant
	Chalcopyrite	Trace	Abundant	Abundant	Abundant
	Pyrrhotite	Trace	Abundant	Abundant	Trace
	Bornite	Trace	Trace	Trace	Trace
	Galena	Trace	Trace	Trace	Trace
	Native gold	Trace	Trace	Trace	Trace
	Covellite	Trace	Trace	Trace	Abundant
Gangue minerals	Quartz	Abundant	Abundant	Abundant	Abundant
	Dolomite	Abundant	Abundant	Abundant	Abundant
	Calcite	Abundant	Abundant	Abundant	Abundant
	Ankerite	Trace	Trace	Trace	Trace
	Albite	Trace	Trace	Trace	Trace
	Muscovite	Trace	Trace	Trace	Trace
	Sericite	Trace	Trace	Trace	Trace
	Chlorite	Trace	Trace	Abundant	Abundant
	Goethite	Trace	Trace	Trace	Abundant

Abundant    
 Minor    
 Trace

**Figure 32:** Paragenetic sequence of mineralization in the Chifumbazi deposit. Abbreviations are QC: quartz-carbonate vein; MQ: milky quartz vein, CQ: clear quartz vein; and FQ: ferruginous quartz vein.

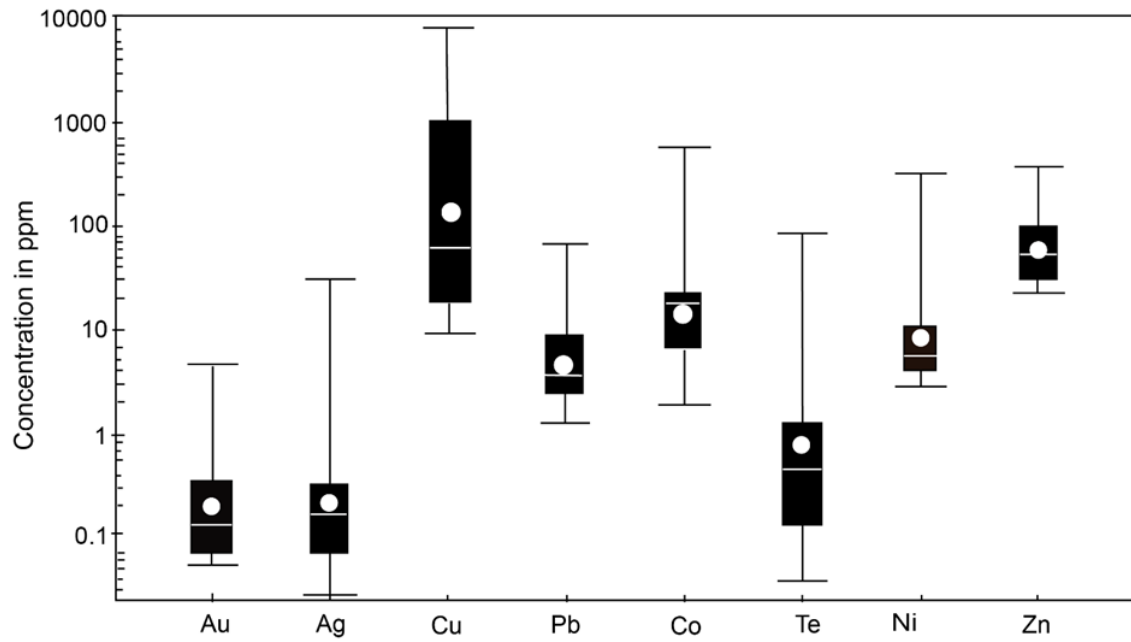


**Figure 33:** Gold, Ag, Cu, Pb, Co, Te, Ni, and Zn contents of the clear quartz (CQ) veins in Stage II from the Chifumbazi deposit, determined by ICP-MS analysis.



#### 4.2.5 Trace element concentrations in quartz

I analyzed concentrations of trace elements (Na, Al, Ti, K, and Fe) of quartz for two and one samples from the CQ veins (sample ID: CF-28 and CF-40) and the FQ veins (sample ID: CF-08) of Stage II, respectively (Table 13 appendix 3), using an electron microscope (Cossa et al., 2023). Quartz in the CQ veins contains relatively lower concentrations of trace elements than those in the FQ veins (Figure.34a-d). About 75% of the Ti contents of quartz are below the detection limit for both the CQ and FQ veins (Cossa et al., 2023).

Regarding the CQ veins (CF-28 and CF-40), the Na content of quartz ranges from 10 to 30 ppm (Figure. 34a), which is below the detection limit (Cossa et al., 2023). The Al content of CF-28 ranges from 10 to 100 ppm; however, that of CF-40 is below the limit of detection (Figure. 34b) (Cossa et al., 2023). The Ti content ranges from 10 to 50 ppm, of which about 75 % are below the limit of detection (Figure. 34c) (Cossa et al., 2023). The K content ranges from 30 to 150 ppm (Figure. 32d), and Fe content ranges from 30 to 280 ppm, with the highest datum reaching 900 ppm (Cossa et al., 2023).

Regarding the FQ vein (CF-08), the Na content of quartz ranges from 10 to 430 ppm (Figure. 34a) (Cossa et al., 2023). The Al content ranges from 10 to 400 ppm, with the highest datum reaching 2299 ppm (Figure. 34b) (Cossa et al., 2023). The Ti content ranges from 10 to 60 ppm, of which more than 50% are below the detection limit (Figure. 34c) (Cossa et al., 2023). The K content ranges from 30 to 200 ppm (Figure. 32d), and the Fe content ranges from 30 to 1260 ppm, with the highest datum reaching 2170 ppm (Figure. 34d) (Cossa et al., 2023). Iron is the most abundant trace element in quartz of the FQ vein, followed by Al and Na (Cossa et al., 2023).

Most of the Al/K values of quartz of the CQ and FQ veins are 0.1-1.0, and some of those of the FQ vein show relatively higher values (Figure. 35a) (Cossa et al., 2023). The Al/K values near 0.69, based on the ratio of the atomic weight of Al (26.98) and K (39.10), would indicate coupled substitution of Al<sup>3+</sup> and K<sup>+</sup> for Si<sup>4+</sup> in quartz (Müller et al., 2002; Takahashi et al., 2008; Rusk, 2012), and those more than 1 for the FQ vein indicate excess Al. The data of the FQ vein indicated a positive correlation between Al contents and Al/Fe ratios, suggesting coupled substitution of Fe<sup>3+</sup> and K<sup>+</sup> for Si<sup>4+</sup> as well (Figure. 35b) (Cossa et al., 2023).

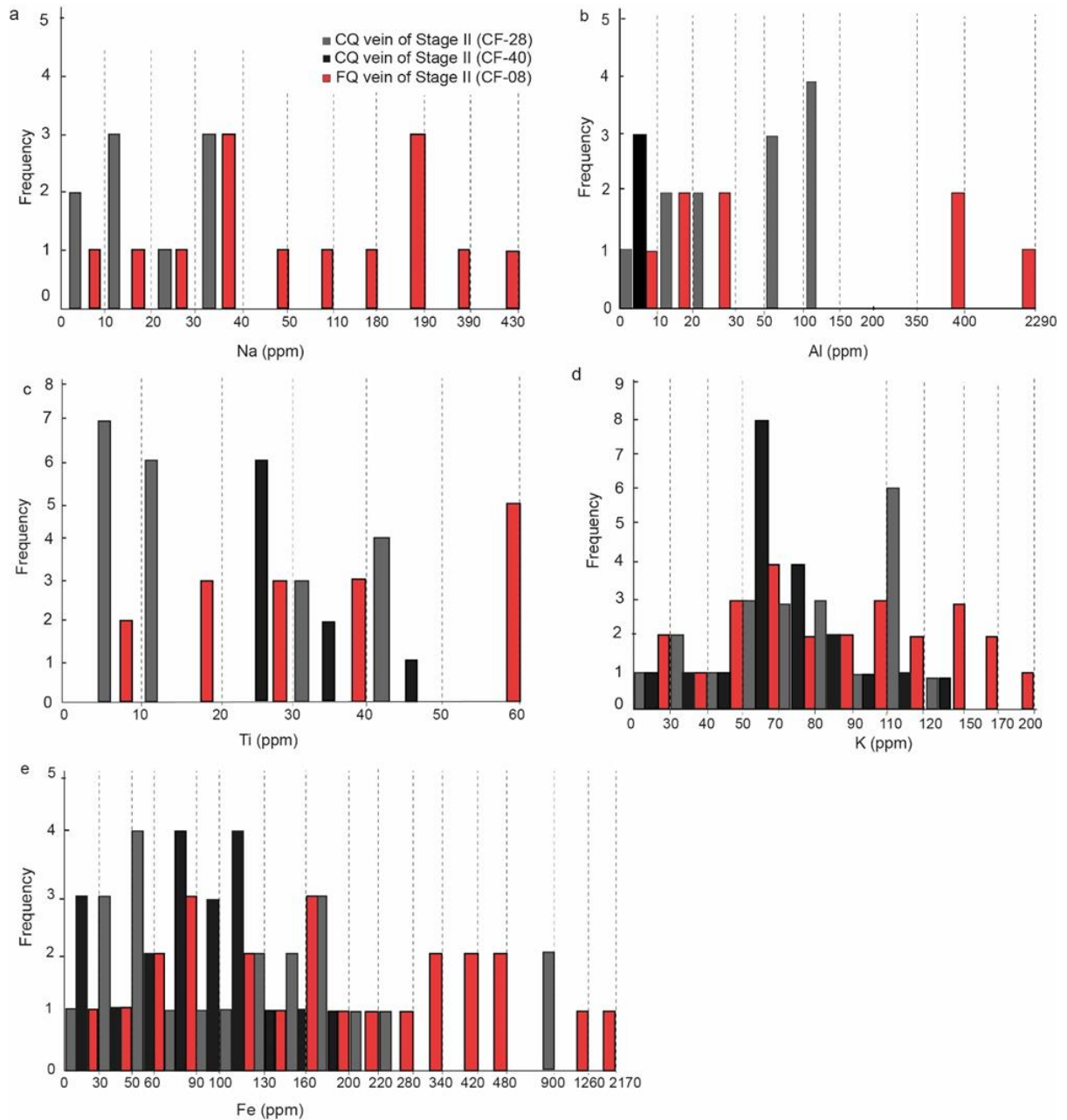


**Figure 34:** Histograms of the trace element contents of quartz based on EPMA analysis for clear quartz (CQ) and ferruginous quartz (FQ) veins of Stage II in the Chifumbazi deposit.

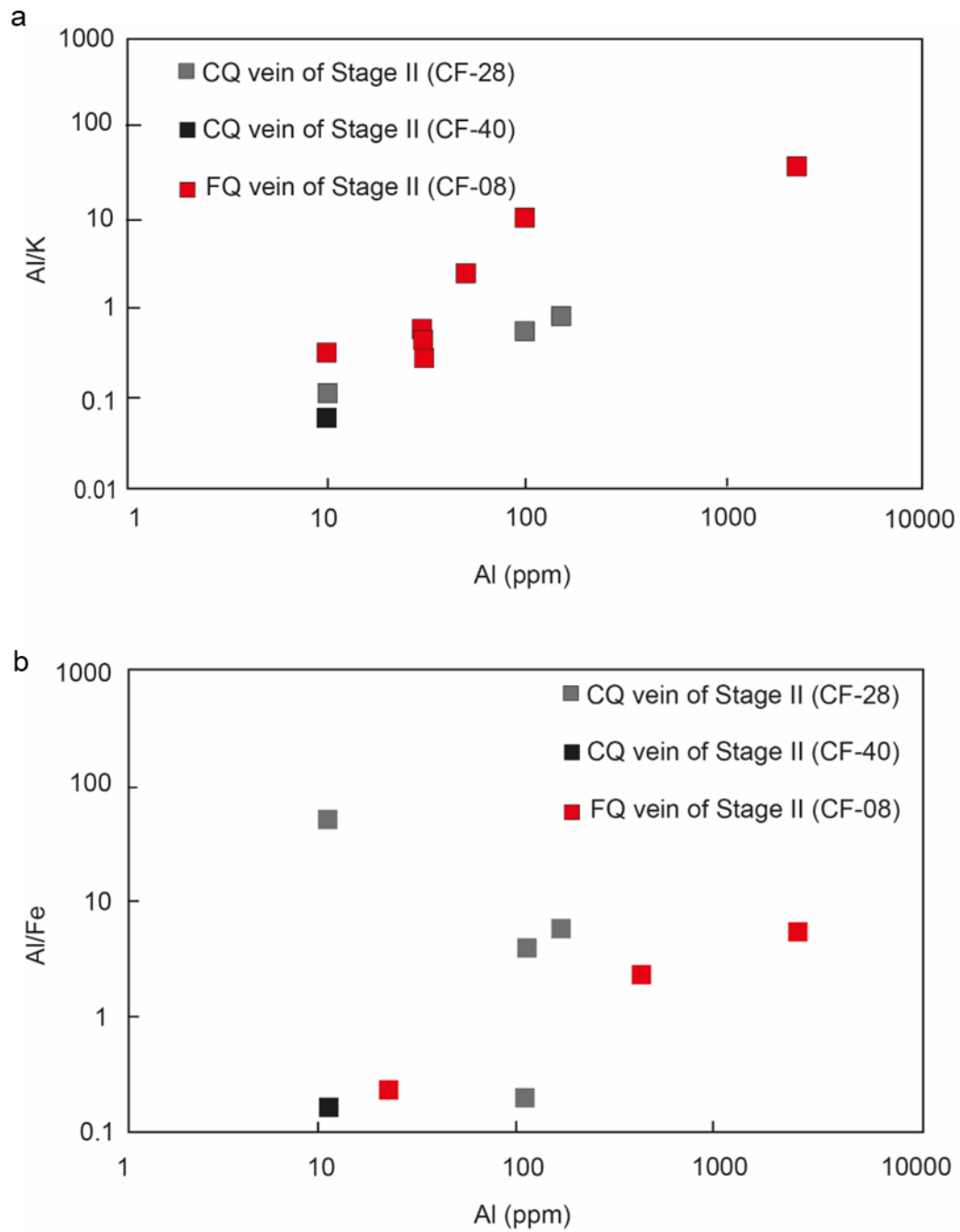


**Figure 35:** (a) Al/K versus Al and (b) Al/Fe vs Al in clear quartz (CQ) and ferruginous quartz (FQ) veins of the Chifumbazi deposit.

#### 4.2.6 Petrography of fluid inclusions

Fluid inclusion study was conducted on quartz in the MQ, CQ, and FQ veins of Stage II, the gold mineralization stage. Five doubly polished thin sections were prepared, two from each of the MQ and CQ veins, respectively (Cossa et al., 2023) and one from the FQ veins. Primary, secondary, and pseudo-secondary inclusions are present in the quartz crystals. The primary inclusions are randomly distributed within a crystal of quartz, with sizes ranging from 2 to 20  $\mu\text{m}$  (Figure. 36a). In contrast, the secondary inclusions occur within healed fractures that crosscut multiple quartz crystals. Pseudosecondary inclusions show planar distribution; however, they do not continue until the end of a single crystal of quartz (Figure. 36a) (Cossa et al., 2023). Generally, it is recognized that primary and pseudo-secondary inclusions are trapped during the formation of host crystals and have the information of the fluids responsible for the formation of the host minerals and related ore deposition (e.g., Roedder, 1984). This study selected primary inclusions for the Raman spectroscopy and microthermometry analyses (Cossa et al., 2023).

Based on the number of phases at room temperature, 25 °C, and the results of laser Raman analysis, the primary inclusions were categorized into three types, which coexist with each other (Figure. 36a) (Cossa et al., 2023). Type I fluid inclusions are aqueous one-phase (liquid) inclusions (Figure. 36a). Type II fluid inclusions are aqueous two-phase (vapor + liquid) inclusions with sizes ranging from 3 to 20  $\mu\text{m}$  and vapor volume between 5 and 30 % (Figure. 36a-d) (Cossa et al., 2023). More than 50 % of fluid inclusions observed are Type II inclusions. Type III fluid inclusions are CO<sub>2</sub> one-phase (vapor) and aqueous-CO<sub>2</sub> two-phase (vapor + liquid) inclusions with sizes ranging from 2 to 4  $\mu\text{m}$ , and the vapor volume of the two-phase inclusions vary between 5 and 20 % (Figure. 36b) (Cossa et al., 2023).

#### 4.2.6.1 Laser Raman spectroscopy

Representative fluid inclusions of Stage II quartz crystals were measured using laser Raman spectroscopy to determine gas compositions (Cossa et al., 2023). The Type I and II inclusions of the CQ and FQ veins are dominated by H<sub>2</sub>O (Figure. 36a, c, d), while Type III inclusions mainly contain CO<sub>2</sub> (Figure. 36b) (Cossa et al., 2023). The vapor and liquid phases of type III inclusions are dominated by CO<sub>2</sub> (Figure. 36e) (Cossa et al., 2023). In this study, no CH<sub>4</sub>, N<sub>2</sub>, CO, or H<sub>2</sub> was not detected .

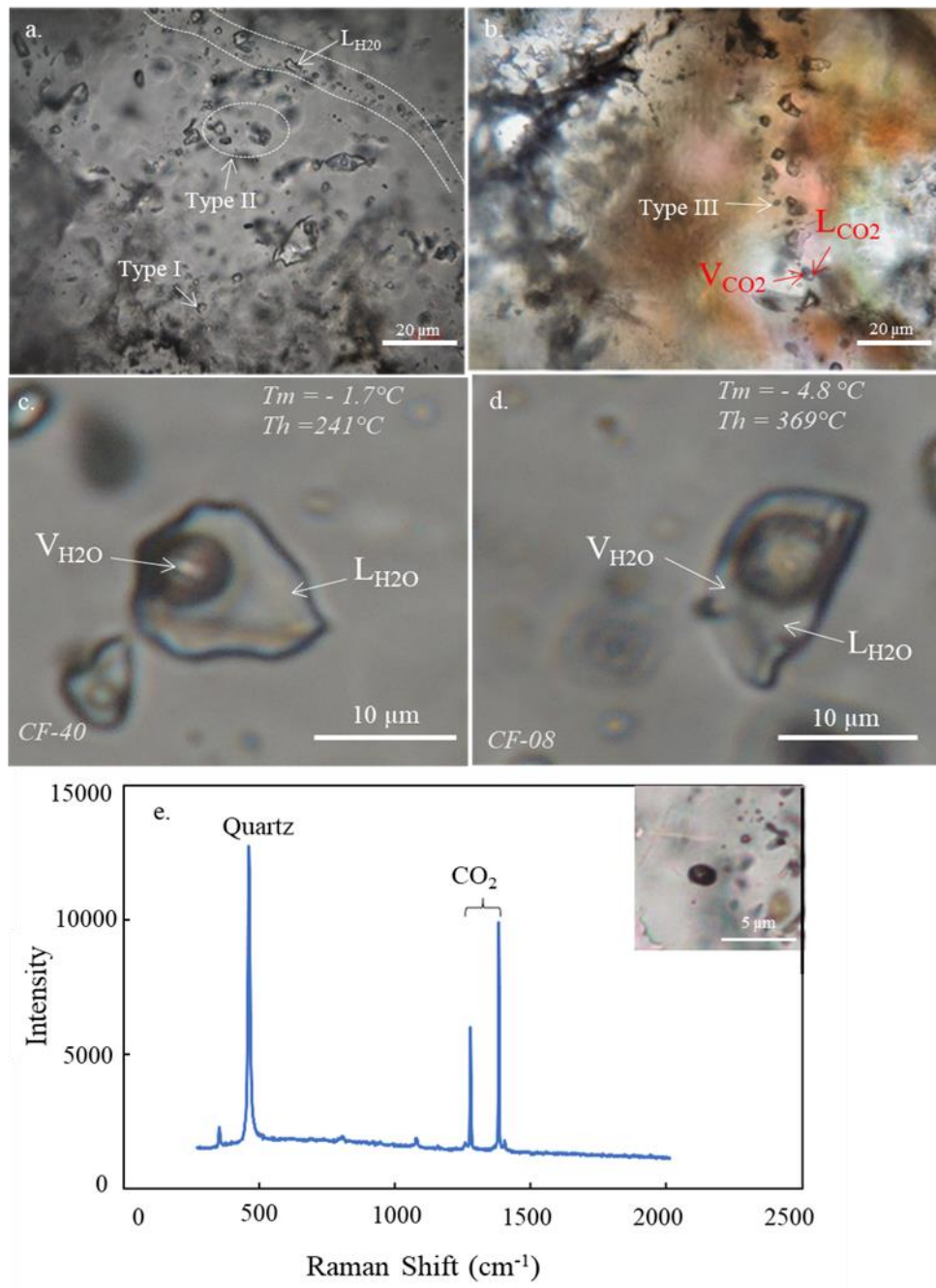


**Figure 36:** Photomicrographs showing fluid inclusions in quartz veins of Stage II of the Chifumbazi deposit: (a, b) fluid inclusions of aqueous one-phase (liquid) (Types I), aqueous two-phase (vapor-liquid) inclusions (Type II), and aqueous- $\text{CO}_2$  one-phase (vapor) and/or two-phase (vapor-liquid) inclusions (Type III); (c, d) isolated Type II fluid

inclusions in quartz crystals; (e) Raman spectra of a Type III fluid inclusion showing the presence of CO<sub>2</sub>.

#### 4.2.6.2 Microthermometry

Microthermometry was conducted for the Type II fluid inclusions in two samples (CF-28 and CF-40) of the CQ veins and one sample (CF-08) of the FQ veins of Stage II (Cossa et al., 2023). The fluid inclusions of the MQ veins as well as the Type I and Type III fluid inclusions are too small to analyze (Cossa et al., 2023). The results of microthermometry analysis are shown in Table 14. The ranges of homogenization temperatures, ice-melting temperatures and corresponding salinity of the Type II inclusions of Stage II are from 219 to 369 °C, from -0.4 to -11.2 °C, and 0.7 – 15.2 wt.% NaCl eq. for sample CF-08 (Figure. 37a, b), from 219 to 304 °C, from -0.7 to -11.3 °C and 2.1 – 15.3 wt.% NaCl eq. for CF-28 (Figure. 37c, d), and from 216 to 288 °C, from -1.7 to -7.9 °C, and 2.9 – 11.5 wt.% NaCl eq. for CF-40 (Figure. 37e, f), respectively (Cossa et al., 2023). The homogenization temperature and salinity data are plotted in the binary diagram shown in Figure 37, no positive or negative correlation was observed in all analyzed samples (CF-08; CF-28, and CF-40) of Stage II (Figure. 38) (Cossa et al., 2023).

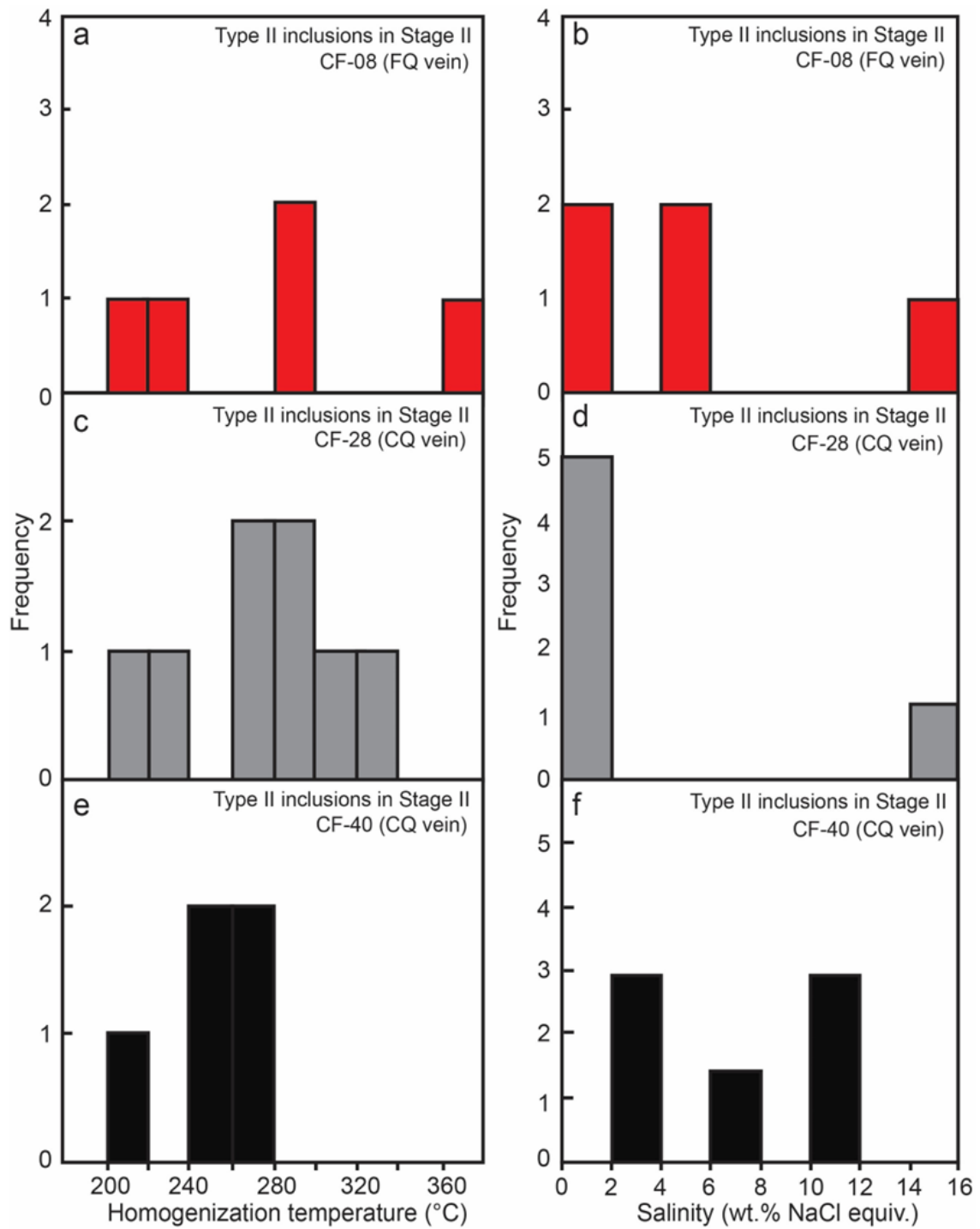


**Figure 37:** Histograms of homogenization temperatures ( $T_h$ ) and salinity of fluid inclusion type II in quartz veins of the Chifumbazi deposit.



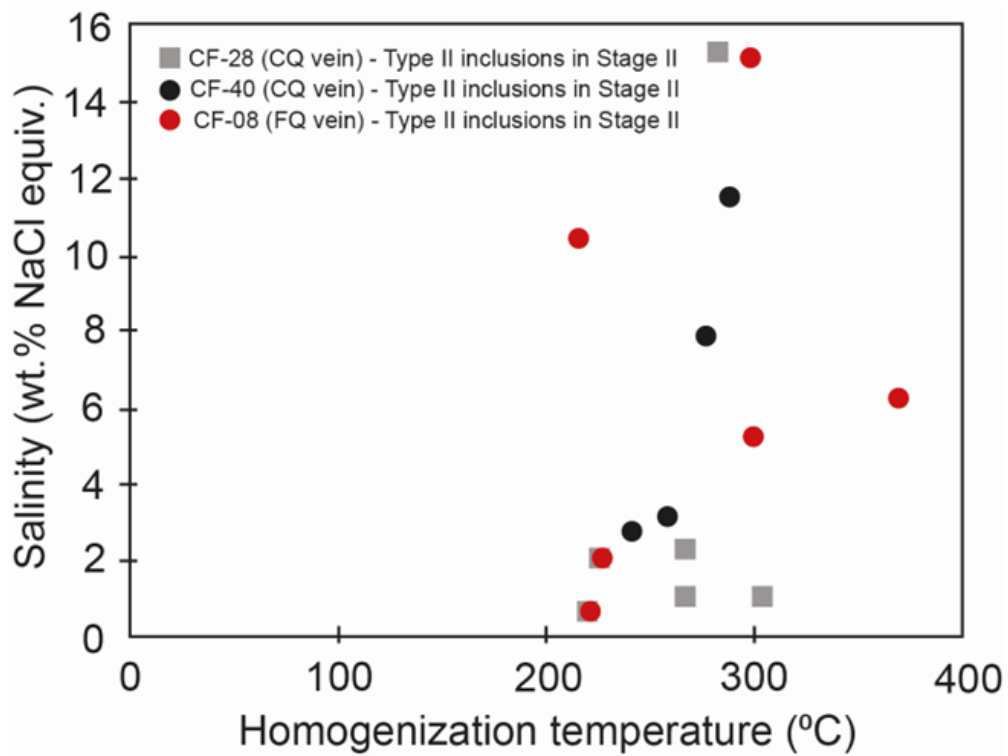


**Figure 38:** Homogenization temperatures versus salinity plot for the fluid inclusions of Stage II from the Chifumbazi deposit.

#### 4.2.7 Sulfur isotopes

Sulfur isotope ratios were determined for 14 sulfide samples including pyrite, and chalcopyrite in MQ, CQ and FQ veins of Stages I and II, chlorite veins of Stage III, and sulfide-disseminated quartz-mica-schist. The  $\delta^{34}\text{S}$  values obtained are shown in Table 6 and Figure 18. The  $\delta^{34}\text{S}$  values of pyrite from Stages I, II and III range from +0.9 to +2.4 ‰ with an average of +1.4 ‰, and those of chalcopyrite from Stages I and II range from +1.1 to +1.4 ‰ with an average of +1.2 ‰. The  $\delta^{34}\text{S}$  value of one pyrite sample separated from the quartz-mica-schist is +2.1 ‰ (Table 16; Figure. 39).

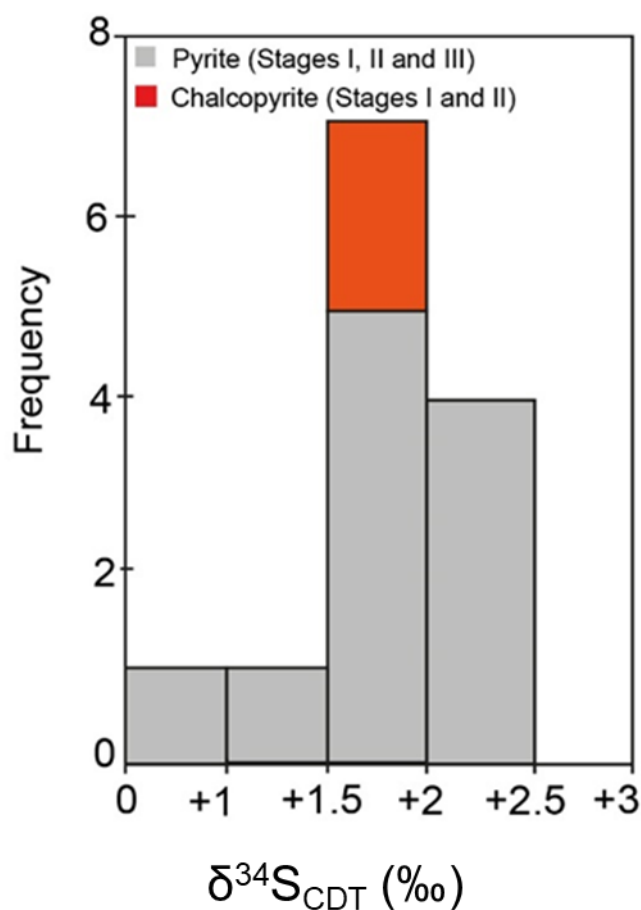


**Figure 39:** A histogram of sulfur isotope compositions of sulfides from the Chifumbazi deposit.

## **5. DISCUSSION**

### **5.1 Hydrothermal alteration**

The formation of ore mineralisation from hydrothermal solutions originated from cooling magma also involves the formation zones of alteration minerals due to chemical changes in the mineralogy of host rocks (Barnes, 1997, Hedenquist and Lowenstern, 1994).

Hydrothermal alteration is weakly developed in the Mugomo and Chifumbazi deposits. Based on the paragenesis and cross-cutting relationship at the Mugomo deposit, the alteration processes can be distinguished as, silicification, epidotization and chloritization consisting of stringer veins and lumpy epidote.

The paragenesis and cross-cutting relationship at the Chifumbazi deposit suggest that the alteration processes can be distinguished as sericitization, chloritization and carbonatization. Sericite and calcite are commonly found replacing plagioclase in the host rock in both deposits.

Chloritization was observed in both the Mugomo and Chifumbazi deposits. This alteration type consists of replacement of pyroxenes, olivine and amphiboles by chlorite (Figure.11c, f) and (Figure. 24b, e) respectively. Sericitization was observed in the both deposits (Figures 11e and 24b, e, f), and carbonatization (Figures 11f).

### **5.2 Evolution of the mineralizing fluid**

Fluid inclusions can provide information about the conditions during the formation processes of the hydrothermal systems, which allows for inferring the evolution of ore-forming fluids (Chai et al., 2017).

Fluid inclusions (type II and type III) from the first stage of mineralization at Mugomo deposit exhibit medium homogenization temperatures (200°C- 439° C), and moderate salinities (1-15 NaCl wt.% equiv.) (Table 8, appendix 2).

Fluid inclusion of first stage of mineralization from Chifumbazi deposit, exhibits medium homogenization temperature (220°C- 340° C), with salinity varying between (2-15 NaCl wt% equiv.). The presence of CO<sub>2</sub> in fluid inclusion type Ia may have played a critical role in gold transportation (Chian et al., 2017). The interaction of the primary fluid with wall rocks resulted in the precipitation of quartz, sericite, pyrite, and biotite (Figure. 24e, f).

In many hydrothermal systems, gold depositions are associated with fluid immiscibility or boiling mechanism (Chain et al.,2017, Chai et al., 2016a). Fluid immiscibility may also occur at Chifumbazi and Mugomo deposits. The evidence of fluid immiscibility during the early stage is supported by the microthermometric data (Figure 21), which show a similar homogenization temperature (300°C- 450°C) but different salinity values for type II and type III inclusions (type II varying from 2-10 NaCl wt% equiv., and type III from 25-28 NaCl wt% equiv.). Another evidence of fluid immiscibility in the deposits is the coexistence of vapor (gas-rich) fluid inclusion type I and liquid (aqueous-rich) fluid inclusion type II in the same quartz crystal. The type I and type II inclusions likely resulted from the separation of homogeneous carbonic-aqueous fluid that was responsible for the mineralization. The moderate salinity of aqueous fluids inclusions may suggest that the parental fluid was also moderate-high in salinity. Thus, most probably, the type III, free phase inclusion can represent the parental fluid. This also supported the fact that type III inclusions occur together with type I and type II in the same crystal in the Chifumbazi deposit (Figure.36a).

### **5.3 The formation of chlorite and epidote veins**

Epidote veins and veinlets associated with chlorite and quartz crosscut Mugomo deposit host rocks (Figure. 8d). Mineral breakdown in the surrounding rocks often leads to the release of fluids that lead to epidote vein formation (Castelli et al., 1998; Brunsmann et al., 2000). A combination of hydrothermal activity and low metamorphic grades can

produce an epidote (Leighton, 1954). Plagioclase, pyroxene, and olivine are replaced by it in metamorphosed basalts and gabbros. In addition to this, it occurs in schists and marbles (Leighton, 1954). The epidote veins from the Mugomo deposit can be formed by hydrothermal activity, and metamorphism of the protolith of the metavolcanic rock was responsible of the replacement of plagioclase, olive or pyroxene to epidote as an alteration mineral.

The Chifumbazi deposit host rock is crosscut by mineralized milky quartz, quartz-carbonate, and chlorite veins and veinlets (Figure 29). As a result of diagenesis, low-grade metamorphism, and hydrothermal alteration, chlorite is formed in a wide variety of rocks (e.g. De Caritat, 1993, Vidal et al., 2001, Yavuz et al., 2015, Ciesielczuck, 2012). The chlorite mineral is a common ferromagnesian silicate in many sulfide deposits occurring in rocks of wide- spread bulk composition and metamorphic grade (Bryndzia and Scott, 1987), that occurs as an alteration of surrounding rocks in most hydrothermal systems (Martinez-Serrano and Dubois, 1998). In intermediate-felsic igneous rocks, chloritization via dissolution-reprecipitation is a common way to form chlorite (Wang et al., 2018). However, in the Chifumbazi deposit chlorite is formed in the quartz-mica-schist with SiO<sub>2</sub> content varying between 54.05 wt.% - 72.40 wt.% (intermediate to felsic) as an alteration mineral and as veins and veinlets.

It has been proposed that several mechanisms are involved in chloritization (e.g. Ferry, 1979, Parneix et al., 1985, Yuguchi et al., 2015; Wang et al., 2018), which are essential to recognize both inflow and outflow components of hydrothermal fluids. Furthermore, chlorite compositions in hydrothermal alteration zones change systematically with proximity to fluid pathways and hydrothermal veins, making it possible to trace fluid compositions in these zones (Walshe, 1986; Halter et al., 1998; Lanari et al., 2014). A significant finding in exploration is that chlorite exhibits significant lateral and vertical composition changes from the distal to proximal ends of the orebody (Wilkinson et al., 2015; Xiao et al., 2017; Wang et al., 2018). These characteristics were not observed in large scale in the study area. However, the hand specimen samples collected in the alteration zone (Figure 29e) can clearly show the composition changes in the quartz-mica-schist caused by the mineralized chlorite veinlet.

## 5.4 Tectonic Setting

Fractional crystallization would alter magma composition and confuse mantle source features during magma generation and emplacement (Deng et al., 2015). As a result, trace element ratios with similar bulk solid/melt partition coefficients in mafic-ultramafic intrusive rocks (such as Th/U, Nb/U, La/Nb, etc.) are almost independent of fractional crystallization (Deng et al., 2015).

### **Contrasting trace element contents of felsic meta-igneous rocks at Chifumbazi and Mugomo.**

In Mugomo, the host rock shows unfractionated LREE-HREE, moderate LILE, and low P, and is likely to have formed in an extensional margin with light REE and mildly enriched compared to mid-REE ( $La/Sm_N = 0.9 - 2.4$ ), whereas mid- to heavy REE trends are nearly flat, the trace element patterns are not the same as the Okataina arc rhyolite (Figure 40a).

Host-rock at Chifumbazi with enrichment of light REE (LREE) over mid-REE [ $(La/Sm)_N = 3.83 - 7.79$ ] (Figure 40b) and mid-REE over heavy REE (HREE) [ $(Gd/Yb)_N = 1.25 - 1.99$ ], and the trace element patterns are similar with those of Furancungo Suite and the Okataina have a typical volcanic-arc geochemical signature (fractionated LREE-HREE, high LILE, and Pb) and likely formed in a convergent margin (Figure 41).

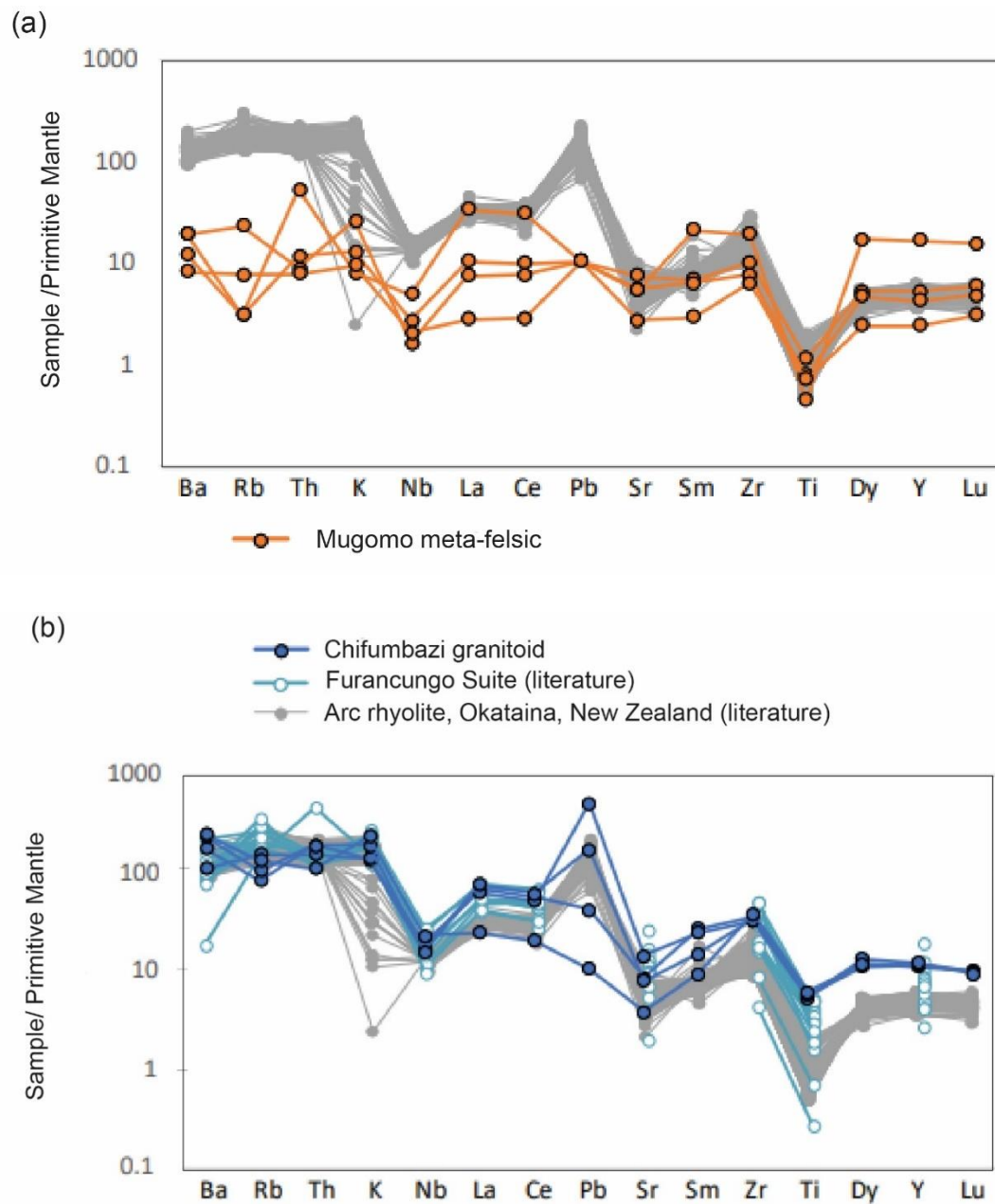


**Figure 40:** Diagrams of primitive mantle-normalized trace element patterns (a) of metavolcanic rocks in the Mugomo deposit compared with the arc rhyolite from the Okataina deposit (data from Deering et al., 2011); (b) of quartz-mica-schist in the Chifumbazi deposit compared to granitoids from the Furancungo Suite (data from GTK

consortium, 2006) and Okataina deposit (data from Deering et al., 2011);. Normalization values are from Sun and McDonough (1989).

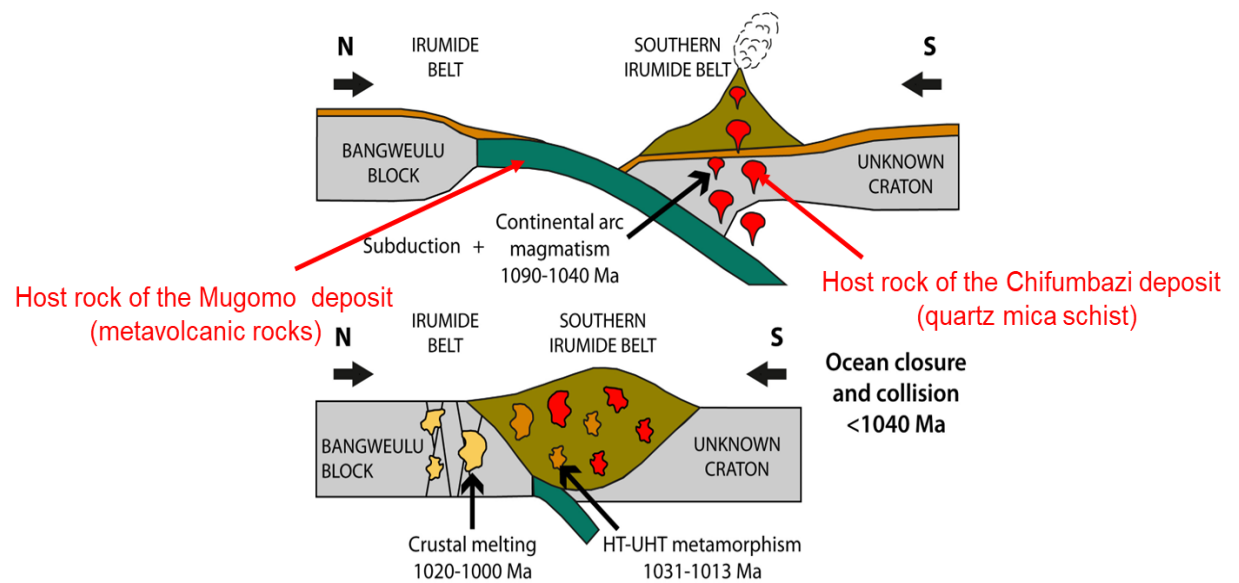


**Figure 41:** Geodynamic model showing the sequence of tectonic-metamorphic events during the Irumide orogeny and an overview map of the Southern Irumide Belt (Karmakara & Schenk, 2016).

## 5.5 Comparison between the veins and shear zones



Regionally, the gold prospects in the northern Tete province are related to a different strike shear zones formed during the Pan -African and Post Pan-African orogens (Muntigh, 2021).

The two main vein orientations at Chifumbazi and Mugomo (NE- SW and approx. N-S) (Figure 42) are similar to regionally occurring fault zones formed during the Pan-African orogenic event (640 – 480 Ma) (Muntigh, 2021):

- Approx. NE-SW striking (related to the Zambezi Orogeny 590-560 Ma)
- Approx. N-S striking (Ross-Delamarian Orogeny 520-480 Ma) (Muntigh, 2021).

The post-metamorphic auriferous veins may have occurred during the Mozambique and Ross- Delamarian Orogens.

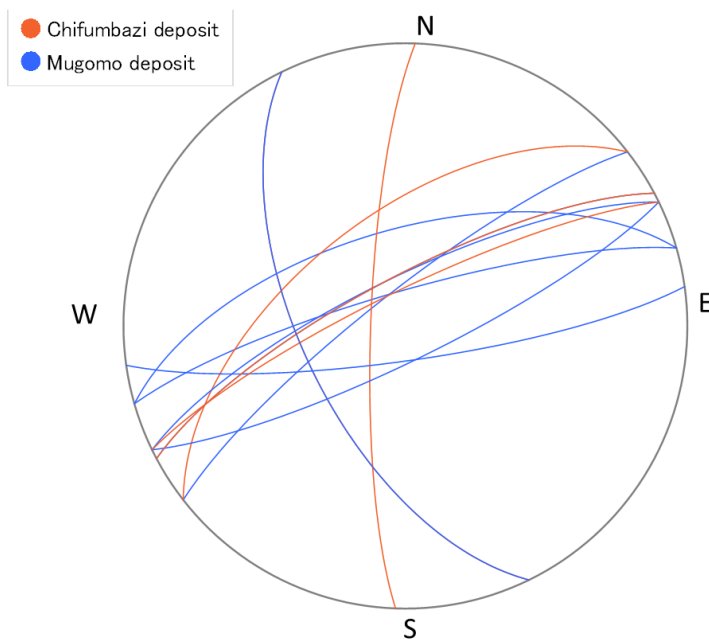


**Figure 42:** Stereonet (lower hemisphere) of vein orientations at Mugomo and Chifumbazi deposits.

## 5.6 Type of mineralization

Based on preliminary scientific evidence, the primary gold mineralization in the Chifunde District including the Chifumbazi deposit has been considered as orogenic-type mineralization, or in other terms, mesothermal mineralization (cf. Groves et al., 1998), where Au (Ag-Cu)-bearing quartz veins were considered to have formed during Neoproterozoic-Phanerozoic granitic magmatism (Muntingh, 2021) through a metamorphic process. The veins in the Chifumbazi deposit are hosted only in Mesoproterozoic quartz-mica-schist, it is possible to say that the Chifumbazi deposit formed after the Mesoproterozoic period. The sulfur isotope values of the sulfides in the Mugomo and Chifumbazi deposits overlap with those of different sources, including other orogenic deposits worldwide (Figure. 43). This precludes the identification of the source of sulfur based solely on sulfur isotope signatures. Nevertheless, the  $\delta^{34}\text{S}$  values obtained falls within most of the reported data for orogenic-type gold deposits, between 0 and 10 ‰ (Goldfarb and Groves, 2015 and references therein).

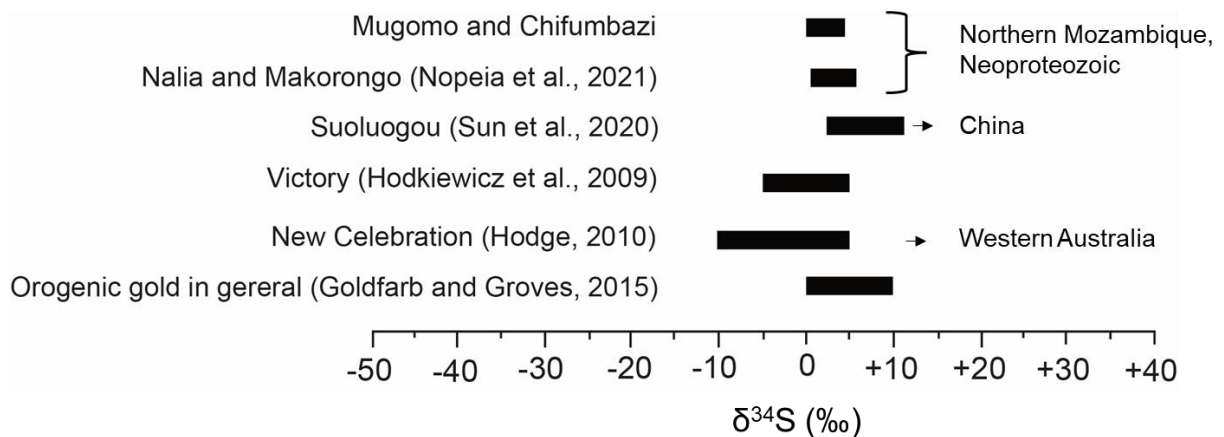


**Figure 43:** Comparison of sulfur isotopic ratios of primary mineralization in the Mugomo and Chifumbazi deposits with other orogenic gold deposits worldwide.

Due to its ubiquitous nature and good chemical resistance, quartz is an excellent mineral for tracking fluid evolution and mineralization types in mineralizing systems (Rusk et al.,

2008; Rusk, 2012; Maydagan et al., 2015; Mao et al., 2017; Rottier and Casanova, 2020; Cossa et al., 2023). Particularly, Al and Ti concentrations of hydrothermal quartz are often used to distinguish the associated ore deposit type (Rusk, 2012). The Al content of quartz in orogenic gold deposits varies between ca. 6 and 1,000 ppm, and Ti content between ca. 0.2 and 100 ppm, whereas it has an Al content between ca. 10 and 300 ppm, and Ti content between 2 and 300 ppm in porphyry deposits (Rusk, 2012; Sun et al., 2021; Cossa et al., 2023, Figure. 20). The Al contents of quartz in the CQ (clear quartz) and FQ (ferruginous quartz) veins from the Chifumbazi deposit are between below the detection limit (<47 ppm) to 2290 ppm, and most of the data indicate <400 ppm, which overlap the general range of orogenic-type gold deposits (Figure. 20) (Cossa et al., 2023). About 75 % of data of Ti content of quartz in the CQ and FQ veins from the Chifumbazi deposit are below the detection limit (< 30 ppm), and others indicate up to 60 ppm Ti (Cossa et al., 2023). The Ti contents of 30-60 ppm are mostly within the range of Ti contents reported for other orogenic-type gold deposits (cf. Rusk, 2012; Sun et al., 2021; Cossa et al., 2023, Figure 44). The data plotted in Al vs Ti diagram Figure 20 fall in both the fields of orogenic and porphyry deposits (Cossa et al., 2023).

Carbonization, sericitization and chloritization observed in the Chifumbazi deposit, are the typical alteration types of orogenic-type gold deposits (e.g. Groves et al., 1998). In general, orogenic-type gold deposits are formed by fluids with salinity commonly below 15 wt.% NaCl eq., relatively high CO<sub>2</sub> contents, and reduced and near neutral pH, and their timing of gold deposition is syn- or post-peak metamorphism (Groves et al., 1998; Ridley and Diamond, 2000; Wilkinson, 2001; Phillips and Powell, 2010; Goldfarb and Groves, 2015; Nopeia et al., 2021). All Type II fluid inclusions in the veins of the Mugomo and Chifumbazi deposits have comparable salinity between 0 and 15.3 wt.% NaCl eq., and the Type III fluid inclusions in the Mugomo deposit are high in salinity (26 - 28 wt%) and those from the Chifumbazi deposit contain CO<sub>2</sub> in the vapor phase (Cossa et al., 2023). The ore mineral assemblage of Stage II is mainly pyrrhotite, pyrite, chalcopyrite and native gold, suggesting a reduced condition for the ore-forming fluids.

Based on the aforementioned alteration type, ore mineral assemblages, characteristics of fluid inclusions, and sulfur isotope signature, the Chifumbazi deposit is likely orogenic-

type gold mineralization. Since the veins in the Chifumbazi deposit are not deformed nor foliated by the regional metamorphism, the timing of gold mineralization was after the peak of deformation (Cossa et al., 2023).

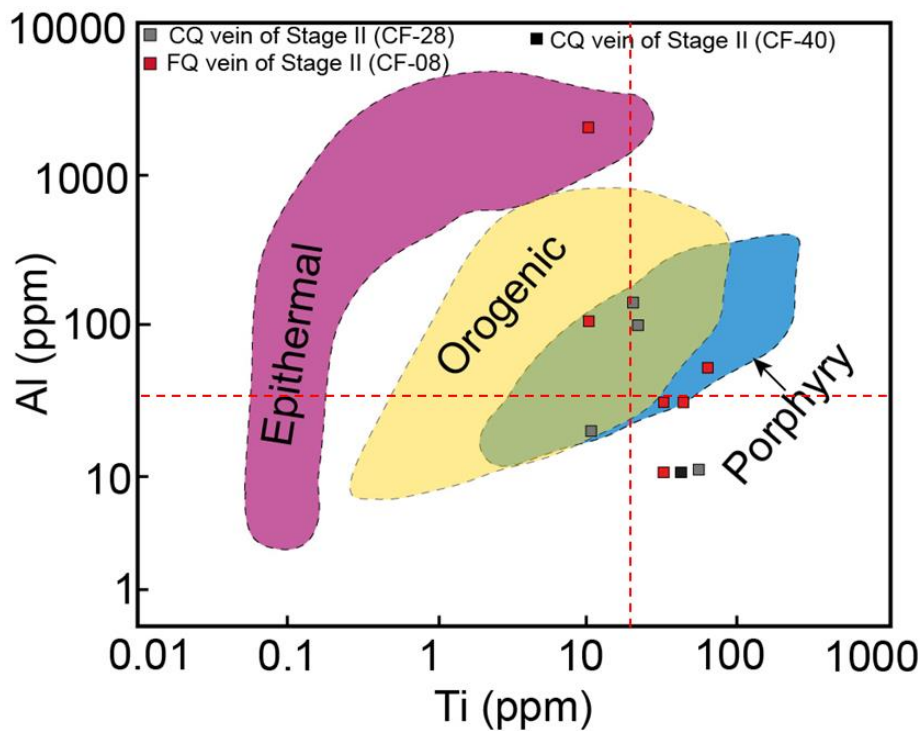


**Figure 44:** Aluminum versus Ti contents of quartz of clear quartz (CQ) and ferruginous quartz (FQ) veins of Stage II of the Chifumbazi deposit with comparison to those of hydrothermal quartz from epithermal, orogenic, and porphyry deposits (modified after Rusk, 2012; Sun et al., 2021).

## 5.7 Ore-forming conditions

Several gold prospects in Tete Province, including the Chifumbazi deposit in the Chifunde District and the Mugomo deposit at the Furancungo area in the Macanga District, are thought to be spatially associated with shear zones (e.g. GTK Consortium, 2006; Cossa et al., 2023), so I consider that the shear structures were the conduits in which gold-bearing hydrothermal fluids migrated (Cossa et al., 2023).

Fluid inclusions hosted in quartz crystals of Stage II, the gold mineralization stage, in the Chifumbazi deposit, exhibit the modes of homogenization temperatures of 240-300 °C, with salinity varying between 0.7 and 15.3 NaCl wt% eq (Figure 20), on the other hand, the fluid inclusion of the Mugomo deposit exhibit homogenization temperatures of 200-439°C, with salinity varying between 1 and 15.0 NaCl wt.% eq (Figure 34) (Cossa et al., 2023). Generally, orogenic-type gold deposits are formed by fluids with salinity <15 wt.% NaCl eq., high CO<sub>2</sub>, and the timing of gold deposition is syn- or post-peak metamorphism (Groves et al., 1998; Phillips and Powell, 2010). The salinity of the Mugomo and Chifumbazi deposits varies between 0- 15 wt% NaCl equiv (Figure. 44) (Cossa et al., 2023).

To consider the trapping temperature of fluid inclusions based on homogenization temperatures, pressure correction is necessary. Although there is no specific pressure nor depth information of ore-formation for both deposits, the occurrence of biotite, muscovite, and actinolite in the country rocks, quartz-mica-schist and biotite schist indicate the greenschist facies metamorphism (Cossa et al., 2023). Reported full-ranges of pressure and temperature (P-T) conditions of the formation of orogenic-type gold deposits in the world are ca. 50–500 MPa and 200–650 °C, respectively (Groves et al., 2003), whereas P-T conditions for those formed in greenschist facies are ca. 150–280 MPa and 200–400 °C (Goldfarb et al., 2005). Applying the pressure range of 150-280 MPa (Goldfarb et al., 2005), the isochores of fluid inclusions (cf. Bodnar, 2003) with the modal homogenization temperatures of 240-300 °C and the salinity of 10 NaCl wt% eq. indicates a range of trapping temperature of fluid inclusions, ca. 325-550 °C for the Mugomo and Chifumbazi deposits (Cossa et al., 2023).

Although CO<sub>2</sub> vapor inclusions are present in the veins of the Chifumbazi deposit (Figure. 15e), the histograms of homogenization temperatures of fluid inclusions do not

show a pattern of fluid boiling (Figures. 21, 38). Furthermore, the binary plot of homogenization temperature versus salinity plot in the Figures 21 and 38 do not show any positive or negative correction suggesting that the boiling process did not take place in the Mugomo and Chifumbazi deposits (Cossa et al., 2023). We consider that the hydrothermal fluids in the Chifumbazi deposit were in a state of effervescence, i.e. degassing of CO<sub>2</sub> was ongoing and CO<sub>2</sub> gas was trapped in the Type III fluid inclusions (Cossa et al., 2023). Solubility of CO<sub>2</sub> in hydrothermal fluids with a P-T condition of 140 MPa and 350 °C and different salinities of 6 wt% and 20 wt% NaCl eq. is 34 wt% and 11 wt% CO<sub>2</sub>, respectively (Takenouchi & Kennedy, 1965). According to Henry's law, the effervescence of CO<sub>2</sub> from the hydrothermal fluids is caused by the decrease in pressure. The hydrothermal fluids were likely migrating from the deeper to shallower portions during the gold deposition process in the Chifumbazi deposit (Cossa et al., 2023).

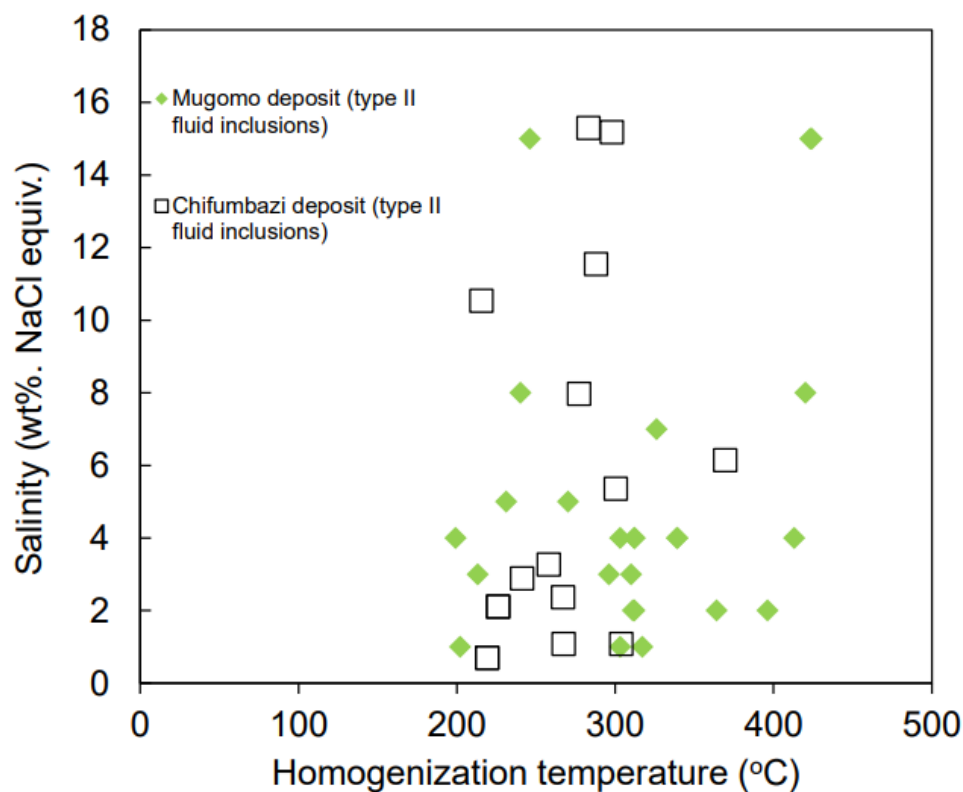


**Figure 45:** Homogenization temperatures versus salinity plot for the fluid inclusions of type II from the Mugomo and Chifumbazi deposits.

### **5.8 Implication to the mineral exploration**

This study is the first academic report that described the details of gold mineralization in the Tete Province, Mozambique. However, other Au deposits in Namuno District, Cabo Delgado Province in northeastern Mozambique were also recently identified as orogenic-type gold (Nopeia et al., 2021). There are many artisanal gold mines as well as small-scale gold mines in Mozambique, and most of their mineralization types based on the geological study are indefinite (e.g. Nopeia et al., 2022). Although the Mugomo and Chifumbazi deposits are a small-scale gold occurrence, it is still worth doing systematic exploration for the deeper portion of the deposit and/or its vicinities as the samples and data of the deposit have been collected from only the surficial and shallow sub-surficial portions (Cossa et al., 2023). According to (Cossa et al., 2023) regional exploration, quartz veins in shear zones can be one of the targets for exploration, whose positions may be examined using geological maps, artisanal mine workings, and remote sensing techniques.

## 6. CONCLUSIONS

This study has allowed defining some key, mineralogical and geochemical characteristics of the mineralization at the Chifumbazi and Mugomo. These two occurrences exemplify the so-far little-known mineralization of Tete province Au. Mineralization in the Mugomo deposit is characterized by epidote  $\pm$  chlorite and quartz + sulfide vein hosted in metavolcanic rocks and biotite-schist.

The mineralization in the Chifumbazi deposit is characterized by milky quartz vein, quartz + carbonate vein, and chlorite veins hosted in quartz-mica-schists.

The metavolcanic rocks and biotite-schist of the Mugomo deposit were altered to quartz, chlorite, and epidote, while the quartz-mica-schists of the Chifumbazi deposit were altered to sericite, calcite, and chlorite.



The ICP-MS data from the Mugomo deposit suggest that gold is present in the metavolcanic rocks with a concentration up to 2 ppm. In the Chifumbazi deposit gold was detected in the veins with a concentration about 5 ppm .

Sulfur isotopic compositions of sulfides are higher in the Mugomo deposit (+2.5 to +3.8 ‰) than those in the Chifumbazi deposit (+1.0 to +2.5 ‰).

Primary gold mineralization in the Chifumbazi prospect, in the northern Tete province, is predominantly hosted by quartz-mica-schist which is composed of plagioclase, quartz, actinolite, biotite, calcite, chlorite, and sericite, thus this metamorphic rock is grouped into greenschist facies. In this type of metamorphic facies, orogenic gold deposits are mostly found (Groves et al., 2003). While in the Mugomo deposit the primary gold is hosted in the metavolcanic rock composed of plagioclase, quartz, biotite, muscovite, epidote, sericite, and calcite as alterations minerals.

The common occurrence of sulfides and gold particularly associated with quartz, quartz-carbonate, and chlorite veins at the Chifumbazi deposit indicates that these sheared rocks may be important perspective guides for vein systems in the northern part of Tete province. Similar structural orientations among foliation and ore veins (Figure. 13b) are evidence of contemporaneous formation, suggesting an ore-forming hydrothermal system.

The Chifumbazi prospect is dominated by NE-SW and N-S trending structures and gold mineralization is associated with these structures. The identified structures acted as fluid pathways for hydrothermal fluids that contemporaneously altered the wall rocks and lead to gold mineralization.

Orogenic gold at the Chifumbazi prospect has some common characteristics: (i) strong structural control involving faults and shear zones, (ii) large veins and vein arrays, and (iii) proximal sericite-chlorite-carbonate alterations. The ore is primarily related to quartz ore in veins that contain sulfides and gold.

Both Mugomo and Chifumbazi show the relationship between hydrothermal alteration zones. However, the Chifumbazi deposit is related to brittle shear deformation during the ore formation, while the Mugomo deposit is related to regional metasomatism.

## **7. REFERENCES**

- Alessio, B.I., Collins, A.S., Siegfried, P., Glorie, S., De Waele, B., Payne, J., Archibald, D.B (2018). Neoproterozoic tectonic geography of the South-east Congo craton Zambia as deduced from the age and composition of detrital zircons. Research paper pp 2-4
- Barnes, H.L., (1997). Geochemistry of hydrothermal ore deposit. Third edition, John Wiley & sons, Inc., New York
- Benning, L. & Seward, T. (1996) Hydrosulfide complexing of Au (I) in hydrothermal solutions from 150–400 C and 500–1500 bar. *Geochimica et Cosmochimica Acta*, 60, 1849–1871.
- Bingen, B., Jacobs, J., Viola, G., Henderson, I.H.C., Skara, Ø., Boyd, R., Thomas, R. J., Solli, A., Key, R. M., Daudi, E.X.F. (2009). Geochronology of the Precambrian crust in

the Mozambique Belt in NE Mozambique and implications for Gondwana assembly. *Precambrian Research*, 170, pp 231-255.

Bodnar, R. (1983) A method of calculating fluid inclusion volume based on vapor bubble diameters and P-V-T-X properties of inclusion fluid. *Economic Geology*, 78, 535–542.

Bodnar, R.J. (2003) Introduction to aqueous electrolyte fluid inclusions. In: Samson, I., Anderson, A. & Marshall, D. (Eds.) *Fluid inclusions: analysis and interpretation mineralogical Association of Canada 2003, short course series, Vol. 32*. Quebec, Canada: Mineralogical Association of Canada, pp. 81–100.

Brekke, H., Furnes, H., Nordås, J. & Hertogen, J. (1984) Lower Palaeozoic convergent plate margin volcanism on Bømlo, SW Norway, and its bearing on the tectonic environments of the Norwegian Caledonides. *Journal of the Geological Society*, 141, 1015–1032. Available from: <https://doi.org/10.1144/gsjgs.141.6.1015>

Brouxel, M. & Lapierre, H. (1988) Geochemical study of an early Paleozoic Island-arc-back-arc basin system. Part 1: the trinity ophiolite (northern California). *Geological Society of America Bulletin*, 100, 1111–1119.

Bryndzia, L. T and Scott, S. D. (1987). Application of Chlorite-Sulfide-Oxide Equilibria to Metamorphosed Massive Sulfide Ores, Snow Lake Area, Manitoba. *Economic Geology*, Vol.82, pp 963-970.

Chai, P., Hou, Z., Zhang, Z. (2017). Geology, Fluid inclusion and stable isotope constraints on the fluid evolution and resource potential of the Xiadian gold deposit, Jiaodong Peninsula. *Original Article. Resource Geology* Vol. 67, No. 3, pp 341-359.

Chai, P., Sun, J. G., Hou, Z., Xing, S. W and Wang, Z. Y. (2016a). Geological, fluid inclusion, H-O-S-Pb isotope, and Ar-Ar geochronology constraints on the genesis of the Nancha gold deposit, southern Jilin Province, northeast China. *Ore Geology. Rev.*, 72, 1053-1071.

Chiaradia, Massimo, (2020). Gold endowments of porphyry deposits controlled by precipitation efficiency. Article number: 248.

- Ciesielczuck, J. (2012). Chlorite of hydrothermal origin in the Strzelin and Borów granites (Fore-Sudetic Block, Poland). *Geological Quarterly*, 56, 333-344.
- Cossa, E.P.F., Agangi, A., Takahashi, R., Manalo, P., Imai, A. & Manjate, V. (2023) Geology, geochemistry, and genesis of gold mineralization in the Chifumbazi deposit of the Tete Province, Irumide Belt, Mozambique. *Resource Geology*, 73(1), e12308. Available from: <https://doi.org/10.1111/rge.12308>
- Daniel I. Ibraimo (2005). Geoscience data integration for classifying geological units in Tete province, Mozambique. Unpublished report.
- Deering C. D., Cole J. W. and Vogel T. A. (2011). Extraction of crystal-poor rhyolite from a hornblende-bearing intermediate mush: a case study of the caldera-forming Matahina eruption, Okataina volcanic complex. *Contributions to Mineralogy and Petrology* volume 161, pages 129–151.
- Deng, Y., Yuan, F., Zhou, T., Xu, C., Zhang, D., & Guo, X. (2015). Geochemical characteristics and tectonic setting of the Tuerkubantao mafic-ultramafic intrusion in West Junggar, Xinjiang, China. *Geoscience Frontiers*, 6(2), 141-152. <https://doi.org/10.1016/j.gsf.2013.10.003>
- De Waele, B., Johnson S.P., Pisarevsky S.A., (2007). Paleoproterozoic to Neoproterozoic growth and evolution of the Eastern Congo craton: Its role in the Rodinia puzzle. Article in *Precambrian Research*.
- De Waele, B., Kampunzu, A.B., Mapani, B.S. E, and Tembo, F. (2006). The Mesoproterozoic Irumide Belt of Zambia. *Journal of African Earth Sciences*, Volume 47, Issues 1-2, PP 54-65.
- De Waele, B., Liegeon. J.P., Alexander, A.N., and Tembo, F. (2006). Isotopic and geochemical evidence of Proterozoic episodic crustal reworking within the Irumide Belt of south-central Africa, the Southern metacratonic boundary of Archaen Bangweulu *Precambrian Research*. PP 148, 225-256.
- De Waele, B., Tembo, F. and Wingate M.T.D (2014). A Review of the geochronology of the Irumide Belt, Zambia. Article

De Waele, B., Tembo, F. and Wingate, M.T.D. (2001). A review of the geochronology of the Irumide Belt, Zambia. Article.

Direcção Nacional de Geologia (DNG), ~ Maputo, 382p. Hannington, M. & Scott, S. (1989) Sulfidation equilibria as guides to gold mineralization in volcanogenic massive sulfides; evidence from sulfide mineralogy and the composition of sphalerite.

Ferry, J.M. (1979). Reaction Mechanisms, Physical Conditions, and Mass Transfer During Hydrothermal Alteration of Mica and Feldspar in Granitic Rocks From South-Central Maine, USA. *Contributions to Mineralogy and Petrology*, 68, 125-139.

Fichter, L. S. (2000). Metamorphic rocks. Barrovian metamorphism, and metamorphic grade. Department of Geology and Environmental Science. James Madison University, Harrisonburg, Virginia 22807.

Fritz, H., Abdelsalam, M., Ali, K. A., Bingen, B., Collins, A. S., Fowler, A. R., Ghebread, W., Hauzenberger, C. A., Johnson, P. R., Kusky, T. M., Macey, P., Muhongo, S., Stern, R. J., and Viola, G. (2013). Orogen styles in the East African orogen: A review of the Neoproterozoic to Cambrian tectonic evolution. Volume 86, PP 65-106.

Goldfarb, R. & Groves, D. (2015) Orogenic gold: common or evolving fluid and metal sources through time. *Lithos*, 233, 2–26. Available from: <https://doi.org/10.1016/j.lithos.2015.07.011>

Goldfarb, R.J., Baker, T., Dube, B., Groves, D.I., Hart, C.J.R. & Gosselin, P. (2005) Distribution, character and genesis of gold deposits in metamorphic terranes. In: Hedenquist, J.W., Thompson, J.F.H., Goldfarb, R.J. & Richards, J.P. (Eds.) *Economic geology 100th anniversary volume*. Quebec, Canada: *Economic Geology*, pp. 407–450.

Grantham, M., Maboko, M. & Englington, B. (2003) A review of the evolution of the Mozambique Belt and implications for the amalgamation and dispersal of Rodinia and Gondwana. *Geological Society, London, Special Publications*, 206, 401–425.

Grantham, M.Y., Maboko, M. and Englington, B.M. (2003). Proterozoic East Gondwana: supercontinent Assembly and breakup. *Gondwana Institute for Geology and Environment*,

Japan Institute of Fundamental Studies, Sri Lanka, Geological Society Special Publications.

Groves, D.I., Goldfarb, R.J., François, R.F. & Hart, C.J.R. (2003) Gold deposits in metamorphic belts: overview of current understanding, outstanding problems, future research, and exploration significance. *Economic Geology*, 98, 1–29.

Groves, D.I., Goldfarb, R.J., Gebre-Mariam, M., Hagemann, S. & Robert, F. (1998) Orogenic gold deposits: a proposed classification in the context of their crustal distribution and relationship to other gold deposit types. *Ore Geology Reviews*, 13, 7–28.

Groves, D.I., Goldfarb, R.J., Mariam, M.G., Hagemann, S.G, and Robert, F, (1997). Orogenic gold deposits: A proposal classification in the context of their crustal distribution and relationship to other gold deposit. Pp 8.

GTK Consortium. (2006) Geology of Degree Sheets Inhamambo, Maluwa, Chifunde, Zumbo, Fíngoè- Mâgoè, Songo, Cazula, and Z obuè, Mozambique. Map Explanation, 4: Sheets 1430– 1432 and 1530–1534.

Hedenquist G.W, Lowenstern J.B., (1994). The role of magma in the formation of hydrothermal ore deposits. *Nature*, 370, pp 519-527

Hedenquist, J. W., Arribas, A., Urien, E.G., (2000). Exploration for epithermal gold deposits. *SEG Reviews*, chapter 7, Vol. 13, p. 245-277.

Johnson, C., Affolter, M.D., Inkenbrandt, P., Mosher, C. (2012). An introduction to geology. *Libretexts*, 491.

Johnson, S. P., Rivers, T., and De Waele, B. (2005). A review of the Mesoproterozoic to early Paleozoic magmatic and tectonothermal history of south- central Africa: implications for Rodinia and Gondwana. *Journal of the geological society London*, Volume 162. PP 433-450.

Johnson, S.P., de Waele, B., Tembo, F., Katango, C., Tani, K., Chang, Q., Iizuka, T. and Dunkley, D. (2007) Geochemistry, Geochronology and Isotopic Evolution of the Chewore–Rufunsa Terrane, Southern Irumide Belt: a Mesoproterozoic Continental Margin Arc. *Journal of Petrology*, Vol. 48, pp 1411-1441

- Kerkhof, A.M. V. D, and Hein, F. (2000). Fluid inclusion petrograph.
- Kerrick, R., Goldfarb, R., Groves, D.I., Garwin, S.L, (2000). The geodynamics of world-class gold deposits: Characteristics, space-time distribution and origins. *Reviews in Economic Geology*, Article, volume 13.
- Kesler, S.E., Chryssoulis, S.L., Simon, G (2002). Gold in porphyry copper deposits: its abundance and fate. *Ore geology reviews*. Volume 21, Issues 1-2, pages 103 – 124.
- Kirkemo, H., Newman, W. L., Ashley, R. P. (2017). The geology of gold. Article
- Koglin, N., Frimmel, H.E., Minter W.E.L., Brätz, H. (2009). Trace-element characteristics of different pyrite types in Mesoarchean to Paleoproterozoic placer deposits. *Mineralium Deposita* 45, article, 259-280 (2010).
- Korkiakoski, E. (2008). Geochemical surveys in Mozambique: a data compilation project. Geological survey of Finland, special paper 48, 263-287.
- Lächelt, S. (2004). Geological and Mineral Resources of Mozambique; Ministério de Recursos Minerais e Energia de Moçambique. Internal report
- Lehto, T., and Goncalves, R, (2008). Mineral Resources potential in Mozambique. Page 319
- Macey, P.H., Thomas, R.J., Grantham, G.H., Ingram, B.A., Jacobs, J., Armstrong, R.A., Roberts, M.P., Bingen, B., Hollick, L., deKock, G.S., Viola, G., Bauer, W., Gonzales, E., Bjerkgård, T., Hendersongm, I.H.C., Sandstadg, J.S., Cronwrightc, M.S., Harley, S., Solli, A., Nordgulen, Ø., Motuza, G., Daudi, E. and Manhic, V. (2010). Mesoproterozoic geology of the Nampula Block, northern Mozambique: tracing fragments of Mesoproterozoic crust in the heart of Gondwana *Precambrian Research*, 182 (2010), pp. 124-148.
- Mäkitie H., Matti I. L., Manninen T., Marques J.M., Cune, G and Mavie, H (2008). Petrography and geochemistry of granitoid rocks in the northern part of Tete province. PP 168-169.

- Manalo, P. C., Imai, A., Subang, L., de los Santos, M., Yanagi, K., Takahashi, R. and Blamey, N. (2018) Mineralization of the northwest quartz-pyrite-gold (QPG) veins: Implications for multiple mineralization events in Lepanto, Mankayan Mineral District, northern Luzon, Philippines. *Economic Geology*, 113, 1609–1626.
- Mänttari, I. 2008. Mesoarchaeon to Lower Jurassic U-Pb and Sm-Nd ages from NW Mozambique. Geological Survey of Finland, Special paper 48, 81- 119.
- Ministério da Administração Estatal – MAE (2005). Perfil do distrito de Chifunde Província de Tete. Report, pp 2-3.
- Mtabazi, E. G., Boniface, N., and Andresen, A. (2019). Geochronological characterization of a transition zone between the Mozambique Belt and Unango-Marupa complex in SE Tanzania. Paper, pp 134-153.
- Nopeia, M., Mondlane, S., Takahashi, R., Jamal, D., Abdulgani, I. and Baptista, I. (2022) An integrated geoscience approach to effective formalization of artisanal mining in Mozambique: A case study of Namuno District, northeastern Mozambique. *The Extractive Industries and Society*, 101098. <https://doi.org/10.1016/j.exis.2022.101098>.
- Nopeia, M., Takahashi, R., Imai, A., Jamal, D. and Agangi, A. (2021) Geological and geochemical characterization of the Nanlia and Makorongo gold prospects, Mozambique Belt, northeastern Mozambique. *Ore Geology Reviews*, 135, 104195. <https://doi.org/10.1016/j.oregeorev.2021.104195>.
- Ohmoto, H. (1986). Stable isotope geochemistry of ore deposits. *Reviews in Mineralogy*, Chapter 14, 491-560.
- Ortega, L. (2017). Fundamentals of fluid inclusions studies, Short course (Akita University, 2017).
- Pearce, J. (1996). Sources and settings of granitic rocks, Article in *Episodes* 19 (4), pp 120-125.
- Pearce, J. A., & Cann, J. (1973). Tectonic setting of basic volcanic rocks determined using trace element analyses. *Earth and Planetary Science Letters*, 19(2), 290– 300



- Pearce, J.A. and Norry, M.J. (1979). Petrogenetic Implications of Ti, Zr, Y, and Nb Variations in Intrusive Rocks. *Contributions to Mineralogy and Petrology*, 69, 33-47. <http://dx.doi.org/10.1007/BF00375192>
- Pearce, J.A., 1982, Trace element characteristics of lavas from destructive plate boundaries, in Thrope, R.S., eds., *Andesites*: New York, John Wiley and Sons, 528–548 p.
- Pearson, T. N. and Viljoen, M.J. (1986). Antimony mineralization in the Murchison greenstone Belt an overview. *Mineral deposit of Southern Africa*. PP 316-317
- Pekkala, Y., Lehto, T., and Matti, I. L (2008). Introduction to GTK Projects in Mozambique. Article in *Special Paper - Geological Survey of Finland*.
- Phillips, G.N. and Powell, R. (2010) Formation of gold deposits: A metamorphic devolatilization model. *Journal of Metamorphic Geology*, 28, 689-718. <https://doi.org/10.1111/j.1525-1314.2010.00887.x>.
- Pirajno, Franco, (2009). Hydrothermal process and mineral systems. *Geological Survey of Western Australia*, Perth, WA, Australia, chapter 5, 355 – 516p.
- Regnolds, G. (1994). Fluid inclusion petrograph, Chapter 6.
- Reich, M., Kesler, S.E. and Utsunomiya, S. (2005) Solubility of gold in arsenian pyrite. *Geochimica et Cosmochimica Acta*, 69, 2781-2796.
- Ridley, J.R. and Diamond, L.W. (2000) Fluid chemistry of lode-gold deposits and implications for genetic models. *Society of Economic Geologists*, 13, 141-162.
- Roedder, E. (1984) Fluid Inclusions. *Reviews in Mineralogy* 12, Mineralogical Society of America, 644 p.
- Rogers, J. J., Unrug, R. and Sultan, M. (1995) Tectonic assembly of Gondwana. *Journal of*
- Rollinson, H. (1993). *Using geochemical data evaluation, interpretation*. Singapore. Ongman.

- Rottier, B. and Casanova, V. (2020) Trace element composition of quartz from porphyry systems: a tracer of the mineralization fluid evolution. *Mineralium Deposita*, 56, 843-862. <https://doi.org/10.1007/s00126-020-01009-0>.
- Rusk, B. (2012) Cathodoluminescent textures and trace elements in hydrothermal quartz. In *Quartz: Deposits, Mineralogy and Analytics*. Springer, Berlin, Heidelberg, 307-329. DOI: 10.1007/978-3-6442-22161-3\_14.
- Rusk, B., Lowers, H. and Reed, M. (2008) Trace elements in hydrothermal quartz: relationships to cathodoluminescence textures and insights into vein formation. *Geological Society of America* 36, 547–550. <https://doi.org/10.1130/G24580A.1>
- Sarafian, E., Evans, R.L., Salam, M.G.A., Atekwana, E. A., Elsenbeck, J.R., Jones, A.G., and Chikambwe, E.M (2017). Imaging Precambrian lithospheric Structure in Zambia using Electromagnetic methods. Article paper.
- Seal II, R. R. (2006). Sulfur Isotope Geochemistry of Sulfide minerals.
- Seward, T. M. (1973) Thio complex of gold and the transfer of gold in hydrothermal ore solutions. *Geochimica et Cosmochimica Acta*, 53, 379–399.
- Shao, Y.J., Wang, W.S., Liu Q.Q., Zhang, Y. (2018). Trace Element Analysis of Pyrite from the Zhengchong Gold Deposit, Northeast Hunan Province, China: Implications for the Ore-Forming Process. Paper, pp 8-17.
- Sillitoe, R. H. (2010). Porphyry copper systems. *Economic Geology*. Research article 105 (1), pp. 3–41.
- Simon, J., De Waele, B., and Liyungu, A.K. (2006). U-Pb Shrimp geochronology of granitoid rocks in eastern Zambia: terrane subdivision of the Mesoproterozoic southern Irumide Belt. Article in *Tectonics* 25:TC6004
- Sterk, R., Gazley, M.F., Wood, M. P., Collins, S.C. and Collis, G. (2018) Maximising the value of PorTable XRF data in exploration: An example from Marirongoe, Mozambique. *Geochemistry: Exploration, Environment, Analysis*, 18, 142 – 154, article

Sun, S. and McDonough, W. (1989). Chemical and isotopic systematics of ocean basalts: implications for mantle composition and processes, in magmatism in the ocean basins. Geological Society, London, Special Publications, 42, 313-345. DOI:10.1144/GSL.SP.1989.042.01.19

Sun, Z., Wang, J., Wang, Y., Zhang, Y. and Zhao, L. (2021). Multistage hydrothermal quartz veins record the ore-forming fluid evolution in the Meiling Cu–Zn (Au) deposit, NW China. Ore Geology Reviews, 131, 104002. <https://doi.org/10.1016/j.oregeorev.2021.104002>.

Sverine, G. (1978). Relatório sobre os trabalhos de prospecção de ouro na provincial de Tete (distrito de Macanga) realizados pela brigada de investigação complexa (contrato 55-036/11900). Unpublished, internal report.

Takahashi, R., Müller, A., Matsueda, H., Okrugin, V.M., Ono, S., van den Kerkhof, A., Kronz, A. and Andreeva, E.D. (2008). Cathodoluminescence and trace elements in quartz: Clues to metal precipitation mechanisms at the Asachinskoe gold deposit in Kamchatka. In Origin and Evolution of Natural Diversity: Proceedings of the International Symposium, 175–184.

Takenouchi and Kennedy (1965). The solubility of carbon dioxide in NaCl solutions at high temperatures and pressures. Amer. J. Sci., 263, 445–454.

Thode, H.G. (1970). Sulfur Isotope geochemistry and fractionation between coexisting sulfide minerals. Mineral Society of America. Spec. Paper 3, 133-144.

Ueki, K., Hino, H., Kuwatani, T. (2017). Geochemical discrimination and characteristics of magmatic tectonic settings: A machine-learning-based approach. Geochemistry, Geophysics, Geosystems, research article. Pp 1327- 1347.

Wang, Z., Chen, B., Yan, X., Li, s. (2018). Characteristics of hydrothermal chlorite from the Niujuan Ag-Au-Pb-Zn deposit in the north margin of NCC and implications for exploration tools for ore deposits. Ore Geology Reviews 101, Elsevier, article, 398-412.

Westerhof, A.B.P., Mäkitie H., Matti I. L., Manninen T., Pekkala, Y., Gustafsson, B. and Tahon, A (2008). The Tete-chipata Belt: A new multiple terrane element from western

Mozambique and Southern Zambia. Geological Survey of Finland, Special Paper 48, 145-166.

Westerhof, A.B.P., Tahon, A., Lehto, T. (2008). Igneous and tectonic setting of the allochthonous Tete gabbro-anorthosite Suite, Mozambique. Geological survey of Finland.

White, N. C. and Hedenquist, J. W; (1995). Epithermal gold deposits: styles, characteristics and exploration. Published in SEG Newsletter, No. 23, pp. 1, 9-13.

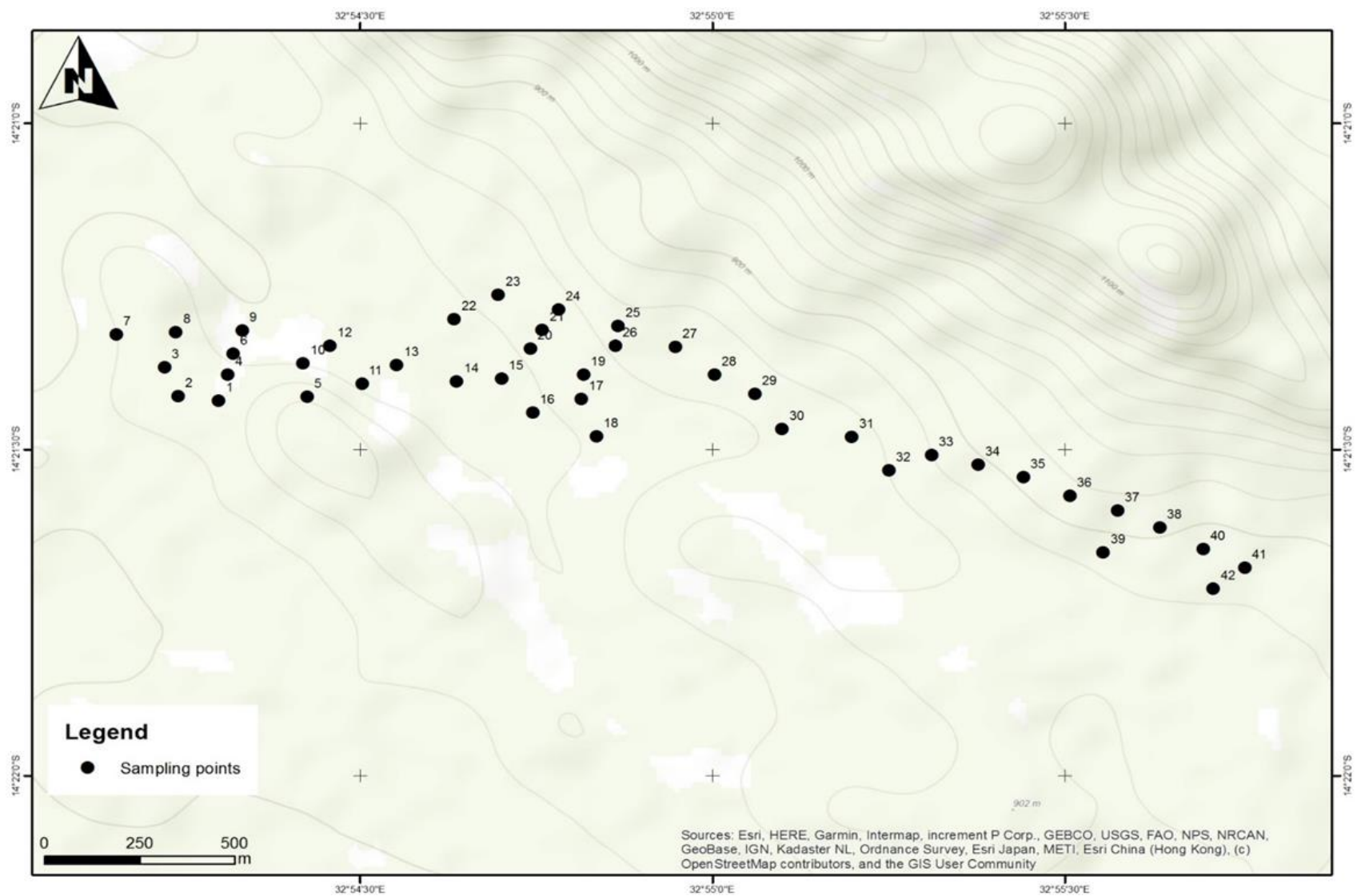
Wilkinson, J. J., Chang, Z., Cooke, D. R., Baker, M. J., Wilkinson, C. C., Inglis, S., Chen, H., & Bruce Gemmell, J. (2015). The chlorite proximator: A new tool for detecting porphyry ore deposits. *Journal of Geochemical Exploration*, 152, 10-26.

Xia, L., & Li, X. (2019). Basalt geochemistry as a diagnostic indicator of tectonic setting. *Gondwana Research*, 65, 43-67. <https://doi.org/10.1016/j.gr.2018.08.006>



Yavuz, F., Kumral, M., Karakaya, N., Karakaya, M. Ç., & Yıldırım, D. K. (2015). A Windows program for chlorite calculation and classification. *Computers & Geosciences*, 81, 101-113.

## **8. APPENDICES**

**Appendix 1.** Sample collection, field observation and host rock characteristics of the Mugomo deposit



**APPENDIX 1.1.** Field observation and host rock characteristics of the Mugomo deposit

<p><b>Sample species:</b> metavolcanic rock (<b>Sample name:</b> EC180317-02, <b>Primary key:</b> Mg 17-02). Location: Mugomo, Area: Northern Tete, <b>Country:</b> Mozambique, <b>Longitude (S):</b> – 14.22962, <b>Latitude (E):</b> 32. 59201, <b>Type of sample:</b> metamorphic rock, <b>Piece:</b>1, <b>Year of collection:</b> 2018, <b>Data input:</b> 17_March_2018. <b>Note:</b> Metavolcanic rock with disseminated sulfides.</p>		<p><b>Sample species:</b> biotite- schist (<b>Sample name:</b> EC180317-09, <b>Primary key:</b> Mg 17-09). Location: Mugomo, Area: Northern Tete, <b>Country:</b> Mozambique, <b>Longitude (S):</b> – 14.22962, <b>Latitude (E):</b> 32. 59201, <b>Type of sample:</b> Schist. <b>Piece:</b>1, <b>Year of collection:</b> 2018, <b>Data input:</b> 17_March_2018</p> <p><b>Note:</b> Biotite-schist.</p>	
			
<p>Analysis and preparation (0: none, 1: exist)</p>		<p>Analysis and preparation (0: none, 1: exist)</p>	
Bulk chemical composition:1	XRD analysis: 0	Bulk chemical composition:0	XRD analysis: 0
Polish section: 1	Sulfur isotope:1	Polish section: 0	Sulfur isotope:0
Thin section: 1	EPMA analysis: 1	Thin section: 1	EPMA analysis: 0
Fluid inclusion analysis:0	Dating: 0	Fluid inclusion analysis: 0	Dating: 0

**Sample species:** metavolcanic rock (**Sample name:** EC180317-01, **Primary key:** Mg 17-06). Location: Mugomo, Area: Northern Tete, **Country:** Mozambique, **Longitude (S):** -14.22962, **Latitude (E):** 32. 59201 **Type of sample:** metamorphic rock, **Piece:**1, **Year of collection:** 2018, **Data input:** 17\_March\_2018. **Note:** Fine grain metavolcanic rock crosscut by epidote vein.



Analysis and preparation (0: none, 1: exist)	
Bulk chemical composition:1	XRD analysis: 1
Polish section: 0	Sulfur isotope:0
Thin section: 1	EPMA analysis: 0
Fluid inclusion analysis: 0	Dating: 0

**Sample species:** metavolcanic rock (**Sample name:** EC180315-02, **Primary key:** Mg 15-02). Location: Mugomo, Area: Northern Tete, **Country:** Mozambique, **Longitude (S):** -14.22962, **Latitude (E):** 32. 59201, **Type of sample:** metamorphic rock, **Piece:**1, **Year of collection:** 2018, **Data input:** 15\_March\_2018.

**Note:** Silicified metavolcanic rock crosscut by crosscut by epidote vein.



Analysis and preparation (0: none, 1: exist)	
Bulk chemical composition:1	XRD analysis: 1
Polish section: 0	Sulfur isotope:0
Thin section: 1	EPMA analysis: 1
Fluid inclusion analysis: 0	Dating: 0



**Sample species:** metavolcanic rock  
**(Sample name:** EC180316-02, **Primary key:** Mg 16-02). Location: Mugomo, Area: Northern Tete, **Country:** Mozambique, **Longitude (S):** – 14.22962, **Latitude (E):** 32. 59201, **Type of sample:** metamorphic rock, **Piece:**1, **Year of collection:** 2018, **Data input:** 16\_March\_2018. **Note:** massive sulfide disseminated in the metavolcanic rock



Analysis and preparation (0: none, 1: exist)	
Bulk chemical composition:1	XRD analysis: 0
Polish section: 1	Sulfur isotope:1
Thin section: 1	EPMA analysis: 0
Fluid inclusion analysis: 0	Dating: 0

**Sample species:** epidote quartz vein  
**(Sample name:** EC180316-04, **Primary key:** Mg 16-04). Location: Mugomo, Area: Northern Tete, **Country:** Mozambique, **Longitude (S):** – 14.22962, **Latitude (E):** 32. 59201, **Type of sample:** vein, **Piece:**1, **Year of collection:** 2018, **Data input:** 16\_March\_2018.

**Note:** Epidote quartz vein



Analysis and preparation (0: none, 1: exist)	
Bulk chemical composition:1	XRD analysis: 0
Polish section: 0	Sulfur isotope:0
Thin section: 0	EPMA analysis:0
Fluid inclusion analysis: 1	Dating: 0

**Sample species:** metavolcanic rock (**Sample name:** EC180317-23, **Primary key:** Mg 17-23). Location: Mugomo, Area: Northern Tete, **Country:** Mozambique, **Longitude (S):** – 14.22962, **Latitude (E):** 32. 59201, **Type of sample:** metamorphic rock, **Piece:**1, **Year of collection:** 2018, **Data input:** 17\_March\_2018. **Note:** sulfides disseminated in the metavolcanic rock



Analysis and preparation (0: none, 1: exist)	
Bulk chemical composition:1	XRD analysis: 0
Polish section: 1	Sulfur isotope:1
Thin section: 1	EPMA analysis: 1
Fluid inclusion analysis: 0	Dating: 0

**Sample species:** metavolcanic rock (**Sample name:** EC180317-16, **Primary key:** Mg 17-16). Location: Mugomo, Area: Northern Tete, **Country:** Mozambique, **Longitude (S):** – 14.22962, **Latitude (E):** 32. 59201, **Type of sample:** metamorphic rock, **Piece:**1, **Year of collection:** 2018, **Data input:** 17\_March\_2018 **Note:** sulfides disseminated in the metavolcanic rock



Analysis and preparation (0: none, 1: exist)	
Bulk chemical composition:1	XRD analysis: 0
Polish section: 1	Sulfur isotope:0
Thin section: 0	EPMA analysis: 1
Fluid inclusion analysis: 0	Dating: 0

**Sample species:** metavolcanic rock (**Sample name:** EC180316-09, **Primary key:** Mg 16-09). Location: Mugomo, Area: Northern Tete, **Country:** Mozambique, **Longitude (S):** - 14.22962, **Latitude (E):** 32. 59201, **Type of sample:** metamorphic rock, **Piece:**1, **Year of collection:** 2018, **Data input:** 16\_March\_2018. Note: sulfides disseminated in the silicified rock.



Analysis and preparation (0: none, 1: exist)	
Bulk chemical composition:1	XRD analysis: 0
Polish section: 1	Sulfur isotope:1
Thin section: 1	EPMA analysis: 1
Fluid inclusion analysis: 0	Dating: 0

**Sample species:** silicified rock (**Sample name:** EC180321-13, **Primary key:** Mg 21-13). Location: Mugomo, Area: Northern Tete, **Country:** Mozambique, **Longitude (S):** - 14.22962, **Latitude (E):** 32. 59201, **Type of sample:** metamorphic rock, **Piece:**1, **Year of collection:** 2018, **Data input:** 21\_March\_2018. **Note:** altered metavolcanic rock



Analysis and preparation (0: none, 1: exist)	
Bulk chemical composition:1	XRD analysis: 0
Polish section: 0	Sulfur isotope:0
Thin section: 0	EPMA analysis: 0
Fluid inclusion analysis: 0	Dating: 0

**Sample species:** silicified rock (**Sample name:** EC180321-13, **Primary key:** Mg 21-13). Location: Mugomo, Area: Northern Tete, **Country:** Mozambique, **Longitude (S):** - 14.22962, **Latitude (E):** 32. 59201, **Type of sample:** metamorphic rock, **Piece:**1, **Year of collection:** 2018, **Data input:** 21\_March\_2018



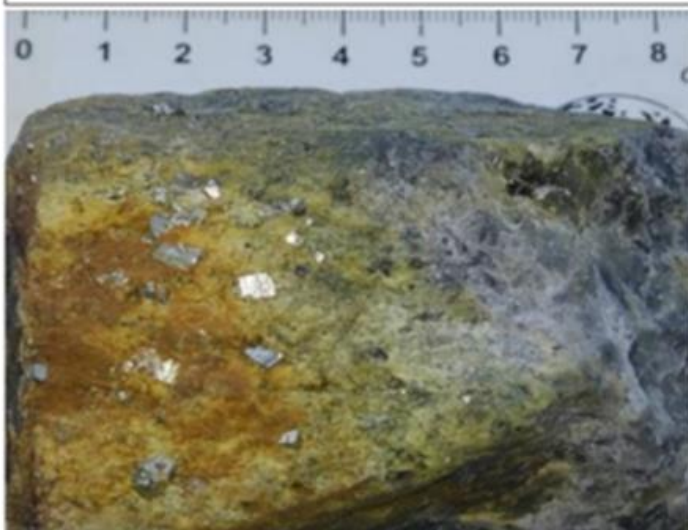
Analysis and preparation (0: none, 1: exist)	
Bulk chemical composition:1	XRD analysis: 0
Polish section: 0	Sulfur isotope:0
Thin section: 0	EPMA analysis: 0
Fluid inclusion analysis: 1	Dating: 0

**Sample species:** metavolcanic rock (**Sample name:** EC180321-08, **Primary key:** Mg 21-08). Location: Mugomo, Area: Northern Tete, **Country:** Mozambique, **Longitude (S):** - 14.22962, **Latitude (E):** 32. 59201, **Type of sample:** metamorphic rock, **Piece:**1, **Year of collection:** 2018, **Data input:** 21 March\_2018



Analysis and preparation (0: none, 1: exist)	
Bulk chemical composition:1	XRD analysis: 0
Polish section: 0	Sulfur isotope:0
Thin section: 0	EPMA analysis:0
Fluid inclusion analysis: 0	Dating: 0

**Sample species:** silicified roc (**Sample name:** EC180321-02, **Primary key:** Mg 21-05). Location: Mugomo, Area: Northern Tete, **Country:** Mozambique, **Longitude (S):** -14.22962, **Latitude (E):** 32. 59201, **Type of sample:** metamorphic rock, **Piece:**1, **Year of collection:** 2018, **Data input:** 21March\_2018. **Note:** altered silicified rock with disseminated sulfides



Analysis and preparation (0: none, 1: exist)

Bulk chemical composition:1	XRD analysis: 0
Polish section:1	Sulfur isotope:0
Thin section:1	EPMA analysis: 0
Fluid inclusion analysis: 0	Dating: 0

**Sample species:** metavolcanic rock (**Sample name:** EC180321-13, **Primary key:** Mg 21-13). Location: Mugomo, Area: Northern Tete, **Country:** Mozambique, **Longitude (S):** -14.22962, **Latitude (E):** 32. 59201, **Type of sample:** metamorphic rock, **Piece:**1, **Year of collection:** 2018, **Data input:** 21March\_2018. **Note:** metavolcanic rock crosscut by quartz vein.



Analysis and preparation (0: none, 1: exist)

Bulk chemical composition:1	XRD analysis: 0
Polish section:0	Sulfur isotope:0
Thin section: 1	EPMA analysis: 0
Fluid inclusion analysis: 1	Dating: 0

**Sample species:** silicified roc (**Sample name:** EC180321-02, **Primary key:** Mg 21-02). Location: Mugomo, Area: Northern Tete, **Country:** Mozambique, **Longitude (S):** -14.22962, **Latitude (E):** 32. 59201, **Type of sample:** metamorphic rock, **Piece:**1, **Year of collection:** 2018, **Data input:** 21March\_2018. **Note:** quartzite crosscut by epidote vein



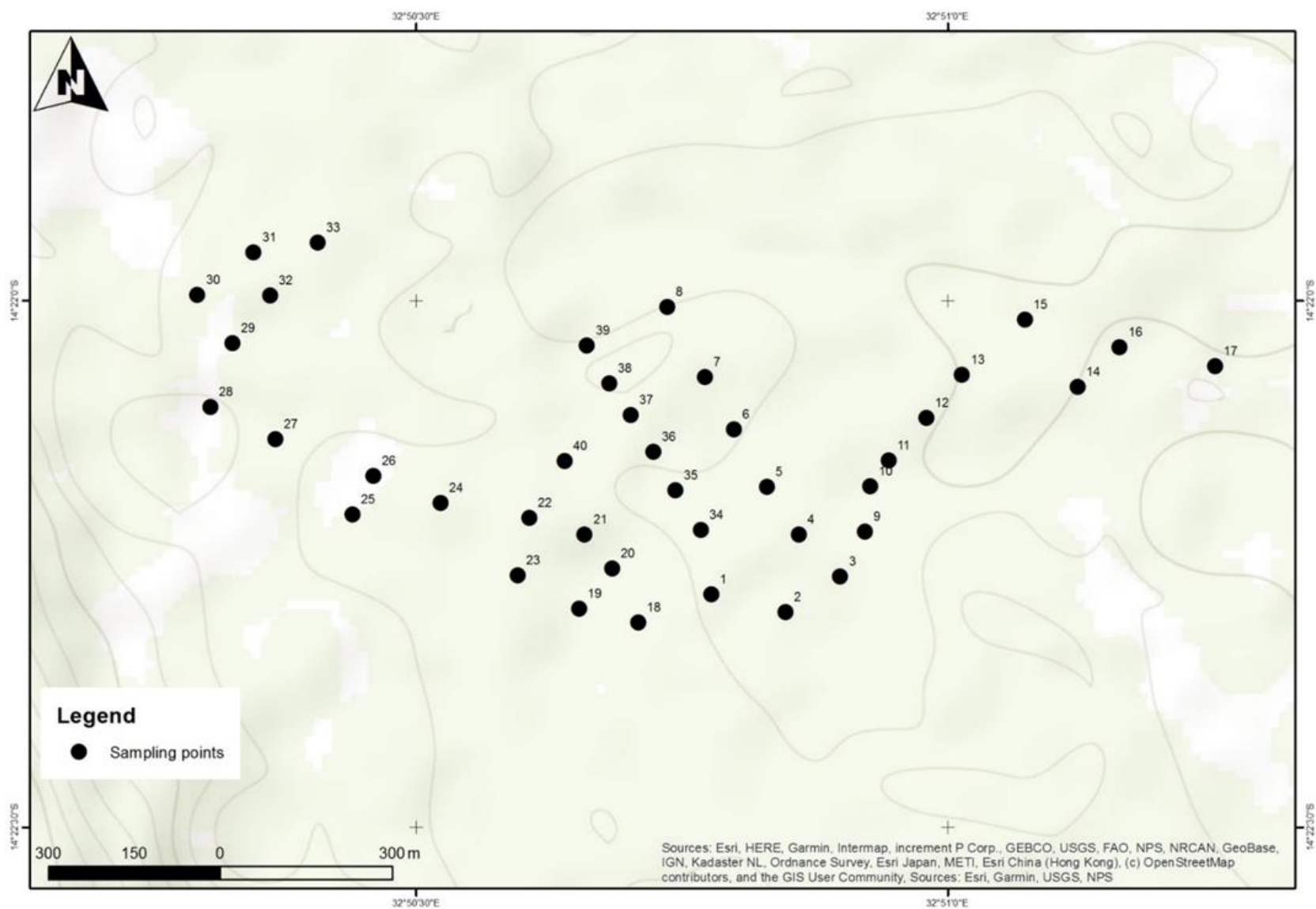
Analysis and preparation (0: none, 1: exist)	
Bulk chemical composition:1	XRD analysis: 0
Polish section:0	Sulfur isotope:0
Thin section: 1	EPMA analysis: 0
Fluid inclusion analysis: 1	Dating: 0

**Sample species:** silicified roc (**Sample name:** EC180321-02, **Primary key:** Mg 17-15). Location: Mugomo, Area: Northern Tete, **Country:** Mozambique, **Longitude (S):** -14.22962, **Latitude (E):** 32. 59201, **Type of sample:** metamorphic rock, **Piece:**1, **Year of collection:** 2018, **Data input:** 21March\_2018. **Note:** quartzite with disseminated sulfides



Analysis and preparation (0: none, 1: exist)	
Bulk chemical composition:1	XRD analysis: 0
Polish section:0	Sulfur isotope:0
Thin section: 1	EPMA analysis: 0
Fluid inclusion analysis: 1	Dating: 0

**Appendix 1.2.** Field observation and host rock characteristics of the Chifumbazi deposit



## APPENDIX 1.2.1 Field observation and host rock characteristics of the Chifumbazi deposit

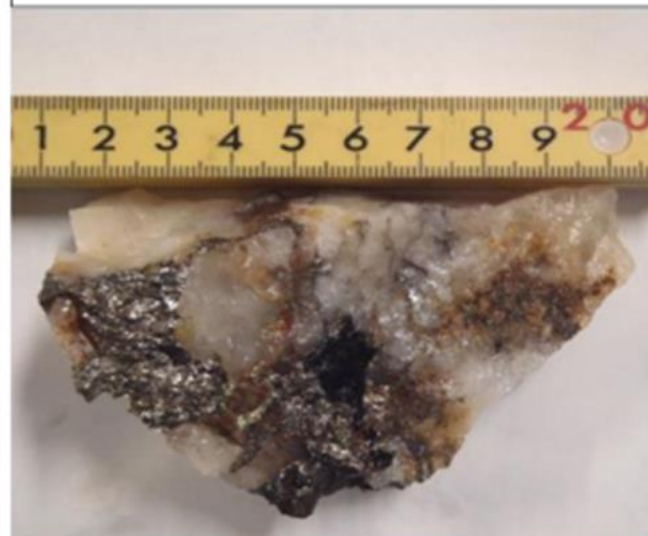
**Sample species:** quartz-mica-schist  
**(Sample name:** EC180320-08, **Primary key:** Cf-08). **Location:** Chifumbazi, Area: Northern Tete, **Country:** Mozambique, **Longitude (S):** -14.40127, **Latitude (E):** 33.01325, **Type of sample:** igneous rock, **Piece:**1, **Year of collection:** 2018, **Data input:** 20\_March\_2018. **Note:** quartz-sericite schist crosscut by quartz vein



Analysis and preparation (0: none, 1: exist)

Bulk chemical composition:1	XRD analysis: 0
Polish section:0	Sulfur isotope:0
Thin section: 0	EPMA analysis: 0
Fluid inclusion analysis: 1	Dating: 0

**Sample species:** quartz vein (**Sample name:** EC180320-09, **Primary key:** Cf-09). **Location:** Chifumbazi, Area: Northern Tete, **Country:** Mozambique, **Longitude (S):** -14.40127, **Latitude (E):** 33.01325, **Type of sample:** quartz vein, **Piece:**1, **Year of collection:** 2018, **Data input:** 20\_March\_2018. **Note:** quartz vein with sulfides



Analysis and preparation (0: none, 1: exist)

Bulk chemical composition:1	XRD analysis: 0
Polish section: 0	Sulfur isotope:1
Thin section: 0	EPMA analysis: 0
Fluid inclusion analysis: 0	Dating: 0



**Sample species:** chlorite vein (**Sample name:** EC180320-40, **Primary key:** Cf-40).  
**Location:** Chifumbazi, Area: Northern Tete,  
**Country:** Mozambique, **Longitude (S):** -14.40127, **Latitude (E):** 33.01325, **Type of sample:** vein, **Piece:**1, **Year of collection:** 2018, **Data input:** 20\_March\_2018.  
**Note:** sulfides disseminated in the chlorite and quartz vein.



Analysis and preparation (0: none, 1: exist)

Bulk chemical composition:1	XRD analysis: 0
Polish section:0	Sulfur isotope:1
Thin section: 0	EPMA analysis:1
Fluid inclusion analysis: 1	Dating: 0

**Sample species:** quartz-mica-schist (**Sample name:** EC180320-36, **Primary key:** Cf-36).  
**Location:** Chifumbazi, Area: Northern Tete,  
**Country:** Mozambique, **Longitude (S):** -14.40127, **Latitude (E):** 33.01325, **Type of sample:** igneous rock, **Piece:**1, **Year of collection:** 2018, **Data input:** 20\_March\_2018.

**Note:** quartz-sericite schist



Analysis and preparation (0: none, 1: exist)

Bulk chemical composition:1	XRD analysis: 1
Polish section:	Sulfur isotope:0
Thin section: 1	EPMA analysis: 0
Fluid inclusion analysis: 0	Dating: 0

**Sample species:** quartz-mica-schist  
**(Sample name:** EC180320-09, **Primary key:** Cf-09). **Location:** Chifumbazi, Area: Northern Tete, **Country:** Mozambique, **Longitude (S):** -14.40127, **Latitude (E):** 33.01325, **Type of sample:** igneous rock, **Piece:**1, **Year of collection:** 2018, **Data input:** 20\_March\_2018. **Note:** milky, carbonate quartz and chlorite vein



Analysis and preparation (0: none, 1: exist)	
Bulk chemical composition:1	XRD analysis: 0
Polish section: 0	Sulfur isotope:0
Thin section: 1	EPMA analysis: 0
Fluid inclusion analysis: 0	Dating: 0

**Sample species:** quartz-mica-schist  
**(Sample name:** EC180320-14, **Primary key:** Mg 17-09). **Location:** Chifumbazi, Area: Northern Tete, **Country:** Mozambique, **Longitude (S):** -14.40127, **Latitude (E):** 33.01325, **Type of sample:** igneous rock, **Piece:**1, **Year of collection:** 2018, **Data input:** 20\_March\_2018. **Note:** quartz-sericite schist crosscut by milky and carbonate quartz.



Analysis and preparation (0: none, 1: exist)	
Bulk chemical composition:1	XRD analysis: 0
Polish section: 0	Sulfur isotope:0
Thin section: 1	EPMA analysis:1
Fluid inclusion analysis: 1	Dating: 0

**Sample species:** quartz-mica-schist  
**(Sample name:** EC180320-35, **Primary key:** Cf-35). **Location:** Chifumbazi, **Area:** Northern Tete, **Country:** Mozambique, **Longitude (S):** -14.40127, **Latitude (E):** 33.01325, **Type of sample:** igneous rock, **Piece:**1, **Year of collection:** 2018, **Data input:** 20\_March\_2018. **Note:** quartz-sericite schist with disseminated sulfides



Analysis and preparation (0: none, 1: exist)

Bulk chemical composition:1	XRD analysis:1
Polish section: 0	Sulfur isotope:1
Thin section: 1	EPMA analysis: 0
Fluid inclusion analysis:0	Dating: 0

**Sample species:** gneiss (**Sample name:** EC180320-10, **Primary key:** Cf-10). **Location:** Chifumbazi, **Area:** Northern Tete, **Country:** Mozambique, **Longitude (S):** -14.40127, **Latitude (E):** 33.01325, **Type of sample:** igneous rock, **Piece:**1, **Year of collection:** 2018, **Data input:** 20\_March\_2018. **Note:** foliated gneiss



Analysis and preparation (0: none, 1: exist)

Bulk chemical composition:1	XRD analysis: 1
Polish section: 0	Sulfur isotope:0
Thin section: 1	EPMA analysis: 0
Fluid inclusion analysis: 0	Dating: 0

**Sample species:** quartz vein (**Sample name:** EC180320-40, **Primary key:** Cf-40). **Location:** Chifumbazi, Area: Northern Tete, **Country:** Mozambique, **Longitude (S):** -14.40127, **Latitude (E):** 33.01325, **Type of sample vein,** **Piece:**1, **Year of collection:** 2018, **Data input:** 20\_March\_2018.

**Note:** quartz vein



Analysis and preparation (0: none, 1: exist)	
Bulk chemical composition:1	XRD analysis:0
Polish section: 0	Sulfur isotope:1
Thin section: 1	EPMA analysis: 1
Fluid inclusion analysis:1	Dating: 0

**Sample species:** quartz vein (**Sample name:** EC180320-24, **Primary key:** Cf-28). **Location:** Chifumbazi, Area: Northern Tete, **Country:** Mozambique, **Longitude (S):** -14.40127, **Latitude (E):** 33.01325, **Type of sample:** igneous rock, **Piece:**1, **Year of collection:** 2018, **Data input:** 20\_March\_2018. **Note:** a mixture of clear and quartz- carbonate veins crosscut by chlorite veinlet



Analysis and preparation (0: none, 1: exist)	
Bulk chemical composition:1	XRD analysis:0
Polish section: 0	Sulfur isotope:0
Thin section: 1	EPMA analysis: 0
Fluid inclusion analysis:1	Dating: 0

**Sample species:** quartz-mica-schist (**Sample name:** EC180320-08, **Primary key:** Cf-08). **Location:** Chifumbazi, Area: Northern Tete, **Country:** Mozambique, **Longitude (S):** -14.40127, **Latitude (E):** 33.01325, **Type of sample:** igneous rock, **Piece:**1, **Year of collection:** 2018, **Data input:** 20\_March\_2018. **Note:** quartz-sericite schist crosscut by quartz-carbonate and milky quartz vein



Analysis and preparation (0: none, 1: exist)	
Bulk chemical composition:1	XRD analysis:0
Polish section: 0	Sulfur isotope:0
Thin section: 1	EPMA analysis: 0
Fluid inclusion analysis:1	

**Sample species:** Carbonate vein (**Sample name:** EC180320-38, **Primary key:** Cf-38). **Location:** Chifumbazi, Area: Northern Tete, **Country:** Mozambique, **Longitude (S):** -14.40127, **Latitude (E):** 33.01325, **Type of sample:** vein **Piece:**1, **Year of collection:** 2018, **Data input:** 20\_March\_2018. **Note:** quartz - carbonate vein crosscut by clear quartz veinlet with sulfides.



Analysis and preparation (0: none, 1: exist)	
Bulk chemical composition:1	XRD analysis:0
Polish section: 1	Sulfur isotope:0
Thin section: 1	EPMA analysis: 1
Fluid inclusion analysis:0	Dating: 0

## **Appendix 2.**

# **Mugomo deposit**

1. Whole-rock geochemistry of the
2. Fluid inclusion microthermometry
3. Sulfur Isotope

**Table 3:** Whole rock chemical compositions of metavolcanic rock from the Mugomo deposit. Units are wt% for major oxides and ppm for other elements.

Area	Mugomo deposit																	
Sample ID	Mg 17-02	Mg 17-09	Mg 16-02	Mg21-05	Mg21-13	Mg17-01	Mg16-09	Mg 15-01	Mg 21-01	Mg 17-06	Mg 17-18	Mg 21-05	Mg 15-02	Mg 17-09	Mg 21-03	Mg 21-13	Mg 16-02	Mg 17-00a
SiO <sub>2</sub> (wt.%)	83.63	56.13	74.05	69.87	75.37	76.12	81.72	69.191	68.617	75.158	77.366	70.57	76.23	56.13	75.04	74.94	74.05	80.34
TiO <sub>2</sub>	0	1.26	0.12	0.251	0.099	0.172	0.157	0.185	0.346	0.165	0.102	0.273	0.15	1.26	0.14	0.11	0.12	0.07
Al <sub>2</sub> O <sub>3</sub>	0.65	12.69	11.62	16.3	13.85	11.12	9.29	16.139	11.974	12.699	11.985	15.123	12.94	12.69	10.3	13.12	11.62	9.23
Fe <sub>2</sub> O <sub>3</sub> (T)	6.85	11.59	3.23	1.75	1.36	3.68	1.81	3.664	5.637	1.357	1.241	3.108	1.76	11.59	4.02	1.84	3.23	2.8
MnO	0.01	0.14	0.03	0.033	0.02	0.027	0.024	0.021	0.085	0.033	0.016	0.041	0.01	0.14	0.07	0.02	0.03	0.02
MgO	0.48	7.61	0.78	0.58	0.11	0.53	0.47	0.523	1.867	0.361	0.169	0.963	0.81	7.61	3.12	0.77	0.78	0.72
CaO	0.62	3.27	3.23	2.13	1.13	0.98	0.51	1.845	6.441	2.086	1.371	2.03	0.96	3.27	1.65	1.4	3.23	0.44
Na <sub>2</sub> O	0.1	0.6	5.53	7.48	7.03	5.16	4.52	5.936	1.173	6.588	5.297	6.59	5.66	0.6	1.67	7.39	5.53	4.93
K <sub>2</sub> O	0	5.34	0.37	0.27	0.17	0.55	0.2	1.129	1.615	0.112	0.42	0.246	0.88	5.34	3.23	0.23	0.37	0.33
P <sub>2</sub> O <sub>5</sub>	0.01	0.36	0.03	0.06	< 0.01	0.02	0.03	0.023	0.075	0.024	0.008	0.048	0.01	0.36	0.02	0.01	0.03	0
TOTAL	92.35	98.99	98.99	98.724	99.139	98.359	98.731	98.656	97.83	98.583	97.975	98.992	99.41	98.99	99.26	99.83	98.99	98.88
Ba	10.37	281.8	103.4	143	88	139	59	275	301	-18	153	113	198.5	297.8	633.2	133.9	131.9	185.5
Cu	280.7	38.52	4.08	27	31	17	5						0	35.4	0	2.8	0	154.6
Nb	0.04	2.43	2.77	2	3.6	1.2	1.5	4	11	2	4	4	1.4	8	2.2	3.7	10.5	5.3
Ni	41.23	32.51	4.54	205	68	91	39	12	110	11	8	15	0	44.1	0.3	0	0	4.5
Pb	87.47	2.03	2.05	< 5	< 5	< 5	< 5						2.8	2.4	6	2.5	2.3	1.1
Rb	0.62	96.6	6.54	2	2	15	5	33	32	5	8	5	18.9	122.6	53.6	4	7.7	4
Sr	39.97	147.3	184.5	163	118	120	59	214	225	87	166	140	167.8	185.5	100.5	174.1	218.8	49.3
Y	7.81	66.81	73.08	24.5	77.6	20.2	11.5	49	288	34	52	26	25.9	91.2	26.4	95.1	88.5	23.6
Zn	3002	121.5	6.37	14	6	30	18						8.1	139.5	90.3	6.8	7.3	10.5
Zr	106.8	179.8	119.7	117	222	88	74	154	88	115	236	126	144.7	106.8	109.2	358.4	179.8	215
Th	n/a	n/a	n/a	1.03	4.57	0.78	0.69											

**Table 4:** Whole rock chemical compositions of mafic metavolcanic rocks from the Mualadzi group. Units are wt% for major oxides ppm for other elements. Data from GTK consortium, 2006.

Sample	Area	Rock type	SiO <sub>2</sub>	TiO <sub>2</sub>	Al <sub>2</sub> O <sub>3</sub>	Fe <sub>2</sub> O <sub>3</sub> (T)	MnO	MgO	CaO	Na <sub>2</sub> O	K <sub>2</sub> O	P <sub>2</sub> O <sub>5</sub>	TOTAL	Rb	Y	Nb	Zr	
			%	%	%	%	%	%	%	%	%	%	%		ppm	ppm	ppm	
MD-39	Mualadzi group	Metabasalt	44.10	0.51	12.90	9.89	0.30	6.39	21.98	b.d	0.08	0.08	96.23		b.d	b.d	16	
MD-40		Metabasalt	44.10	0.01	1.18	7.50	0.23	38.20	0.23	b.d	0.00	b.d	91.45		b.d	b.d	b.d	
MD-41		Metavolcanic rock	48.00	0.39	12.70	12.48	0.24	7.92	14.59	1.62	0.38	0.08	98.40	b.d		8	b.d	b.d
MD-42		Mafic metatuff	49.20	1.85	14.50	14.79	0.23	6.28	8.84	3.36	0.26	0.17	99.48	b.d		33	b.d	114
MD-43		Metavolcanic rock	49.80	1.24	14.90	12.37	0.25	6.22	8.53	3.79	0.72	0.21	98.03	32		19	b.d	30
MD-44		Metavolcanic rock	50.20	0.45	6.86	12.20	0.25	11.80	8.84	3.36	0.06	0.04	94.06	b.d		17	b.d	18
MD-45		Metavolcanic rock	50.90	1.22	14.00	12.88	0.21	6.45	8.53	3.79	0.27	0.06	98.31	b.d		30	b.d	61
MD-46		Metavolcanic rock	51.00	0.37	9.24	10.80	0.25	10.90	14.81	0.17	0.10	0.12	97.76	b.d		20	b.d	10
MD-47		Tectonic breccia	63.00	0.77	22.00	1.06	0.02	0.65	0.97	7.97	3.08	0.02	99.54	53		8	b.d	103
MD-48		Felsic metavolcanic r	77.50	0.14	12.00	2.32	0.02	0.23	0.96	4.92	1.59	b.d	99.68	18		18	b.d	109
MD-49		Felsic metavolcanic r	80.10	0.10	10.30	1.16	0.02	0.05	1.01	1.81	4.94	b.d	99.49	91		32	b.d	327



**Table 5:** Whole rock trace and rare-earth element compositions for some selected samples of metavolcanic rock from the Mugomo deposit.

Sample ID	Mg 21-09	Mg 17-02	Mg 17-09	Mg 16-02	Mg21-05	Mg21-13	Mg17-01	Mg16-09
La (ppm)	15.5	1.79	8.28	12.35	7.45	24	5.29	1.98
Ce	33.04	4.41	19.32	31.71	18.3	55.6	13.9	5.24
Pr	4.47	0.62	2.72	4.87	2.54	7.82	2.03	0.79
Nd	19.39	2.99	13.22	24.01	12.2	35.8	9.93	3.88
Sm	4.22	0.93	4.65	7.37	3.11	9.59	2.92	1.34
Eu	2.38	0.39	1.17	1.89	0.772	1.68	0.783	0.238
Gd	4.04	1.24	7.71	9.97	3.37	10.8	3	1.27
Tb	0.55	0.22	1.54	1.81	0.61	1.95	0.55	0.26
Dy	3.24	1.56	11.58	12.59	4.02	12.9	3.59	1.83
Ho	0.68	0.34	2.67	2.76	0.9	2.68	0.73	0.4
Er	2.01	0.98	8.5	8.18	2.64	8.09	2.13	1.33
Tm	0.29	0.13	1.24	1.18	0.408	1.16	0.346	0.22
Yb	2	0.88	8.44	7.93	2.98	7.84	2.46	1.55
Lu	0.31	0.14	1.24	1.23	0.468	1.2	0.401	0.247
Y	17.18	7.81	66.81	73.08	24.5	77.6	20.2	11.5
Sc	4.13	1.36	27.36	20.29	12	9	12	7
Au	<0.000	1.75	0.02	0.28	< 2	< 2	0.003	< 2
Be	0.27	0.03	0.46	0.53	< 1	1	< 1	< 1
Co	2.42	173.8	21.48	31.64	5	2	3	2
Ni	3.98	41.23	32.51	4.54	205	68	91	39
Cu	29.4	280.7	38.52	4.08	27	31	17	5
Zn	7.06	3002	121.5	6.37	14	6	30	18
Rb	4.66	0.62	96.6	6.54	2	2	15	5
Sr	162.1	39.97	147.3	184.5	163	118	120	59
Zr	32.18	106.8	179.8	119.7	117	222	88	74
Nb	1.44	0.04	2.43	2.77	2	3.6	1.2	1.5
Ag	0.03	16.45	<0.000	0.3	< 0.3	0.4	< 0.3	< 0.3
Cd	0.07	12.47	0.06	0.18	< 0.5	< 0.5	< 0.5	< 0.5
Sn	1.03	0.32	1.63	1.51	1	1	1	1
Sb	0.58	0.4	0.74	0.53	< 0.2	< 0.2	< 0.2	0.2
Cs	0.71	0.13	11.47	0.2	< 0.1	0.1	1.6	0.3
Ba	53.87	10.37	281.8	103.4	143	88	139	59
Pb	5.31	87.47	2.03	2.05	< 5	< 5	< 5	< 5

**Table 6:** Transition metal and metalloids compositions for some selected samples of metavolcanic rock from the Mugomo deposit.

Area	Sample ID	Rock	Mn (ppm)	Co	Ni	Cu	Zn	Au	Ag	Cd	Te	Pb
Mugomo deposit	Mg 15-03	Rhyolite dacite	131.7	1.6	3.82	4.88	21.14	0.04	0.04	0.08	0.01	1.57
	Mg 15-04	Epidote quartz vein	137	255.9	5.87	21.57	5.31	0.01	0.1	0.1	<0.000	2.3
	Mg 16-04	Epidote quartz vein	213.4	31.64	4.54	4.08	6.37	0.28	0.3	0.18	0.01	2.05
	Mg 16-06	Epidote quartz vein	536.2	0.89	1.91	2.65	<0.000	0.01	0.01	0.15	0.19	5.96
	Mg 16-09	Epidote quartz vein	150.7	0.42	1.6	2.4	3.6	0.01	0.2	0.12	<0.000	2.43
	Mg 17-00b	Rhyolite dacite	654.5	13.7	23.17	90.27	19.93	0.01	0	0.07	0.15	5.12
	Mg 17-07	Rhyolite dacite	145.6	3.25	10.54	154.3	11.7	0.02	0.39	0.19	0.08	2.37
	Mg 17-09 a	Epidote quartz vein	8.04	1.33	3.02	1023	<0.000	0	0.5	0.01	0.1	1.26
	Mg 17-13	Rhyolite dacite	46.74	173.8	41.23	280.7	3002	1.75	16.45	12.47	18.99	87.47
	Mg 17-16	Rhyolite dacite	169	2.51	3.21	17.32	15.16	0.05	0.36	0.24	0.06	11.8
	Mg 17-21	Rhyolite dacite	768	24.1	17.56	104.2	29.85	0.02	0.26	0.09	0.26	10.01
	Mg 20-13	Rhyolite dacite	768.9	21.48	32.51	38.52	121.5	0.02	0	0.06	0.29	2.03
	Mg 21-03	Rhyolite dacite	1295	4.9	3.34	37.92	20.35	0	0.21	0.1	0.07	6.06
	Mg 21-07	Rhyolite dacite	362.5	21.6	9.46	313.5	106.4	0.04	2.41	0.46	7.04	16.14
	Mg 21-08	Epidote quartz vein	1032	8.49	15.07	123.6	18.2	0.03	0	0.08	0.05	9.24
	Mg 21-09	Rhyolite dacite	744.4	38.22	11.86	458	69.54	0.02	0.25	0.26	0.77	0
	Mg 17-02	Rhyolite dacite	525.7	9.79	19.63	140.6	50.06	0.02	0.16	0.13	0.27	4.04
	Mg 17-09 b	Biotite-schist	217.8	2.19	5.51	8.93	16.58	<0.000	0.72	0.12	0.07	4.93
	Mg 16-01	Rhyolite dacite	769.1	6.94	8.05	3.15	42.7	0	0.12	0.16	0.05	8.83
	Mg 17-00 a	Epidote quartz vein	227.1	2.42	3.98	29.4	7.06	<0.000	0.03	0.07	0.09	5.31

**Table7:** Microthermometry data of Type II and III inclusions of the Mugomo deposit.

Sample ID	Fluid type	Raw data		Corrected data		
		Tm	Th	Tm	Th	Salinity
Mg 21-06	Type II	-2.8	323.7	-2	312	4
		-3.3	352.9	-2	339	4
		-0.6	329.7	0	317	1
		-1.4	323.2	-1	311	2
		-2.5	306.7	-2	296	3
		-3	314.5	-2	303	4
		-1.6	378.9	-1	364	2
		-3.5	430.3	-3	413	4
		-2.1	321.3	-2	310	3
		-6.4	438.5	-5	420	8
		-3.3	352.9	-2	339	4
Mg 16-04		-2.8	323.7	-2	312	4
		-1.8	324.3	-1	312	2
		-3.2	205.6	-2	199	4
		-0.9	314.4	-1	303	1
		-12	442	-11	424	15
		-1.7	412.5	-1	396	2
		-6.3	248.6	-5	240	8
Mg 17-18		-2.4	219.9	-2	213	3
		-5.8	338.5	-5	326	7
		-12	441.8	-11	423	15
		-3.8	280	-3	270	5
	-12.1	254	-11	246	15	
Mg 21-06	Type III	-4.1	239	-3	231	5
		-0.7	209	0	202	1
		-22.4	458.2	-25	439	26
		-24.5	448.8	-29	430	28

**Table 8:** Measured  $\delta^{34}\text{S}_{\text{CDT}}$  (‰) from the sulfide minerals in the Mugomo deposit

Sample No.	Mineral	$\delta^{34}\text{S}\text{‰}$
MG-17-09	Pyrite	2.5
MG-17-08	Pyrite	3.8
MG-16-09	Pyrite	3.5
MG-17-21	Pyrite	3.5
Mg 17-07	Pyrite	3.1
Mg16-02	Pyrite	3.3
Mg17-02	Pyrite	3.0
Mg17-23	Pyrite	3.6

## **Appendix 3**

### **Chifumbazi deposit**

1. Whole-rock geochemistry
2. Fluid inclusion microthermometry
3. Sulfur isotope

**Table 9:** Whole rock trace element compositions of quartz-mica-schist from the Chifumbazi deposit.

Area	Chifumbazi Deposit															
Rock type	Meta-granodiorite															
Sample	CF-15	CF-42	CF-05	CF-18	CF-1	CF-05	CF-06	CF-08	CF-10	CF-13	CF-14	CF-16	CF-18	CF-31	CF-37	CF-40
SiO <sub>2</sub> (wt.%)	68.1	58.3	65.0	66.0	66.0	64.7	64.0	64.5	64.0	61.4	65.2	57.1	65.4	65.0	72.4	57.9
TiO <sub>2</sub>	1.18	1.14	1.21	1.34	0.94	1.04	0.96	1.18	1.03	0.87	1.26	1.40	1.24	0.97	0.88	1.13
Al <sub>2</sub> O <sub>3</sub>	16.6	16.4	15.7	17.5	14.2	16.2	16.9	19.3	13.1	15.2	17.9	20.0	18.4	16.1	13.0	15.7
Fe <sub>2</sub> O <sub>3</sub> (T)	3.09	6.93	6.53	3.70	7.03	5.73	6.89	2.85	8.12	7.12	3.40	4.95	3.56	5.17	4.44	7.51
MnO	0.07	0.10	0.04	0.05	0.04	0.03	0.06	0.02	0.08	0.08	0.05	0.08	0.02	0.05	0.02	0.09
MgO	0.37	1.36	0.40	0.50	1.92	0.98	1.49	1.09	2.43	1.68	1.05	1.52	1.11	1.22	1.20	2.20
CaO	0.68	3.55	0.15	0.55	0.89	0.18	0.61	0.53	2.22	3.52	0.83	3.08	0.59	1.63	0.56	3.73
Na <sub>2</sub> O	4.87	5.42	2.93	2.02	3.72	2.68	1.64	2.92	3.23	1.61	4.12	3.04	1.44	2.14	2.10	4.61
K <sub>2</sub> O	2.83	2.89	3.89	4.79	3.02	4.21	4.85	5.07	3.48	4.59	4.00	5.46	5.85	4.80	3.30	3.47
P <sub>2</sub> O <sub>5</sub>	0.36	0.34	0.12	0.37	0.26	0.12	0.39	0.35	0.34	0.29	0.54	0.39	0.42	0.33	0.36	0.34
LOI	1.26	3.50	3.96	2.00	1.84	3.34	1.99	1.87	1.76	3.30	1.38	2.69	1.73	1.78	1.40	3.11
TOTAL	99.4	99.9	99.9	98.7	99.8	99.2	99.7	99.7	99.8	99.7	99.8	99.6	99.7	99.2	99.6	99.8
Ba (ppm)	1281	791	1704	1770	717	1654	1756	1943	847	1451	1486	2102	1956	1673	1207	794
Cu	24.0	11.0	60.0	14.0	24.4	38.0	222	20.2	10.5	93.3	2.7	50.9	0.0	179.0	130.9	0.0
Nb	11.8	14.2	11.4	16.9	13.3	24.8	7.90	19.5	9.9	10.2	17.7	18.3	23.1	21.0	12.9	13.9
Ni	3.00	75.0	6.00	3.00	12.1	2.7	9.70	5.20	10.8	10.0	4.30	8.60	9.50	11.8	1.30	11.4
Pb	8.00	98.0	33.0	< 5	11.4	4.1	4.80	3.50	8.10	7.20	8.60	7.70	4.20	4.60	3.80	7.00
Rb	54.0	100	69.0	88.0	127.3	71.0	100	86.6	132.9	113.4	76.1	106.6	107.7	89.6	61.5	125.4
Sr	184	310	172	82.0	230.8	169.4	157	97.3	269	151	201	245	95.6	120	104	325
Y	51.5	55.0	53.4	56.0	53.8	47.7	66.8	78.8	66.3	55.3	78.0	51.0	62.3	59.6	56.7	60.5
Zn	16.0	183	51.0	16.0	76.5	8.0	23.2	11.8	68.7	53.4	17.3	22.1	13.0	17.3	17.2	73.4
Zr	412	371	379	437	472	331	321	408	360	309	464	465	449	375	325	383
Th	16.6	13.6	16.5	9.8	n/a	n/a	n/a	n/a	n/a	n/a	0.1	n/a	n/a	n/a	n/a	10.2

**Table 10:** Whole rock trace element compositions meta-diorite and meta-granodiorite from Zambia (Southern Irumide Belt)

Area	Southern Irumide Belt (Zambia)						
Rock type	Meta-diorite			Meta-granodiorite			
Sample	36	58	45A	63	48A	38	42
SiO <sub>2</sub> (wt.%)	55.17	59.64	61.44	67.24	67.96	75	76.48
TiO <sub>2</sub>	2.66	1.03	1.01	1.2	0.93	0.4	0.66
Al <sub>2</sub> O <sub>3</sub>	13.55	16.2	17.98	14.08	12.54	13.53	10.34
Fe <sub>2</sub> O <sub>3</sub> (T)	12.89	10.19	9.1	4.91	6.66	2.95	4.82
MnO	0.15	0.18	0.05	0.04	0.15	0.03	0.07
MgO	3.54	4.47	3.07	2.43	1.3	0.45	1.42
CaO	8.35	2.67	0.69	4.39	9.19	0.82	3.42
Na <sub>2</sub> O	1.65	2.93	1.08	2.96	0.75	4.26	2.01
K <sub>2</sub> O	1.5	2.65	4.49	1.9	0.45	2.15	0.93
P <sub>2</sub> O <sub>5</sub>	0.3	0.18	0.16	0.25	0.14	0.1	0.11
LOI	0	0	0.45	0.21	0	0	0
TOTAL	99.76	100.14	99.52	99.61	100.07	99.69	100.26
Ba (ppm)	458.3	808.3	811.1	407.8	106.8	767.9	206.4
Cu	136.5	56	105.3	0.5	1.3	184.4	2.8
Nb	29.9	15.8	17.5	20.2	19.6	61.5	11.8
Ni	49.4	69.2	51.4	16.4	23.2	<1.4	24.4
Pb	6.4	17.3	13.4	1.4	25	2.7	6
Rb	41.2	102.3	190.8	106	27	67.3	59.4
Sr	265.8	99	72.1	268.2	241.8	216.5	212.3
Y	3.1	33.6	33.8	52.6	41.1	91.2	25
Zn	107.2	95	79	20.5	35.4	42.3	36.1
Zr	251	203.5	196.6	242.9	206.2	464.6	188.2
Th	9.1	17.2	18.1	27.5	19	33.1	14.4

**Table 11:** Whole rock trace element compositions of veins from the Chifumbazi deposit.

Vein type	Chlorite	Quartz									Quartz-carbonate					
Sample ID	Cf - 08	Cf - 06	Cf - 09	Cf - 14	Cf - 17	Cf - 18	Cf - 24	Cf - 30	Cf - 43	Cf - 12	Cf - 19	Cf - 32	Cf - 38	Cf - 26	Cf - 27	
Li (ppm)	19.4	2.20	5.41	1.71	2.67	37.5	22.0	35.2	2.176 p	46.7	8.737E-0	2.15	7.99	1.77	30.1	
Be	5.1	0.11	0.30	0.06	0.24	4.04	0.51	0.20	0.12	0.48	0.06	0.09	0.07	0.17	4.07	
Sc	22.3	11.6	19.0	8.92	8.50	37.2	20.8	13.2	7.12	18.33	6.93	13.15	8.13	7.56	36.1	
Mn	466	101	327	1897	183	705	6442	1330	215	1781	57.9	12080	2107	101	4123	
Co	3.99	2.20	560	1.83	24.9	5.89	17.7	18.1	25.6	24.4	2.02	8.75	8.73	16.8	18.5	
Ni	2.76	1.88	311	2.89	4.66	3.88	5.39	10.8	12.4	8.70	4.99	5.95	4.06	7.65	8.61	
Cu	69.3	18.0	758	8064	172	31.6	8.9	17.2	4486	209	29.6	19.4	12.9	1183.0	121	
Zn	48.7	10.9	382	42.3	29.6	70.8	104.7	109.7	27.4	224.2	23.0	61.7	51.0	36.6	69.8	
Rb	132	3.23	7.28	0.43	8.66	134.2	10.5	4.83	3.54	6.30	1.69	1.10	1.05	2.66	121	
Sr	145	8.2	226.6	115.5	14.6	77.9	579	9.4	13.4	104.3	6.76	556.4	19.2	48.5	317	
Y	18.0	0.35	57.4	5.47	4.6	14.6	23.1	2.52	1.86	6.62	0.52	22.14	5.22	1.79	17.9	
Zr	62.4	0.22	54.0	0.52	21.0	53.8	18.5	5.39	0.38	8.71	0.91	0.85	0.29	6.77	56.4	
Nb	21.7	0.18	6.08	0.45	2.46	19.3	1.05	1.02	0.42	1.75	0.26	0.49	0.11	0.55	19.1	
Au	0.08	0.04	4.70	0.06	0.12	0.10	0.06	0.14	1.81	0.20	0.16	0.23	0.05	0.43	0.10	
Ag	0.30	0.03	30.34	1.04	0.15	0.26	0.10	0.09	0.19	0.21	0.03	0.06	0.03	0.25	0.32	
Cd	0.16	0.07	1.80	0.58	0.62	0.23	0.85	0.23	0.37	0.14	0.07	1.45	0.24	0.14	0.87	
Sn	9.17	0.34	3.36	0.86	0.66	10.4	0.93	0.37	0.52	0.51	0.70	0.33	0.53	0.51	6.57	
Sb	0.79	0.30	1.23	0.78	0.41	0.31	0.26	0.46	0.99	0.11	0.38	0.17	0.32	0.44	0.83	
Te	0.08	0.07	61.87	0.43	1.17	0.07	0.49	0.40	85.5	0.37	0.04	1.00	0.11	1.28	0.29	
Cs	4.73	0.23	1.23	0.26	0.53	3.10	0.75	0.91	0.37	0.33	0.17	0.13	0.16	0.21	4.13	
Ba	3067	46.2	119.1	10.2	162	2282	203	32.0	52.6	135	34.6	40.9	22.8	59.4	2337	
La	40.6	1.12	9.10	12.7	9.20	22.8	7.62	1.86	5.36	25.2	0.95	4.52	3.10	5.56	54.4	
Ce	106	2.12	23.8	26.4	20.8	57.5	15.9	3.2	11.3	59.7	2.10	10.3	4.95	12.70	123	
Pr	14.7	0.26	3.41	3.35	2.60	6.97	2.10	0.55	1.41	7.4	0.28	1.39	0.89	1.62	15.5	
Nd	59.4	0.95	16.2	14.3	10.5	28.5	8.89	2.33	5.79	27.5	1.16	6.33	3.85	6.72	63.7	
Sm	12.7	0.23	5.22	3.28	2.38	6.39	2.63	0.63	1.36	5.06	0.30	2.34	1.08	1.51	14.1	
Eu	2.2	0.05	2.09	0.70	0.45	1.01	0.97	0.22	0.29	0.89	0.07	1.47	0.34	0.30	2.89	
Gd	10.1	0.19	7.17	2.98	2.15	5.58	3.71	0.74	1.26	4.16	0.32	3.93	1.35	1.30	11.6	
Tb	1.12	0.02	1.37	0.33	0.25	0.65	0.66	0.10	0.14	0.41	0.03	0.71	0.19	0.14	1.20	
Dy	4.65	0.09	9.78	1.31	1.09	3.13	4.18	0.53	0.54	1.65	0.13	4.33	1.06	0.49	4.76	
Ho	0.70	0.02	2.17	0.21	0.18	0.55	0.94	0.11	0.07	0.28	0.02	0.87	0.21	0.09	0.73	
Er	1.85	0.04	6.80	0.61	0.49	1.48	3.33	0.33	0.18	0.78	0.05	2.60	0.63	0.20	1.85	
Tm	0.24	0.01	1.01	0.09	0.07	0.19	0.60	0.06	0.03	0.11	0.01	0.42	0.10	0.03	0.25	
Yb	1.42	0.06	6.62	0.68	0.43	1.09	5.49	0.41	0.22	0.75	0.05	3.56	0.73	0.23	1.73	
Lu	0.24	0.01	0.97	0.14	0.07	0.17	1.07	0.08	0.04	0.14	0.01	0.68	0.13	0.04	0.32	
Pb	4.83	2.04	65.9	12.55	1.25	3.32	9.16	2.91	3.78	1.44	1.25	6.16	2.31	2.87	7.06	
Th	15.2	0.04	1.15	0.07	1.98	6.33	0.40	0.19	0.07	1.63	0.09	0.08	0.04	0.94	11.8	
U	2.16	0.11	28.0	0.03	0.62	0.89	0.29	0.10	0.07	1.16	0.11	8.63	0.15	0.40	2.88	



**Table 12:** Transition metal and metalloids compositions for some selected samples the Chifumbazi deposit.

Area	Sample ID	Rock	Mn (ppm)	Co	Ni	Cu	Zn	Au	Ag	Cd	Te	Pb
Chifumbazi deposit	Cf- 02	Meta-granodiorite	409.8	5.18	2.93	34.8	39.54	0.04	0.17	0.14	0.19	6.53
	Cf - 06	Quartz vein	101.2	2.2	1.88	17.98	10.89	0.04	0.03	0.07	0.07	2.04
	Cf - 08	Chlorite vein	465.9	3.99	2.76	69.26	48.73	0.08	0.3	0.16	0.08	4.83
	Cf - 09	Quartz vein	326.5	560.1	310.8	758.1	381.6	4.7	30.34	1.8	61.87	65.88
	Cf - 12	Quartz-carbonate veir	1781	24.41	8.7	209	224.2	0.2	0.21	0.14	0.37	1.44
	Cf -14	Quartz vein	1897	1.83	2.89	8064	42.29	0.06	1.04	0.58	0.43	12.55
	Cf - 17	Quartz vein	183.3	24.9	4.66	172.3	29.57	0.12	0.15	0.62	1.17	1.25
	Cf - 18	Quartz vein	705	5.89	3.88	31.55	70.84	0.1	0.26	0.23	0.07	3.32
	Cf - 19	Quartz-carbonate veir	57.87	2.02	4.99	29.61	22.97	0.16	0.03	0.07	0.04	1.25
	Cf - 22	Meta-granodiorite	543.3	156.7	104.4	1196	26.23	0.08	0.36	0.18	25.93	6.16
	Cf - 23	Quartz vein	8893	3.56	6.04	7.18	30.52	0.05	0.25	1.16	0.4	12.95
	Cf - 24	Quartz vein	6442	17.74	5.39	8.87	104.7	0.06	0.1	0.85	0.49	9.16
	Cf - 25	Meta-granodiorite	1345	43.48	8.45	314.8	85.85	0.1	0.58	0.38	9.62	11.71
	Cf - 26	Quartz vein	100.9	16.75	7.65	1183	36.64	0.43	0.25	0.14	1.28	2.87
	Cf - 27	Chlorite vein	4123	18.52	8.61	121.4	69.84	0.1	0.32	0.87	0.29	7.06
	Cf - 28	Quartz vein	5193	7.38	4.14	5.62	76.65	0.06	0.12	0.94	0.3	6.19
	Cf - 30	Quartz vein	1330	18.05	10.77	17.19	109.7	0.14	0.09	0.23	0.4	2.91
	Cf - 31	Meta-granodiorite	1660	43.71	8.76	1367	95.19	1.41	0.81	0.66	0.54	6.27
	Cf - 32	Quartz-carbonate veir	12080	8.75	5.95	19.38	61.68	0.23	0.06	1.45	1	6.16
	Cf - 36	Meta-granodiorite	1316	18.82	9.65	30.96	131.1	0.1	0.24	0.4	0.37	9.13
Cf - 37	Meta-granodiorite	19120	26.74	8.19	150	62.09	0.48	0.11	1.5	0.82	9.1	
Cf - 38	Quartz-carbonate veir	2107	8.73	4.06	12.93	50.99	0.05	0.03	0.24	0.11	2.31	
Cf -40	Meta-granodiorite	2607	98.1	13.43	1515	115	0.1	0.76	0.93	1.28	7.05	
Cf - 43	Quartz vein	214.5	25.63	12.4	4486	27.39	1.808	0.1879	0.371	85.45	3.782	

**Table 13:** Microthermometry data of Type II inclusions of the Chifumbazi deposit.

Sample no.	Stage	Host mineral	No	Inclusion size ( $\mu\text{m}$ )	Type	T <sub>m</sub> ( $^{\circ}\text{C}$ )	T <sub>h</sub> ( $^{\circ}\text{C}$ )	Salinity (wt % NaCl equiv.)
CF-40	II	Clear quartz	1	12	L+V	-7.0	216	10.5
		Clear quartz	2	10		-5.1	277	8.0
		Clear quartz	3	8		-1.9	258	3.3
		Clear quartz	4	9		-1.7	241	2.9
		Clear quartz	5	12		-7.9	288	11.5
CF-28	II	Clear quartz	1	18	L+V	-1.2	226	2.1
		Clear quartz	2	11		-0.6	267	1.1
		Clear quartz	3	20		-0.4	219	0.7
		Clear quartz	4	7		-1.4	267	2.4
		Clear quartz	5	5		-0.6	304	1.1
		Clear quartz	6	9		-11.3	283	15.3
CF-08	II	Ferruginous quartz	1	9	L+V	-11.2	298	15.2
		Ferruginous quartz	2	11		-3.8	369	6.1
		Ferruginous quartz	3	14		-0.4	219	0.7
		Ferruginous quartz	4	6		-1.2	226	2.1
		Ferruginous quartz	5	5		-3.3	300	5.4

**Table 14:** Measured  $\delta^{34}\text{S}_{\text{CDT}}$  (‰) from the sulfide minerals in the Chifumbazi deposit.

Sample No.	Stage	Mineral	$\delta^{34}\text{S}_{\text{‰}}$
CF-09	II	Pyrite	2.4
CF-13	I	Pyrite	1.1
CF-14	II	Chalcopyrite	1.4
CF-22	I	Pyrite	0.9
CF-26	I	Pyrite	1.7
CF-26-a	III	Pyrite	1.5
CF-31	I	Pyrite	1.2
CF-32	I	Pyrite	1.6
CF-35	II	Pyrite	1.1
CF-37	II	Pyrite	1.0
CF-40	II	Pyrite	1.8
CF-43	III	Chalcopyrite	1.1
CF-43-a	I	Pyrite	1.2